ELSEVIER

Nuclear Instruments and Methods in Physics Research A 479 (2002) 349–406

NUCLEAR INSTRUMENTS & METHODS IN PHYSICS RESEARCH Section A

www.elsevier.com/locate/nima

A large acceptance, high-resolution detector for rare K^+-decay experiments ☆

R. Appel[a,b], G.S. Atoyan[c], B. Bassalleck[d], E. Battiste[b], D.R. Bergman[a,1], K. Bösiger[e], D.N. Brown[b,2], V. Castillo[f], N. Cheung[b], S. Dhawan[a], H. Do[a], J. Egger[g], S.W. Eilerts[d,3], C. Felder[b,f], H. Fischer[d,4], H.M. Gach[b,5], R. Giles[b], S.N. Gninenko[c], W.D. Herold[g], J.E. Hotmer[b,6], V.V. Issakov[c], O.V. Karavichev[c], H. Kaspar[g,a], D.E. Kraus[b], D.M. Lazarus[f], V.A. Lebedev[c], L. Leipuner[f], P. Lichard[b], J. Lowe[d,7], J. Lozano[a,8], T. Lu[b], H. Ma[f], B. Magurno[f,*], W. Majid[a,9], W. Menzel[h,10], C.S. Miller[b,11], M. Nickelson[b,12], I. Ober[b,13], P.H. Pile[f], S. Pislak[e,a,14], A.A. Poblaguev[c], P. Pomianowski[b,15], V.E. Postoev[c], A.L. Proskurjakov[c], P. Rehak[f], P. Robmann[e], B. Schmid[e], A. Sher[b], Aleksey Sher[e], E. Shunko[b,16], S. Steiner[e], T.L. Stever[b,17], R.W. Stotzer[d,18], V.V. Suhov[c], J.A. Thompson[b], P. Truöl[e,a,*], C. Valine[b,19], H. Weyer[g,h], D.M. Wolfe[d], M.E. Zeller[a]

☆ This work was supported in part by the US Department of Energy, the National Science Foundations of the USA, Russia and Switzerland, the Research Corporation and the REU-program of the NSF.

*Corresponding authors. Tel.: 00411-01-635-5777; fax: 00411-01-635-5704. Tel.: 1-631-344-3959; fax: 1-631-344-5954.
E-mail addresses: lazarus@bnl.gov (D.M. Lazarus), truoel@phyzik.unizh.ch (P. Truöl).
[1] Present address: Department of Physics, Rutgers University, Piscataway, NJ 08855 USA.
[2] Present address: Department of Physics, University of Louisville, Louisville, KY 40292, USA.
[3] Present address: The Prediction Company, Santa Fe, NM 87501, USA.
[4] Present address: Albert-Ludwigs-Universität, D-79104 Freiburg, Germany.
[5] Present address: Medical School, University of Pittsburgh, Pittsburgh, PA 15260, USA.
[6] Present address: AIL Systems Inc., Deer Park, NY 11729, USA.
[7] Also at: Physics Department, University of Birmingham, B15 2TT, UK.
[8] Present address: University of Connecticut, Storrs, CT 06269, USA.
[*] Deceased.
[9] Present address: LIGO, Caltech, Pasadena, CA 91125, USA.
[10] Present address: Universitätspital, CH-8091 Zürich, Switzerland.
[11] Present address: Old Dominion University, Norfolk, VA 23259, USA.
[12] Present address: Dep. of Applied Physics, University of Michigan, Ann Arbor, MI 48109, USA.
[13] Present address: Mt. Lebanon Sr High School, Mt. Lebanon, PA 15228, USA.
[14] Present address: Phonak AG, CH-8712 Stäfa, Switzerland.
[15] Present address: MIT Lincoln Lab., Lexington, MA 02421, USA.
[16] Present address: WINTEK Technology Center, Ann Arbor, MI 48109, USA.
[17] Present address: Zoll Medical Corp., Burlington, MA 01803, USA.
[18] Present address: ORION Int. Technologies, Albuquerque, NM 87106, USA.
[19] Present address: INTEL Corp., Phoenix, AZ 85226, USA.

0168-9002/02/$ - see front matter © 2002 Elsevier Science B.V. All rights reserved.
PII: S0168-9002(01)00906-8

FERMILAB

6. Particle identification . . . 378
6.1. Gas Cherenkov counters . . . 378
6.1.1. Introduction . . . 378
6.1.2. Operating history . . . 378
6.1.3. Optics design . . . 379
6.1.4. Optics tests and construction . . . 380
6.1.5. Mechanical design and construction . . . 382
6.1.6. Photomultipliers . . . 383
6.1.7. Performance . . . 384
6.1.8. Summary . . . 388
6.2. Muon identifier . . . 389
6.2.1. Mechanical construction . . . 390
6.2.2. Electronics . . . 391
6.2.3. Reconstruction and performance . . . 392
7. Trigger . . . 394
7.1. Trigger concept . . . 397
7.2. Hardware realization . . . 397
7.2.1. T0 trigger level . . . 398
7.2.2. T1 trigger . . . 398
7.2.3. T2 trigger . . . 399
7.2.4. T3 trigger . . . 400
8. Online data acquisition and filtering . . . 400
8.1. Data acquisition . . . 401
8.2. Online event filtering . . . 401
9. Typical results . . . 402
Acknowledgements . . . 403
References . . . 404
405

1. Introduction

Because of the incompleteness of the Standard Model of elementary particle physics, several extensions have been proposed which allow the possibility of flavor changing neutral currents and lepton-family violating interactions. Stimulated by these proposals, and a curiosity about the exactness of lepton-family number conservation, many experiments have been undertaken in the last two decades in search of decays such as $\mu^- \to e^- e^+ e^-$ [1], $\mu^- A \to e^- A$ [2], $\mu^+ \to e^+ \gamma$ [3], $K_L^0 \to \mu^\pm e^\mp$ [4], and $K^- \to \pi^+ \mu^+ e^-$ [5], to name those for which the lowest limits on the respective branching ratios have been established. This report is a description of an apparatus constructed at the Brookhaven Alternating Gradient Synchrotron for experiment E865 to perform an improved search for one of these decays: $K^+ \to \pi^- \mu^+ e^-$.

1.1. Physics motivation

$K^+ \to \pi^+ \mu^\pm e^-$: Measuring the branching ratio for the decay $K^+ \to \pi^- \mu^+ e^-$ ($K_{\pi\mu e}$) was the primary motivation for experiment E865. This lepton-family number violating decay could result from extensions to the Standard Model such as supersymmetry, leptoquarks, technicolor, and other horizontal gauge boson models.

One can cast a search for this decay mode in terms of extending the mass scale for the new interaction. Assuming a vector interaction, the branching ratio (B.R.) for $K_{\pi\mu e}$ can be compared with that of the Standard Model allowed decay $K^+ \to \pi^0 \mu^- \nu_\mu$ ($K_{\mu 3}$):

$$\frac{\text{B.R.}(K_{\pi\mu e})}{\text{B.R.}(K_{\mu 3})} \approx \frac{16}{\sin^2\theta_c}\left(\frac{g_X}{g}\right)^4\left(\frac{M_W}{M_X}\right)^4 \quad (1)$$

FERMILAB

where θ_c is the Cabbibo angle; g_X and g are the couplings for the new and weak interactions, respectively; M_W is the mass of the W boson; and M_X is the mass of the hypothesized vector boson mediating the new interaction. The expected level of sensitivity to the B.R.($K_{\pi\mu e}$) of 10^{-11} thus explores a mass scale for a new interaction of

$$\frac{g}{g_X} M_X \approx 84 \text{ TeV}/c^2. \quad (2)$$

$K^+ \to \pi^+ l^+ l^-$: The decays $K^+ \to \pi^+ e^+ e^-$ and $K^+ \to \pi^+ \mu^+ \mu^-$ proceed via a flavor changing neutral current and are suppressed by the Glashow–Iliopoulos–Maiani (GIM) mechanism. While the quark level component of the decay rate is through the $s \to d\gamma$ transition, the observed rate is dominated by long distance effects. The interest in these modes is thus in the information they provide for chiral QCD perturbation theory (ChPT) [6,7]. Prior to E865, about 500 events of the former mode [8,9] and 200 events of the latter [10] had been observed. E865, having recorded about 10,000 and 400 events, respectively, was able to determine that the ChPT calculations of $O(p^4)$ were inadequate, and showed that the rate and form factor for $\pi\mu\mu$ were in agreement with that expected from πee [11,12].

$K^- \to \pi^+ \pi^- e^- \nu_e$ (K_{e4}): Because the two pions are the only hadrons in the final state, K_{e4} is one of the cleanest sources of information on the low-energy $\pi\pi$ interaction [13,14]. Precise measurement of the S-wave $\pi\pi$ scattering length a_0^0 has thus been an experimental goal for more than three decades, with the most recent measurement having recorded 30,000 events [15]. E865 recorded 10 times that amount, allowing a significant reduction in the uncertainty on a_0^0 and on the other parameters describing this decay.

$K^+ \to l^+ \nu_l e^+ e^-$ (radiative K_{l2}): Observation of the modes $K^+ \to \mu^+ \nu_\mu e^+ e^-$ and $K^+ \to e^+ \nu_e e^+ e^-$ allows one to study radiative K_{l2} with virtual photons. Such studies allow measurements of the magnitudes, signs and structure of electromagnetic form factors of the K^+ that are inaccessible with on-shell photons. Prior to E865 14 events from μvee and four from evee had been detected [16]. E865 observed about 1500 events of the former and 400 events of the latter modes. Because of the different masses of the primary leptons, having a sizable sample from both modes allows broad exploration of the structure of these decays.

1.2. Experimental overview

The experimental goal of E865 was to search for the $K_{\pi\mu e}$ decay with a single event sensitivity for a branching ratio of a few times 10^{-12}. This

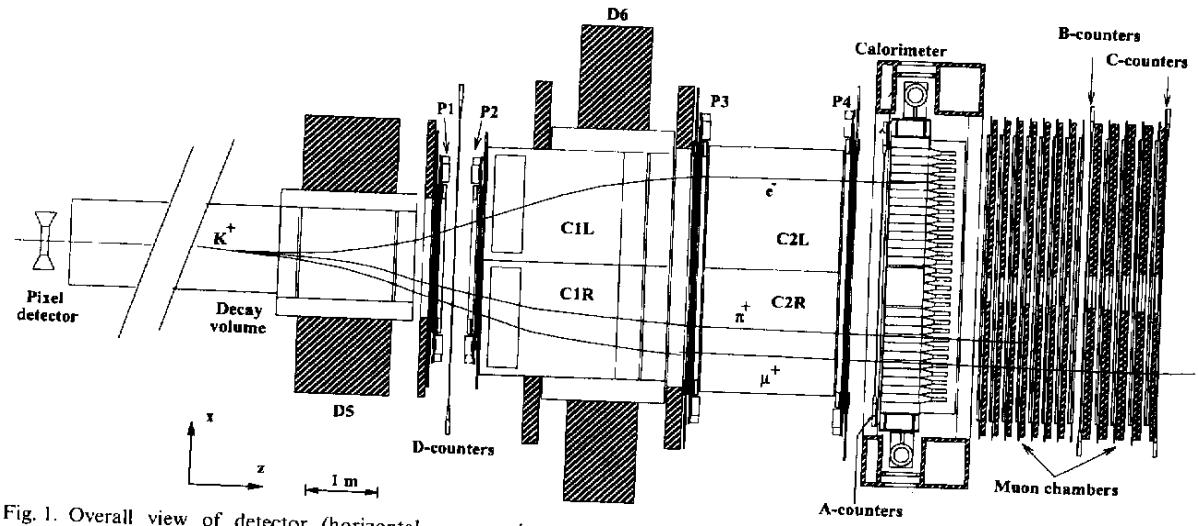

Fig. 1. Overall view of detector (horizontal cross-section at beam height). C1/C2: gas Cherenkov counters; P1/P2/P3/P4: proportional chambers; D5/D6: dipole magnets; A/B/C/D-counters: scintillator trigger hodoscopes.

required an intense K^+ beam and an apparatus with a large acceptance for three-body decays. The mode sought for is on the order of 10^{-9} of other K^+ decay modes such as $K^+ \to \pi^+\pi^+\pi^- \times$ (K_τ, B.R. = 0.056) and $K^+ \to \pi^+\pi^0$; $\pi^0 \to e^+e^-\gamma$ (K_{Dal}, B.R. $= 2.3 \times 10^{-3}$). Thus correct identification of particle species (PID) and precision in the tracking of the trajectories of the decay products were important considerations.

The apparatus shown in Fig. 1 resided in an unseparated beam directly downstream from a 5 m long vacuum decay volume. The 6 GeV/c beam contained about 10^8 K^+ and 2×10^9 protons and π^+ per spill, with approximately 10% of the beam kaons decaying in the decay volume. A dipole magnet at the exit of the decay region approximately separated K^+ decay products by charge (negative to beam left, positive to beam right) and reduced the charged particle background originating upstream of the detector. Proportional chamber packages (P1–P4), each containing four planes of chambers, were arrayed on either side of a second dipole magnet to form a momentum analyzing spectrometer system.

The first elements of the PID system were atmospheric pressure Cherenkov counters upstream and downstream of the spectrometer magnet. The left sides of each, C1L and C2L, were filled with hydrogen gas to detect e^-. To reject e^+ the right sides, C1R and C2R, were filled with CH_4.

The second element of the particle identification system was a Shashlyk-style electromagnetic calorimeter [17], and the third was a muon range stack of proportional tubes with plates of steel placed between each pair of planes. Four scintillator hodoscope planes (A,B,C,D) for triggering purposes and a scintillator pixel detector used at lower intensities completed the apparatus.

With these components, electron identification was assigned to tracks having appropriate light in the Cherenkov counters and energy deposition in the calorimeter consistent with their momentum. Pions were identified as having no light in the Cherenkov counters, energy deposition in the calorimeter consistent with a minimally ionizing particle or a hadronic shower, and depth in the muon stack less than the range predicted by the measured momentum. Muons were tagged as tracks with no light in their respective Cherenkov counters, energy in the calorimeter consistent with minimum ionization, and penetration depth in the muon stack consistent with muon range.

A list of the detector parameters is displayed in Table 1.

A right-handed coordinate system is used with the origin in the center of the upstream entrance of the first dipole (D5). The z-axis points in the beam direction, the y-axis points upwards, and the x-axis points to the left side.

In the following sections detailed descriptions of the construction and performance of the various detector elements are given. These are followed by a description of the overall apparatus performance.

2. The K^+ beam

The beam design maximized the kaon flux both in absolute terms and relative to other beam constituents and provided good collimation and shielding in order to reduce the muon halo resulting from copious decays of beam pions and kaons. A beam momentum of 6 GeV/c was chosen in order that beam particles were below the threshold for Cherenkov radiation in hydrogen at atmospheric pressure since the latter was an essential component for particle identification and triggering. 6 GeV/c also corresponds to the maximum of the K^+ production spectrum for 24 GeV/c primary protons. Although an electrostatically separated beam would provide a substantial reduction in pions, protons and muons, such a beam would yield a factor of 10 less kaon flux than the present design for the same number of protons on target.

The AGS typically delivered $(0.9–1.1) \times 10^{13}$ primary protons to the A Target in a spill of 1.6–2.8 s with corresponding cycle times of 3.6–5.1 s. Beam structure during the spill was highly variable and at times limited the intensity that E865 could accept. Auto-correlation measurements indicated a strong 100 KHz component in the structure. Rebunching the beam with the 100 MHz longitudinal phase space dilution cavity during the 1998 run greatly improved the good data through-

Table 1
List of detector parameters

Magnets (D5, D6)	D5	D6
Charged particle spectrometer		
Function	Charge separation	Momentum analysis
B_y^{max}	0.502 T	0.575 T
Volume	$1.22 \times 0.61 \times 1.22$ m^3	$3.05 \times 1.27 \times 0.91$ m^3
p_t(kick)	0.240 GeV/c	0.255 GeV/c
$\int B_y\, dl$	0.80 Tm	0.82 Tm

Proportional chambers (P1–P4)	P1	P2	P3	P4
Spacing	2 mm	2 mm	2 mm	2 mm
Number of planes/wires	4/3360	4/3360	4/6336	4/6840
Anode-to-cathode spacing	5 mm	5 mm	5 mm	5 mm
Total area	160×80 cm^2	160×80 cm^2	300×140 cm^2	320×160 cm^2
Dead area	19×9 cm^2	30×10 cm^2	55×16 cm^2	70×26 cm^2
Wire orientation	0°, 90°, +19.4°, −19.4°			
Spatial resolution	$\sigma_x = 0.35$ mm, $\sigma_y = 0.52$ mm			
Momentum resolution (p in GeV/c)	$\sigma_p/p = 0.28\%p$ ($p = 3$), $0.32\%p$ ($p = 2$), $0.48\%p$ ($p = 1$)			

Electromagnetic calorimeter	
Granularity	114×114 mm^2
Number of modules/fibers/layers	582/83, 808/60
Depth	0.33 m = 15 radiation lengths
Thicknesses: scintillator, lead	4.0 mm, 1.4 mm
Total area (beam hole)	3.32×2.28 m^2 (0.68×0.34 m^2)
Spatial resolution	$\sigma_x = \sigma_y = 15$ mm
π/e rejection	$3\% < \varepsilon_\pi/\varepsilon_e < 13\%$ for $3 > p_e(p_\pi) > 1$ GeV/c
Energy resolution	$\sigma(E_e)/E_e = 7.6\%/\sqrt{E_e} \oplus 3.5\%$
Timing resolution	$\sigma_t = 350$ ps at $E = 1$ GeV
Stability of response	$\sigma_E/E = 1.7\%$

Particle identification		
Gas Cherenkov counters (C1, C2)		
Volume	C1: $3.0 \times 1.6 \times 1.2$ m^3	C2: $3.2 \times 1.6 \times 1.6$ m^3
δ-ray threshold	30 MeV/c	
Timing resolution	$\sigma_t = 0.65$ ns	
	e^- side (left) H_2	e^+ side (right) CH_4
Thickness	320 mg/cm^2	390 mg/cm^2
Threshold	$p_\mu = 5.7$, $p_\pi = 7.6$ (GeV/c)	$p_\mu = 3.2$, $p_\pi = 4.2$ (GeV/c)
Misidentification probability[a]	$P(\pi^- \text{ as } e^-) = (2.6 \pm 0.1) \times 10^{-6}$	$P(e^+ \text{ as } \pi^+) = (1.7 \pm 0.7) \times 10^{-5}$

Muon identifier		
Total area (beam hole)	4.20×2.10 m^2 (0.42×0.42 m^2)	
Number of planes/tubes	12 horizontal, 12 vertical/14,592	
Wire spacing	1.3 cm	
Spatial resolution	$\sigma_x = \sigma_y = 5$ mm	
	Low threshold (16 planes)	High threshold (24 planes)
Iron absorber	40 cm	75 cm
Threshold	0.8 GeV/c	1.3 GeV/c

Table 1 (*continued*)

Scintillators				
Hodoscopes (A, B, C, D)	A	B	C	D
Total area	3.20×1.71 m^2	3.42×2.10 m^2	3.42×2.10 m^2	2.00×0.80 m^2
Beam hole	0.70×0.34 m^2	0.68×0.53 m^2	0.46×0.46 m^2	0.70×0.34 m^2
Number of elements	30	48	48	20
Timing resolution	$\sigma_t = 0.55$ ns			
Beam pixel array				
Pixel size	$7 \times 7 \times 2$ mm^3			
Number of elements	12 horizontal × 32 vertical			
Timing resolution	$\sigma_t = 1.2$ ns			

[a] The values quoted include the contribution from the electromagnetic calorimeter [60,61,63].

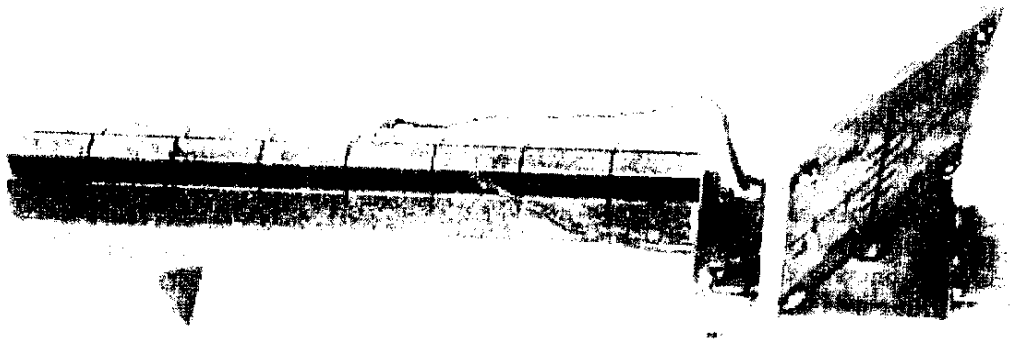

Fig. 2. The production target: The 5×5 mm^2 cross-section region on top of the heat sink is the target. The whole assembly is 275 mm long. The heat sink contains an internal water path for cooling. The target has transverse slots machined for stress relief. The wires are connected to thermocouples which are remotely monitored for protection against overtemperature. A fluorescent screen (AlO_3) is mounted upstream of the target at 45° to the primary proton beam direction and is viewed by a video camera through a 90° port in the shield wall.

put and resulted in much cleaner events as a result of the marked reduction in accidentals.

The production target was one interaction length (15 cm) of copper with transverse dimensions of 5 mm × 5 mm machined from a single billet of copper with the bottom of the target tapering outward to form a water cooled heat sink as shown in Fig. 2. Transverse slots were machined in the target to relieve stress due to thermal expansion from deposition of beam energy.

The intensity, size and position of the primary proton beam were monitored by a secondary emission chamber (SEC), a segmented wire ionization chamber (SWIC) with 1 mm wire spacing in the horizontal and vertical planes and a telescope consisting of three scintillation counters viewing the target through a well-collimated port in the shield wall at 90° to the primary beam direction. The ratio of telescope rate to that of the SEC provided a useful indication of the quality of targeting while the SWIC display produced horizontal and vertical beam positions and profiles. A fluorescent flag mounted on the target assembly was viewed by a video camera through a periscope and the 90° port. The beam-monitoring information was continuously available to the

AGS Main Control Room and the experimental counting house on a pulse to pulse basis.

The target was viewed by the 6 GeV/c beam at a central production angle of 3.5° corresponding to the angle at which the π^+ to K^+ ratio is a minimum according to the Sanford–Wang [18,19] parameterization of particle production. The acceptance was calculated by Monte Carlo simulation to be $\Delta\Omega\Delta P = 0.2$ msr-GeV/c. The estimated beam fluxes for positive kaons, pions and protons are 7×10^7, 1.6×10^9 and 1.2×10^9, respectively, for a typical spill of 10^{13} protons on the one interaction length target. A major concern was the accidental coincidences caused by the muon halo from pion and kaon decays in the beam which would dominate the charged particle rate within the experimental acceptance. The halo was suppressed by tight collimation in the upstream section of the beam and at two intermediate foci followed by dipole magnets which swept momentum-degraded muons out of the accepted phase space.

Fig. 3, a plan view of the beam line configuration, shows the positions of the various components. A dispersive front end, consisting of dipole magnets D1 and D2, bends 6 GeV/c beam particles by 6.5° and 4.75°, respectively, which with the 3.5° central production angle separated the new 6 GeV/c beam, A2, from an existing 0° high-energy beam, A1/A3. Since the design of the experiment requires the beam to pass through the detection apparatus, it was essential to minimize the size of desensitized regions of the proportional wire chambers and beam holes in the scintillation counter arrays and the electromagnetic shower calorimeter in order to maintain good acceptance. The collimation was designed to minimize the tails of the beam distributions, which are primarily muons, at the locations of the various detectors in order to limit their contribution to the accidental rates.

Two quadrupole doublets Q1/Q2 and Q4/[Q5 + Q6] produce momentum dispersed and momentum recombined double foci at Q3 and Q7, respectively. Q3 and Q7 are field lenses with specially shaped vertical and horizontal collimators in their apertures to attenuate muon halo. The Q8/Q9 doublet produces the final focus in the vicinity of the proportional wire chambers P1 and P2, 35 m downstream of the production target. The length of the beam from the production target to the beginning of the 5 m vacuum decay region is 28.1 m.

A Hevimet collimator in D1 was designed to approximate a curved channel defining the horizontal acceptance for 6 GeV/c charged particles in the 2.4 T magnetic field of D1 while reducing the flux of muons from decays in the vicinity of or immediately downstream of the production target, e.g., $K^0_S \to \pi^+\pi^-$. The vertical gap of D1 was reduced to 33 mm by the addition of magnet steel

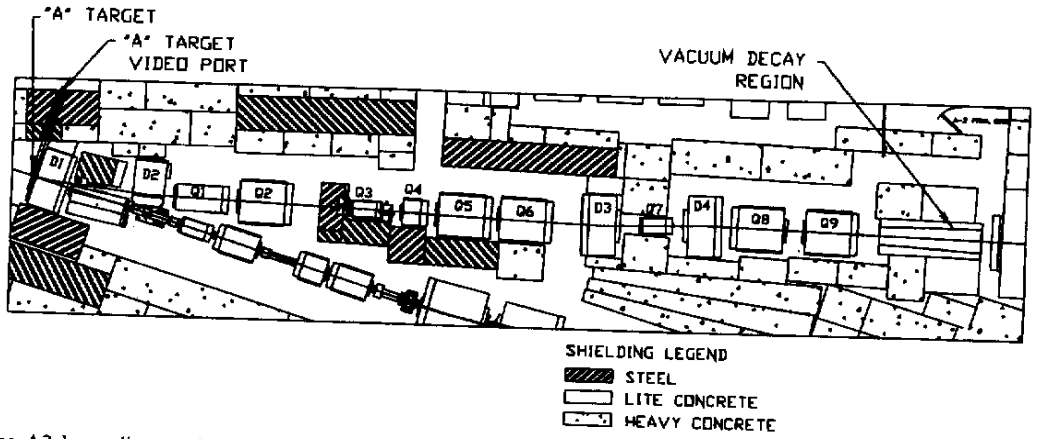

Fig. 3. The A2 beam line configuration: the shielding and magnet locations are shown with the A production target, the beam monitoring port and the vacuum decay region on the AGS experimental floor.

e beam to pass through the
, it was essential to minimize
ed regions of the proportional
beam holes in the scintillation
the electromagnetic shower
to maintain good acceptance.
designed to minimize the tails
ions, which are primarily mu-
of the various detectors in order
ution to the accidental rates.
e doublets Q1/Q2 and
ice momentum dispersed and
ied double foci at Q3 and Q7,
d Q7 are field lenses with
tical and horizontal collima-
to attenuate muon halo. The
duces the final focus in the
tional wire chambers P1 and
n of the production target.
n from the production target
e 5 m vacuum decay region is

tor in D1 was designed to
d channel defining the hor-
6 GeV/c charged particles
field of D1 while reducing
n decays in the vicinity of or
am of the production target,
e vertical gap of D1 was
he addition of magnet steel

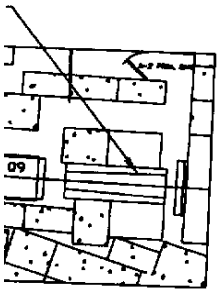

A production target, the beam

the poles. A vertical Hevimet collimator tapered
± 11 mrad was installed in the downstream
hird of the magnet to define the vertical accep-
ance. A fixed collimator in Q1 whose surfaces
ere tapered to correspond to the shape of the
alculated beam envelope further reduced beam
alo.

Horizontal collimators upstream (low momen-
um) and downstream (high momentum) of Q3
ere remotely adjustable to define the momentum
pread and intensity of the hadronic component of
he beam while degrading the momenta of muons
the halo so that they are swept out of the beam
ceptance by D3 and D4. A vertical collimator in
he aperture of Q3 was tapered to fit the calculated
eam convergence and divergence of 15 mrad at
he focus in Q3. The line of minimum vertical
perture followed a horizontal diagonal from
pstream on the low momentum side of the
ispersed beam to downstream on the high
omentum side corresponding to the locus of
ertical foci as a function of transmitted momen-
um. The initial tuning of the beam was carried out
ith a pair of coaxial scintillation counters of
ertical sizes corresponding to the full and one-
alf minimum vertical beam size centered on the
ertical midplane immediately upstream of the line
minimum vertical aperture. Optimizing the ratio
f the beam rates of the smaller to the larger of the
wo counters with Q2 while maintaining Q1 at its
alculated value assured a vertical focus. The
xperimentally determined optimum value of the
)2 excitation agreed with the prediction obtained
y Monte Carlo simulation with magnet measure-
ents to 0.5%.

Further halo reduction was achieved with a
xed collimator in the aperture of Q7 where the
eam is focussed in both planes and momentum
combined. The inner surfaces of this fixed
ollimator were shaped to be 2 mm beyond the
alculated beam envelope. The focussing of Q4
nd Q5+Q6 was determined with a SWIC with
mm wire separation which provided horizontal
nd vertical beam profiles immediately down-
tream of Q7. After minimizing the images on
le SWIC, the doublet excitations were increased
y the calculated amount required to move the foci
the center of Q7. The magnet excitations
corresponding to the optimum SWIC images were in excellent agreement with the calculated values. The horizontal and vertical SWIC images were observed to be 16 ± 4 mm and 14 ± 4 mm rms, respectively, compared with the simulation prediction of 13 mm rms in both planes.

The chromatic aberration due to the successive foci and the momentum band accepted by the beam determines the spot size at the final focus. The Q8/Q9 excitations were chosen to minimize the size of the beam in the proportional wire chambers P1 and P2. A 64 mm SWIC with 2 mm wire spacing was temporarily installed in the beam at the location of the first proportional wire chamber P1, and Q8/Q9 were set to produce the smallest image at their calculated values for this location. Further tuning of Q8 and Q9 minimized the beam rates in the wire chambers. The measured images were 32 ± 3 mm and 16 ± 2 mm rms, somewhat larger than the simulation values of 25 and 12 mm rms in the horizontal and vertical planes, respectively. Fig. 4 displays ray traces in the horizontal and vertical planes for on-momentum and $\pm3\%$ trajectories at the limits of the angular acceptance.

An ionization chamber of 18 cm diameter installed in the secondary beam dump was an excellent secondary beam monitor and provided a stable normalization for the various trigger rates.

The Monte Carlo simulations predicted muon halo rates of 2.8×10^{7} accompanying 7×10^{7} kaons and 2.8×10^{9} π^{+} and protons in the beam per 10^{13} protons on target; the largest contribution to the total charged particle rate of 3.6×10^{7}. This was in good agreement with the 3.0×10^{7} muons observed per spill. The total beam rate was determined during the 1994 engineering run by extrapolating the rate obtained in a beam hodoscope temporarily installed during beam tuning with an 0.1 interaction length target and 1.5×10^{12} primary protons/pulse on the A Target.

Event rates are also in good agreement with the Monte Carlo predictions as determined from normalization to the well known decays $K^{+}\to\pi^{+}\pi^{+}\pi^{-}$ and $K^{+}\to\pi^{+}\pi^{0}$ followed by $\pi^{0}\to e^{+}e^{-}\gamma$ after live time and detector efficiency corrections.

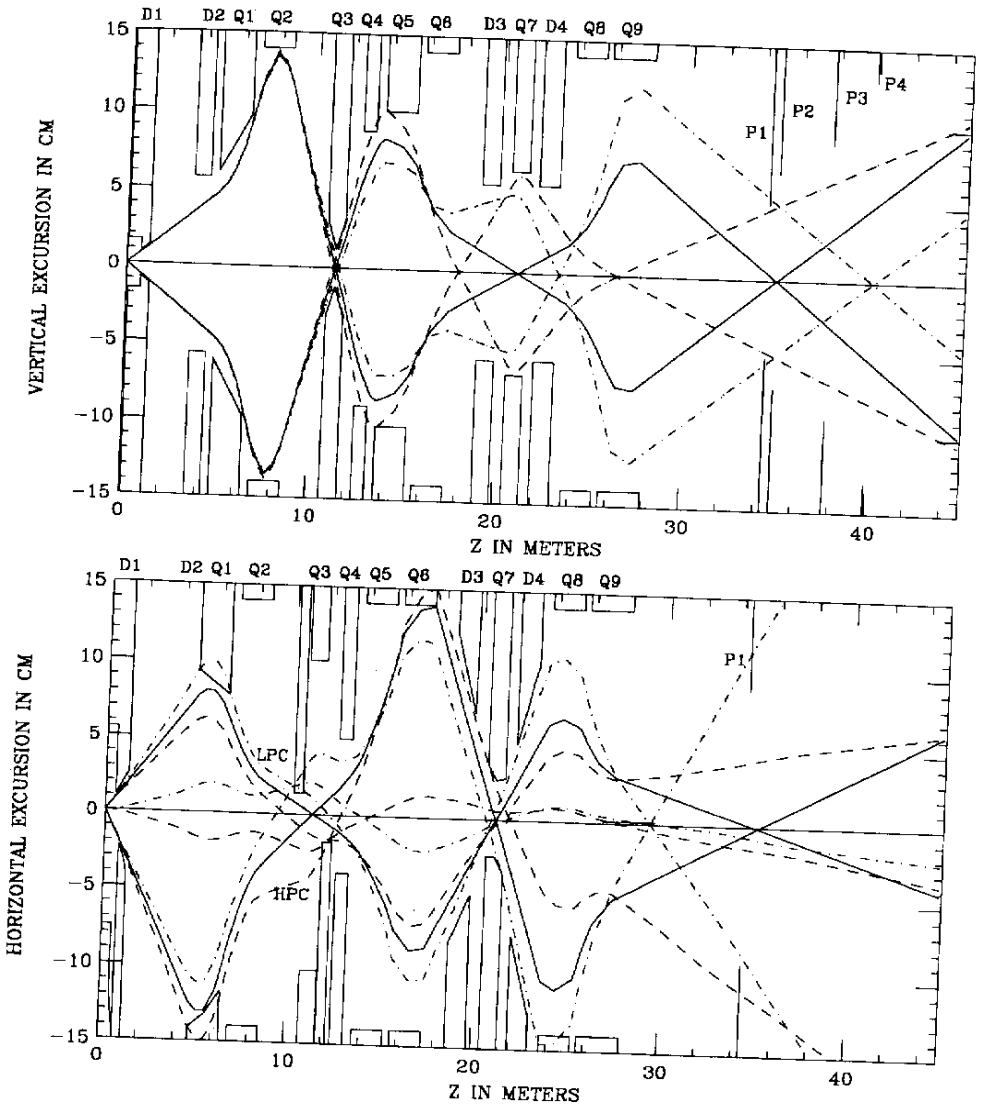

Fig. 4. Horizontal and vertical ray traces: rays originating at the center of the production target at the center and extremes of the acceptance with momenta, $P = (1 \pm 0.03)P_0$ are traced. On momentum trajectories are indicated by solid lines while $\pm 3\%$ paths are given by dashed and dot–dashed patterns, respectively. The magnet apertures are indicated with the fixed collimators in the dipole magnets D1, D3 and D4, and the quadrupoles Q1, Q3 and Q7. The adjustable high and low momentum collimators, LPC and HPC, and the sensitive regions, i.e. outside the beam region, of the multiwire proportional chambers P1–P4 are displayed.

3. Scintillation counters

3.1. Pixel detector

The pixel detector, which was located in the beam immediately upstream of the vacuum decay region, was used for tracking beam particles in a series of precision experiments at reduced intensity in 1997. The 2 mm thick, 7 mm × 7 mm Bicron BC-418 scintillators were configured in a 12 (horizontal) by 32 (vertical) array viewed by air light guides to allow a better determination of the

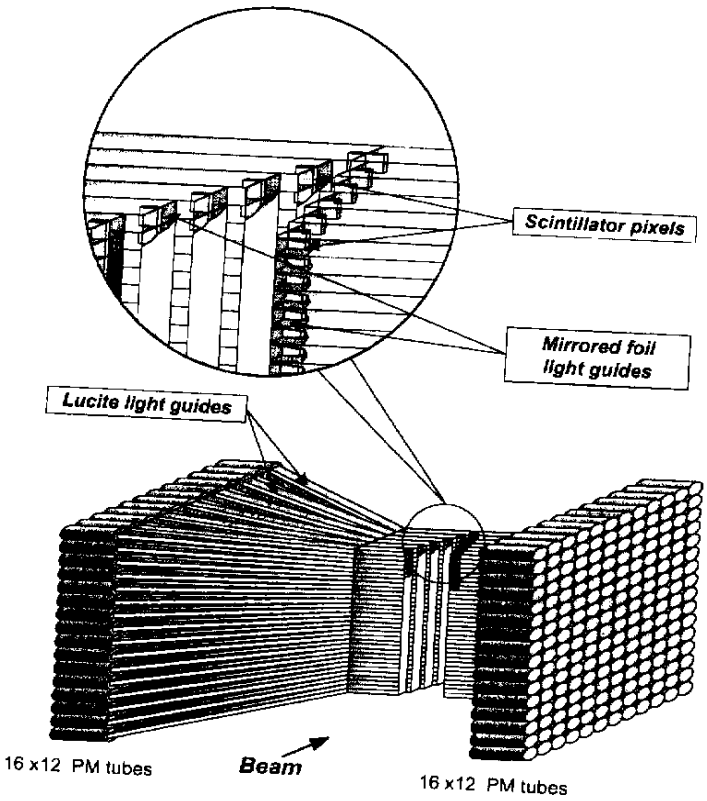

Fig. 5. Scintillator pixel detector

initial K^+ trajectory and thus increase the precision for kinematic reconstruction of decays with an unobserved neutrino. Fig. 5 shows the scintillator array. The pixels were horizontally displaced 7 mm transverse to the beam in each successive layer in depth so that they were not covered by the mirror-lined air light guides of the adjacent scintillator. The length of the air light guides therefore varied from 76 to 111 mm. The latter were then coupled through lucite light guides outside the beam region to the FEU115 photomultipliers, each of which had 11 stages and a 25 mm diameter.

Pixel size was optimized by using simulated kaon decays into three charged pions to determine the spatial distribution of reconstructed kaon trajectories at the pixel array relative to that of the generated kaon position. The measured vertex reconstruction resolution and the requirement that the reconstructed kaon tracks back to the production target were similar to the constraints applied to the data. The track distributions gave a resolution of $\sigma_x = \sigma_y = 5.5$ mm over the 84 mm (horizontal) by 224 mm (vertical) area. This indicated that little improvement could be expected by going to finer segmentation than 7 mm. The combined timing resolution averaged over all elements was $\sigma_t = 1.3$ ns. This allowed us to operate the pixel detector in a beam intensity of 2×10^8 particles/s distributed over a 100 mm × 200 mm area with an efficiency of 91%.

Fig. 6 shows how the reconstruction of the missing mass spectrum for K_{e4} events benefits from the pixel counter information.

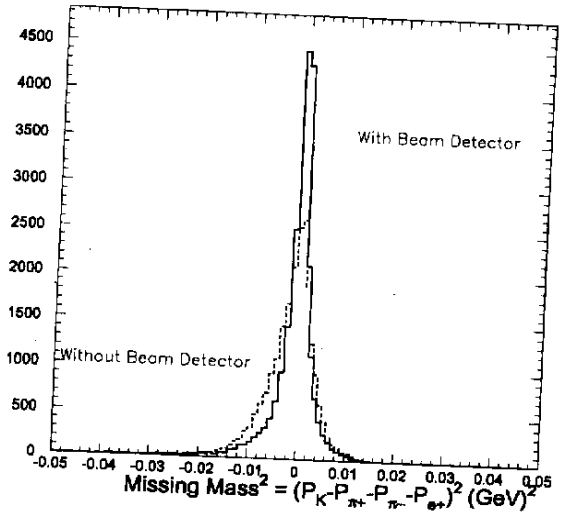

Fig. 6. K_{e4} missing mass spectrum with and without the pixel counter information. The dashed curve was obtained assigning the nominal momentum to the K^+ and assuming the center of the beam line for its direction. The solid curve obtained the K^+ direction from the pixel and the reconstructed vertex.

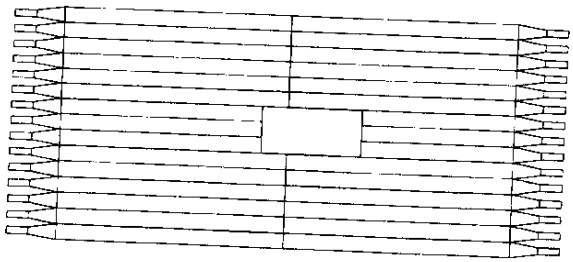

Fig. 7. Downstream view of the scintillator arrangement in the A hodoscope.

3.2. Trigger hodoscopes

Four hodoscopes were used in the apparatus. One of these, the A hodoscope, was used in the lowest-level trigger. It consisted of 30 elements, 11.4 cm wide and 1 cm thick mounted horizontally, viewed by Phillips XP2262 phototubes. Most elements were 160 cm long. However, six elements in the region of the beam were shorter, as shown in Fig. 7. Bicron 408[20] scintillator was chosen for its long attenuation length (380 cm) combined with a fast decay time (2.1 ns).

[20] Bicron Corp., Newbury, Ohio.

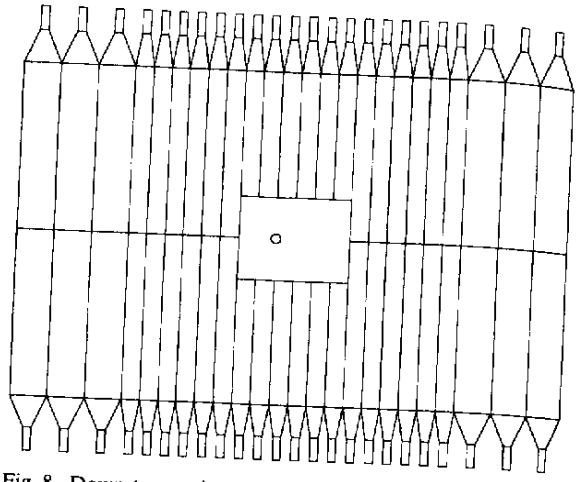

Fig. 8. Downstream view of the scintillator arrangement in the B hodoscope.

The B and C hodoscopes were used in the muon stack as part of the muon trigger. Each contains 48 elements, 11.4 cm wide and 1 cm thick Bicron 408, mounted vertically. Fig. 8 shows the layout of the B hodoscope; the elements in the region of the beam were again shortened. The C hodoscope was similar except that only 10 (rather than 12) elements were shortened. The scintillators were viewed by EMI 9814 phototubes. For all hodoscopes the ends of the scintillators remote from the phototubes were roughened and painted black to suppress the reflected light pulse.

The D hodoscope was added in 1995 as a part of the lowest-level trigger. It is located between wire chambers P1 and P2 and consists of 20 elements, 3 mm thick. Its main function was to ensure that at least two charged particles emerge from the decay volume, thus protecting against triggers that arise from interactions of beam particles within the apparatus.

The time resolution of the hodoscopes was dominated by the spread in light transit time along the length of the scintillators. However, for the crucial coincidence, between the A hodoscope and the shower counter, this transit-time spread was compensated by a specially built circuit that delayed the A-hodoscope signal by an amount appropriate for each shower-counter module,

thereby achieving a resolving time of about 1.5 ns. For this reason, the A hodoscope was mounted as close as possible to the shower counter, to give good spatial correlation between the hit positions in these two detectors. The operation is described in Section 7.2.

4. Charged particle spectrometer

4.1. Magnets

Two large magnets were used for the spectrometer. The first one, D5, separated positively from the negatively charged particles. Its horizontal aperture is 122 cm wide and 122 cm deep along the beam axis. The vertical gap is 61 cm. The line integral of its vertical field, measured in units of transverse momentum deflection (p_t-kick) was 240 MeV/c. D6, the second spectrometer magnet horizontal aperture is 305 cm, it is 91 cm long and has a gap of 127 cm with a p_t-kick of 255 MeV/c. The magnetic field components were mapped on a grid in 5 cm steps using Hall probes. The map starts about 1 m upstream of the entrance of D5 and ends 10 cm downstream of P4. Fig. 9 shows the magnetic field components B_y and B_z.

4.2. Multiwire proportional chambers

The two primary design criteria for the tracking devices were adequate spatial resolution, high rate capability and availability of the spatial information in the trigger. It was expected that about 50 MHz of secondary particles originating from decays or aperture scattering of the beam particles pass through the chambers in addition to the beam flux in the center. Multiwire proportional chambers (MWPC) rather than drift chambers were chosen, because they provide better pattern recognition efficiency in a high rate environment, albeit at less spatial resolution.

To reduce the effects of inefficiencies, to control the combinatorial ambiguities due to random hits, to improve the position resolution, and to

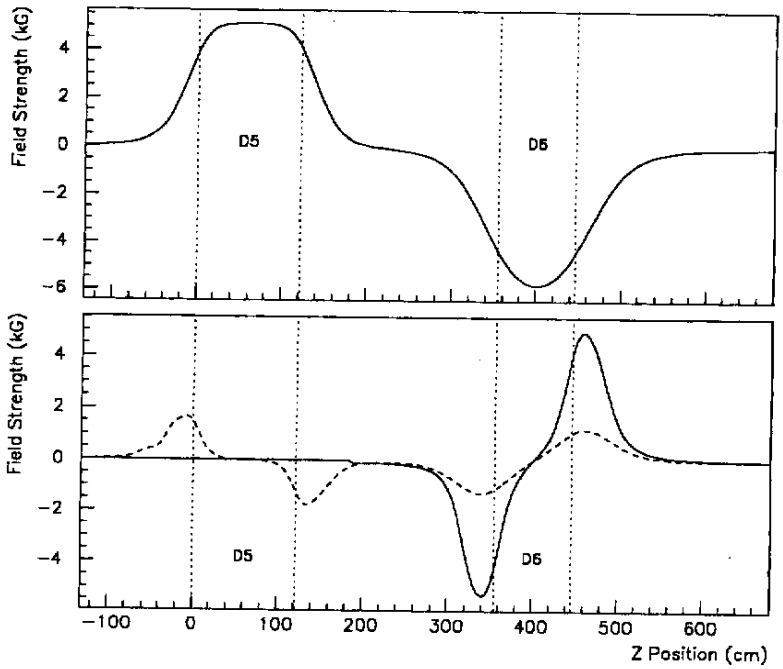

Fig. 9. Magnetic field components B_y (top) and B_z (bottom; $y = 45$ cm: solid line; $y = 15$ cm: dashed line) along the beam direction.

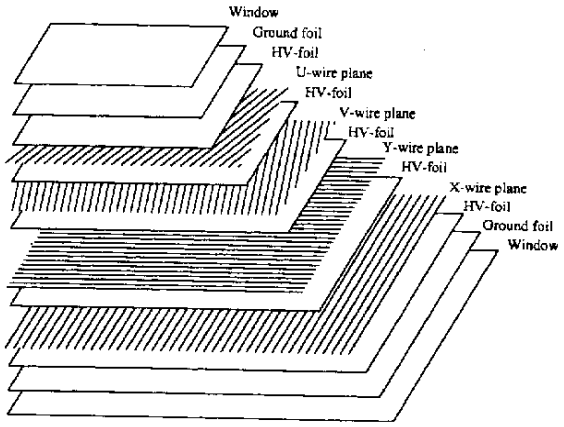

Fig. 10. Details of one of the multiwire proportional chambers showing schematically the sequence of wire and high voltage planes, ground foils and gas windows.

determine the positions unambiguously we opted for four planes per chamber each with different orientation. Experience with a previous experiment [20] showed that four planes are necessary to have enough redundancy, while contributions from multiple scattering to the resolution are still tolerable. Fig. 10 shows the arrangement schematically.

The accuracy of the position measurement depends on the anode wire spacing. Since for comparable gas gain the potential difference between the anode and the cathode has to be increased if the wire spacing is decreased, spacings of less than 2 mm make large chambers difficult to operate. Decreasing the wire diameter helps for smaller devices, but mechanical and electrostatic limitations [21] prevented this in our case.

To handle the high rates the time window during which pulses from the chamber are accepted has to be as short as possible, preferably of the order of 20 ns. This requires small distances between the anode wires, a narrow anode to cathode gap and a chamber gas with high electron drift velocity. To minimize space charge effects, a gas with a high ion mobility is needed with good aging properties. To keep the windows thin the chamber has to operated at atmosphericpressure.

Efficiency considerations and mechanical tolerances, i.e. the difficulty to maintain a uniform gap for such a large chamber and to avoid variations in gain [21], suggest larger gap sizes, which lead to the compromise of a 5 mm gap. Following a technique described previously in Ref. [22], the beam region was kept at a lower high voltage at the cathode planes than the active area of the chamber, and thus rendered insensitive. Graphite cathode planes were chosen because of their known good aging characteristics.

4.2.1. Mechanical construction

The dimensions of the four chambers are summarized in Table 1. Each chamber consists of four anode wire planes, each corresponding to a different orientation of the wires: horizontal, vertical and inclined at $\pm 19.4°$ with respect to the vertical direction, five cathode planes, two ground planes and two gas window planes supported by an aluminum (P1/P2) or steel frame (P3/P4) (see Fig. 10). In the following we describe in detail the construction of the two smaller chambers (P1/P2) (Fig. 11) first, and then summarize those aspects where the construction of the larger chambers (P3/P4) differed.

The anodes were made of gold-plated tungsten wires (diameter $2a = 20\ \mu m$)[21] with a spacing of $s = 2$ mm. The gap width is $l = 5$ mm. The wires were soldered at both ends to gold-plated Cu pads on printed circuit boards about 1 cm from the inside edge of the frame (Fig. 12). On one side, the printed circuit was extended to the outside edge where the connectors for the readout electronics were mounted. The printed circuit boards were glued to a glass-fiber-reinforced epoxy frame (Stesalit[22]). The first wire of a plane was positioned relative to reference points on the frame using an optical measuring tool. For the following wires a comb with a spacing of 2.0 ± 0.0002 mm was used. After 200 wires the position was again checked optically against the reference point. The wires were soldered without flux agent with a special 140°C melting-point solder. To reduce the electrical field at the outermost edge three wires with

[21] Wire type 761 manufactured by LUMALAMPAN AB, Kalmar, Sweden.

[22] Glass fiber reinforced epoxy: Stesalit AG, Zullwil, Switzerland; and Permali, F 54320 Marseille, France.

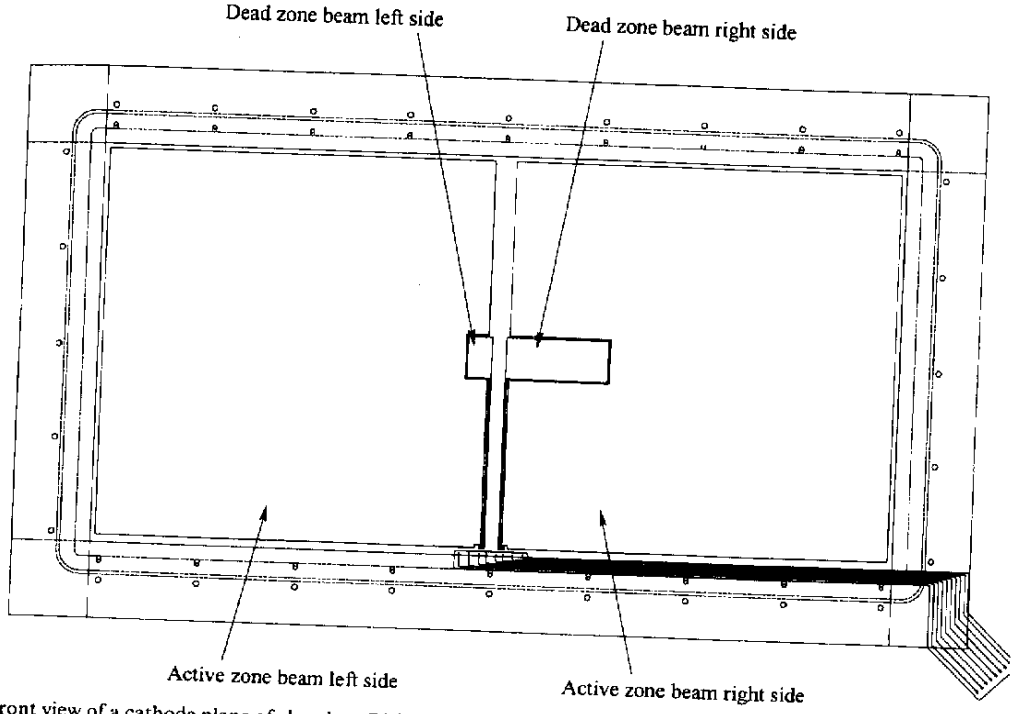

Fig. 11. Front view of a cathode plane of chambers P1/P2. Shown are the graphited surfaces, the frame with the O-ring groove and the high voltage leads to the active and deactivated zones.

increasing diameter (30, 50 and 100 μm) were added.

The wires used break at a tension of $T = 0.9$ N [23]. Our wires were strung on a transport frame using a wiring machine at a tension $T = 0.7$ N, and then transfered to the chamber. For the vertical wires with a typical length, $L = 80$ cm, the maximum potential difference to the cathode V_c, which can be applied before the anode wires are displaced, is given in Ref. [21]

$$V_c = \frac{s}{CL}\sqrt{4\pi\varepsilon_0 T} = 4485 \text{ V}$$

$$\text{with} \quad C = \frac{2\pi\varepsilon_0}{\pi l/s - \ln(2\pi a/s)} = 4.92 \text{ pF/m}. \quad (3)$$

For the horizontal wires, which are twice as long, $V_c = 2243$ V is the maximum voltage allowed, which is well below the operating voltage. These wires were therefore supported by a 3 cm wide and 0.2 mm thick printed circuit board glued with a double-sided tape to a 3 cm wide and 50 μm thick Kapton foil.[23] This support structure was clamped to the Stesalit frame and the horizontal wires were soldered to the board and then cut in the middle. This structure not only supported the wires but also separated the horizontal wires into a left and a right side. The tension of the wires was monitored electronically by measuring the resonance frequency of the wires and a mean value of 0.681 N with a spread of 0.017 N was found.

The cathodes were made of 50 μm thick Mylar foil.[24] The foils were stretched by pulling them around the edges into an evacuated groove. Then they were glued on Stesalit frames with Araldit[25] and sprayed twice with high resistance graphite. The surface was polished after each spraying

[23] Kapton (Polyimid), Du Pont International S.A., 1218 Geneva, Switzerland.

[24] Mylar (Polyester), Du Pont International S.A., 1218 Geneva, Switzerland.

[25] Araldit epoxy glue manufactured by CIBA-Geigy AG, Basel, Switzerland.

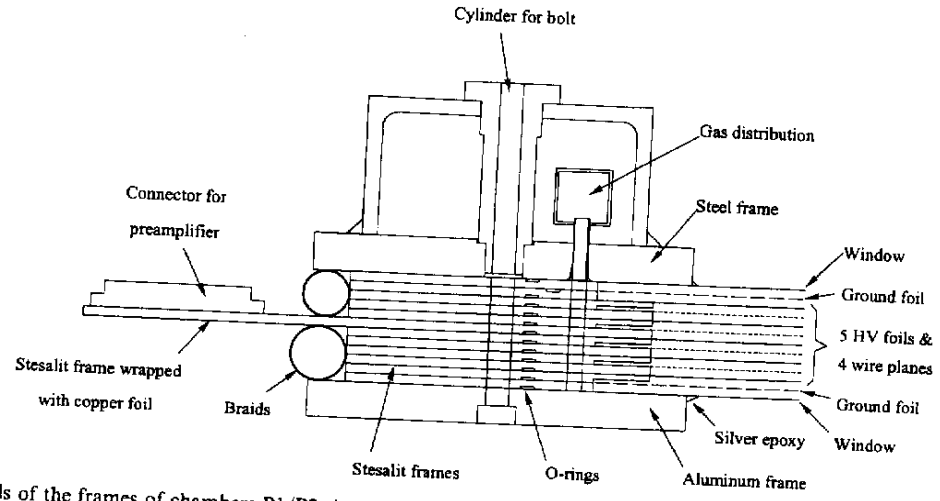

Fig. 12. Details of the frames of chambers P1/P2 showing the sequence of windows, wire and high voltage planes, the gas inlet and distribution, the printed circuit boards and the electromagnetic shielding (see text for further information).

process. At the end the graphite layer was approximately 40 μm thick and the resistance was 1.7 kΩ per square after 1 h heat treatment at 100°C. The graphite layer was made from a mixture of DAG502[26] and isopropanol in the ratio 1 : 1. Before the spraying process, a mask was applied to the foil in order to define the conductive surface. The graphite layer was divided into four electrically separated areas (Fig. 11). All the edges of the graphite zones were rounded, removing the graphite with isopropanol. The borders were cleaned with an ordinary pencil eraser and polished with Q-tips. The zones separating the graphite areas were cleaned with isopropanol, too. No high voltage breakdown from the front to the back side of the Mylar foil was observed up to 6 kV difference and up to 3.5 kV could be applied across the 3.5 mm gap between the graphite areas. A printed circuit was used to supply the cathodes with negative high voltage (Fig. 11). A flattened copper wire glued to the graphite with conductive epoxy[27] connected the graphite with the printed circuit.

Each graphite area can be fed individually with high voltage. The voltage at the two central zones can be lowered to reduce charge amplification in the gas. The cathodes are protected with 512 kΩ resistors to allow a high voltage degradation in case of a spark between the electrodes or a broken wire. The frames of the electrodes are not self-supporting. They are therefore assembled between a 2 cm thick aluminum frame and a 2 cm thick steel frame stiffened by a U-channel (Fig. 12). Twenty-eight precisely drilled holes. We ascribe this effect to shortcomings of the alignment, the imperfect in the support frames and in the Stesalit frames fix the position of electrodes with respect to the chamber reference system. The chamber was assembled by means of 28 hollow steel bolts which were passed through the holes. This system allows the chamber to be easily opened and direct access to each electrode using expandable dowels.

The chamber windows consist of 12.7 μm aluminized Mylar foil. The aluminum layer serves both as a barrier for water vapor and a shield against electronic noise. This foil is glued with Araldit to the aluminum and steel frames. The aluminum foils and the frames are connected electrically by a silver epoxy lining in the corner between frame and foil (Fig. 12). All parts of the Stesalit frames extending out of the chamber are

[26] DAG 502 manufactured by Acheson Colloiden, Scheemda, Netherlands.

[27] Elecolit 340, 3M (Schweiz) AG, 8803 Rüschlikon, Switzerland.

wrapped with a copper foil. The electric shields of each frame are interconnected with metallic braids passed around PVC-tubing and pressed into the empty space between the frames (Fig. 12), resulting in a complete Faraday cage.

An open-loop gas system flushes the MWPCs. The gas tightness is secured by conventional O-rings, glued into a groove in each Stesalit frame. This requires double-sided circuit boards to read out the anode wires, i.e. boards with copper lines, which connect the wires to the connector so that the O-ring does not have to seal an uneven surface.

Two additional 50 μm thick mylar foils (ground foils) sprayed on one side with a graphite and connected to ground are added to the package (Fig. 12) to prevent the outermost cathode from sagging towards the anode because of electrostatic forces. Since the capacity between the ground foil and the cathode is larger than between the anode wires and the cathode, the high voltage of the graphite areas facing the ground plane is lowered to 80% of the voltage of the other active areas of the cathode.

The larger chambers, P3 and P4, differed in some aspects from the smaller chambers, P1 and P2. The chamber frames were manufactured from G10[28] in 4.88 mm thickness. The anode wires were strung[29] with a tension of 0.588 N. Nylon wires were threaded in pairs through the sense wires to prevent motion due to adjacent wire repulsion. On one end of each plane, the wires were soldered to the printed circuit boards. On the other end, they were directly glued to the G10 frame. To keep the anode wire plane stable against the electrostatic forces between the planes, garlands bent into zig-zag shapes [24] were introduced. These garlands, formed from a strip of mylar support an insulated wire. This metal surface was maintained at a potential of 1300 V. The outside ground plane was kept at fixed distance to the first high voltage plane using 12 nylon spacer buttons. The cathode planes of P3 and P4 were made using similar techniques to those used for P1 and P2. The surface resistance of the planes covered with graphite was higher (approximately 50 kΩ per square) and extensive polishing was required before the chambers could be made operational. The high voltage was supplied to the cathode through a line of silver epoxy from the connector at the frame. The front and back side of corresponding graphite-coated areas were shorted with pin holes through the mylar foil. The larger surface of the chambers also required 100 μm thick Mylar entrance and exit foils. The whole chamber package was sandwiched between two stainless-steel frames, 200 mm wide, made from 38 mm thick plates on the back side and stiffened with an 88 mm deep U-shaped aluminum channel on the front side, and bolted down with 25 mm bolts every 600 mm. Gas was fed in through several inlets on the top of the chamber and exited out at the bottom.

4.2.2. Electronics

The MWPC readout system was custom designed for this experiment in collaboration with industry (PCOS4) [25,26], and contains two chips, for which a block diagram is shown in Fig. 13.

The integrated circuit containing the preamplifier and the shaper (LeCroy MQS104) is implemented in a medium performance semi-custom bipolar process. The filtering consists of four poles and one zero. The output pulse width is 18 ns (FWHM) with 11 ns rise time and 23% undershoot. The undershoot is intended to cancel the long tail of the anode signal from the motion of the positive ions. The double hit resolution is less than 80 ns. The effective noise level is less than 3000 electrons, with protection elements and wire capacitance added to the input circuit. The transimpedance gain is 500 kΩ with differential output. Each chip contains four independent channels.

The second integrated circuit (LeCroy MDL108) combines the discriminator, delay element, coincidence gate and readout logic in an 8-channel BiCMOS chip. The discriminator threshold can be lowered well below the noise level. The discriminator is followed by a one-shot producing a fixed output pulse width. The delay element, which is used to adapt the timing of the individual channels to the timing of the coincidence gate sent

[28] G-10-CR Natural Spauldite, Spaulding Composites Co., Tonawnada, NY 14151-0616.

[29] The loan of a winding machine from CERN is gratefully acknowledged.

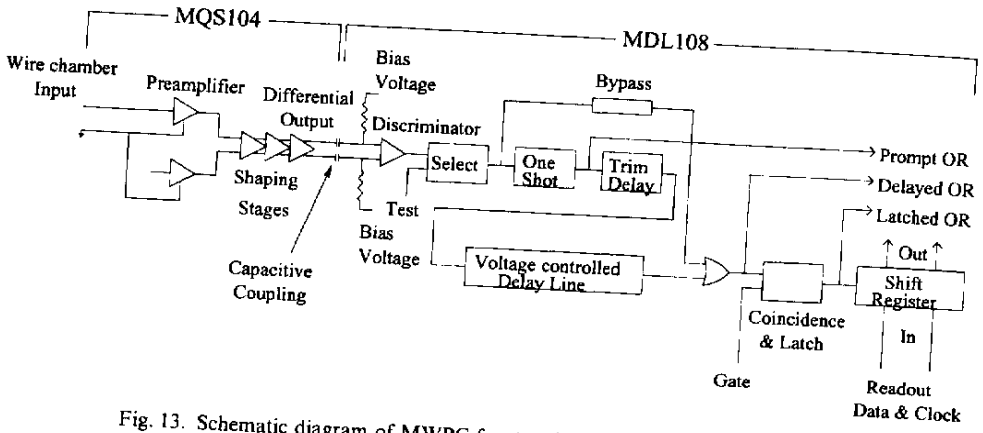

Fig. 13. Schematic diagram of MWPC front end electronics (LeCroy PCOS4).

by the trigger, can be adjusted from 330 ns to 1 μs. The first section of the delay is a trim section with 16 fixed steps of approximately 1 ns. With these trim sections all channels of the chamber can be adjusted to the same delay with an accuracy of less than 2 ns. The actual delay line consists of 150 current-limited inverter stages, each with a minimum delay of 2 ns and a maximum of at least 6 ns. The delay lines are controlled by a phase lock loop and a ninth delay line, the reference delay, which is identical to the eight signal delay lines. In phase lock loop mode, a pair of gate pulses with a separation equal to the desired delay is input to the delay line. Detection circuitry determines whether the delay is greater or less than the desired delay and sets a direction bit accordingly. An initial calibration period with several thousand pulse pairs is required to set the proper value of the delay. Then a calibration every few seconds is necessary to track changes in temperature and power supply voltage. The coincidence is made in an edge triggered D flip–flop. The leading edge of the delayed one-shot output clocks the flip–flop, the coincidence gate is the D input. The output sets a simple set–reset flip–flop. During readout, the set–reset flip–flop output is transfered to a shift register. The shift register is nine bits long, one data bit for each of the eight channels and one parity bit to identify transmission errors. The system is designed to be read out at a 20 MHz shift rate. There are three OR outputs, a prompt OR (the OR of the eight one-shot outputs), a delayed OR (the OR of the eight delay lines outputs) and a latched OR (the OR of the eight set–reset flip–flops).

Four MQS104 and two MDL108 chips are combined on a card. This card is designed to be mounted on the chamber (plugged into the connector shown in Fig. 12). A second connector on the card plugs into a common motherboard. One to 16 of these cards (max. 256 wires) are connected to one motherboard and are organized in a daisy chain, with the readout linked together in one long shift register. This motherboard also distributes power, gate and fast clear signals. The power consumption of one channel is 285 mW. Setting up the system requires down-loading 16 bytes for each MDL108 chip, running the system in phase lock loop mode for adjusting the delays and returning to normal running mode. This task is accomplished by LeCroy 2748 Camac modules, which also provide an OR-output which is used in the fourth-level trigger (see Section 7).

4.2.3. Chamber performance

We operated the two smaller chambers with a 50% : 50% CF_4/isobutane gas mixture, the two larger chambers with a 79.5% : 20% : 0.5% argon/isobutane/CF_3Br gas mixture.

The CF_4/isobutane mixture was selected, because CF_4 is a fast gas [27], producing a large number of primary electrons [28], and if between 15% and 70% Isobutane is admixed, good aging properties are reported [29,30]. Since the drift

velocity increases with the fraction of CF_4, but the ion mobility decreases [31], equal fractions were used. The argon/isobutane/CF_3Br mixture has the advantage of higher gas multiplication and hence lower operation voltage. This was desirable to avoid mechanical deflections of cathode and ground planes in the larger chambers.

The chambers were carefully conditioned over a period of a few months, until the expected operation point was reached. During this process only four of the 6720 wires in P1 and P2 broke and were replaced. The main reason for the slow progress, however, was, that during the tests with a ^{241}Am source at different positions across the chamber self-sustained discharges with dark currents of up to 10 μA appeared. The source produced local ionization comparable to what was expected for the beam. When the source was removed the dark currents did not immediately quench by themselves, but continued to burn for a few hours. Once stopped the chamber could be illuminated with the source at the same position for many hours without the occurrence of any current. This Malter effect-like phenomenon [32] was observed more often at the edges of the graphite area than in the center, but disappeared during the exposure to beam.

The uniformity of the chamber gain was first tested by measuring the currents in the nA range induced by the ^{241}Am source in complete scan. No variations of more than 17% were found in any plane or between different planes. We then measured the gas gain at different positions with a ^{55}Fe source and a calibrated amplifier. Fig. 14 shows one of the curves. We also found with this method no variations larger than 15%, which implies that the gap uniformity is better than 1.25% (63 μm).

After this test, the chamber was installed in the experiment. A plateau curve for chamber P2 at nominal amplifier threshold is shown in Fig. 15. It was measured using high-energy muons originating from particle decays near the production target and passing through the secondary beam line apertures with all magnets switched off. Chamber P1 and the calorimeter were used for triggering. Under normal beam intensity, no increase of the

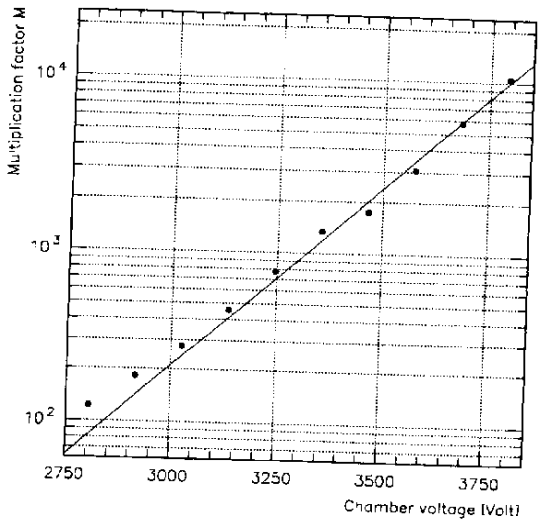

Fig. 14. Gas gain in P2 for 6 keV γ-rays in the 50–50% CF_4–iC_4H_{10} gas mixture.

efficiency could be observed by raising the high voltage above 3280 V and the voltage drop over the 512 kΩ protection resistors was less than 10 V. The chamber was operated most of the time at 3280 V. The dead zone voltage was set to 2600 V; no gas gain was observed at this voltage. Due to the high rate a few hits still occurred in this region, since the chamber operates as an ionization chamber.

P3 and P4 showed an efficiency plateau starting at 2650 V. These chambers were operated typically at 2700 V, corresponding to gas gains of 40,000 to 50,000.

Fig. 15 shows delay curves for various gate widths in CF_4–C_4H_{10} at 3280 V at nominal amplifier threshold. No delay calibration for the individual channels was done for this measurement. We operated P1/P2 with a gate width of 60 ns and P3/P4 with a gate width of 85 ns during the run in 1995. After the end of this run, and after calibration we narrowed the gate for P1/P2 to 40 ns and for P3/P4 to 60 ns, considerably reducing the accidental rate.

During the course of the experiment (1995–1998) the chambers were exposed to 7000 h of beam during 5 years equivalent to 10^{15} particles (upper limit), with 2.5×10^{14} passing the active area. This corresponds to a total charge of 81 C

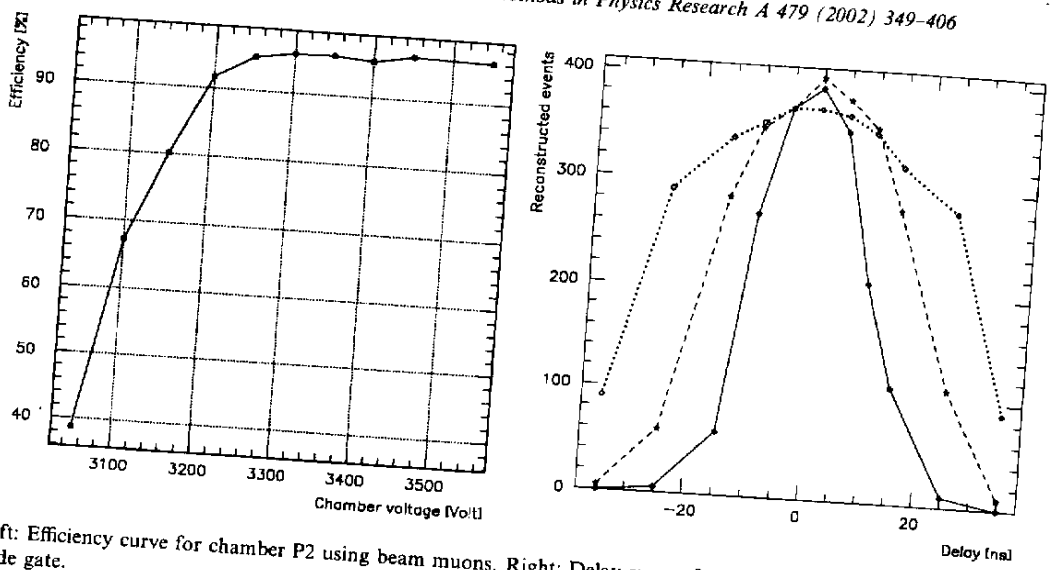

Fig. 15. Left: Efficiency curve for chamber P2 using beam muons. Right: Delay curves for a 40 ns (solid), 60 ns (dashed) and 75 ns (dotted) wide gate.

per plane. With this number we calculate for the wires in the most exposed region a total collected charge of 38 mC/wire/cm. No radiation damage, increase of leakage current or deterioration of efficiency has been observed on chambers P1, P2, and P3. In total we encountered four broken wires over the full running period. Towards the end of the last run chamber P4 occasionally showed persistent currents at the level of 2 μA, which required reducing the high voltage for a few minutes, to make the effect disappear.

4.3. Track reconstruction

The reconstruction of charged tracks in the spectrometer takes advantage of the fact that a combination of scintillator and calorimeter information already limits the area where tracks can be expected in the MWPCs. The reconstruction of electromagnetic or hadronic clusters in the calorimeter (see Section 5.3) in coincidence with a nearby A counter in front of it defines a window in which corresponding hits are kinematically allowed in each MWPC. The size of the window was tuned on data K_{Dal} and K_τ events taken at a very low beam intensity. The track reconstruction combines raw wire hits inside this window to space points, and then space points from the four chambers to a track, for which then the momentum can be determined. Since the typical occupancy of a single wire plane is about 10 hits per event, a loop over all hits allows too many combinations and requires a large amount of computer time.

4.3.1. Reconstruction of space points and tracks

The relation between the horizontal and vertical coordinates x and y and those measured along the inclined planes v and u is given by

$$\begin{pmatrix} v \\ u \end{pmatrix} = \begin{pmatrix} \cos\theta & \sin\theta \\ \cos\theta & -\sin\theta \end{pmatrix} \begin{pmatrix} x \\ y \end{pmatrix}, \quad \theta = 19.5^\circ. \tag{4}$$

For a true space point with coordinates x_0, y_0 associated with a straight track passing through the chamber, the distance to the four wire coordinates x, y, u, v should be minimal. To find a quadruplet one therefore minimizes

$$\chi^2 = \frac{1}{\sigma^2}[(x - x_0)^2 + (v - x_0\cos\theta - y_0\sin\theta)^2 + (u - x_0\cos\theta + y_0\sin\theta)^2 + (y - y_0)^2] \tag{5}$$

with $\sigma = 2/\sqrt{12}$ mm, which yields

$$x_0 = \frac{x + (v + u)\cos\theta}{1 + 2\cos^2\theta}, \quad y_0 = \frac{y + (v - u)\sin\theta}{1 + 2\sin^2\theta}. \tag{6}$$

Only combinations of clusters with a χ^2 less than an experimentally determined cutoff value p_{cut} were accepted. The finite distances between the planes also contribute to the χ^2 when the track angle is unknown. In the first analysis pass, a loose cut of $p_{cut} = 30$ was chosen. Once a track has been found, and the angle at which the track crosses a chamber was known, the space point procedure could be repeated, using the measured angle to project all wire coordinates to the same plane. p_{cut} was then reduced to 14, and tracks which no longer show three space points were discarded. The space-point-finding algorithm looped over all clusters until all possible quadruplets were found. To account for inefficiencies it then continued to find triplets in a similar fashion, i.e. points where the wires of only three planes overlap. Doublet space points were only considered after the track finding and momentum fitting phase for those tracks which have only three space points. The search could then be limited to a sufficiently narrow (1 cm^2) region, and after a doublet was found the momentum fit was repeated. Table 2 lists typical efficiencies per plane, for finding space points and tracks.

With a single plane resolution $\sigma = s/\sqrt{12} = 0.58$ mm ($s = 2$ mm) Eq. (6) yields spatial resolutions $\sigma_x = 0.35$ mm and $\sigma_y = 0.52$ mm. Fig. 16 shows the distribution of residuals in x, i.e. $\Delta x = x - (u+v)/(2\cos\theta)$, for which we expect a width of $\sigma\sqrt{1 + 0.5\cos^{-2}\theta} = 0.72$ mm.

Since tracks are straight lines outside the spectrometer magnet and bend primarily in the x-direction, one can use the differences in the x- and y-position at the center of the magnet projected from the upstream and the downstream part $(\Delta x, \Delta y)$, and the difference in the slope in y $(\Delta\alpha_y)$ between the two parts as criteria to associate space points to a track. The appropriate quality estimator is defined as

$$\chi^2 = \sum_{i,j} p_i E_{ij} p_j$$

$$(p_1 \equiv \Delta x, p_2 \equiv \Delta y, p_3 \equiv \Delta\alpha_y) \qquad (7)$$

where the inverse of the covariance matrix E_{ij} takes into account the measurement errors and the correlation between $\Delta\alpha_y$ and Δy.

The alignment of the chambers was determined from the survey of the fiducial marks on the outside frames and checked with beam halo muons, providing straight tracks, if all magnets are turned off. The wire offsets were accurately determined to within a fraction of the wire spacing and the (x, y) rotation to within 0.1 mrad [33]. Since halo muons illuminate only a restricted region of the chambers, the alignment procedure was cross-checked during normal running with pions from K_τ events.

Monte Carlo studies showed that knowing the particle position in the calorimeter limits strongly the range of possible hits in the proportional chambers. The track finding algorithm made use of this information and searched only in those windows permitted by the corresponding calorimeter clump, but then loops through all space point combinations consistent with the track hypothesis defined by the χ^2 cut. The latter was optimized using tracks recorded at low beam

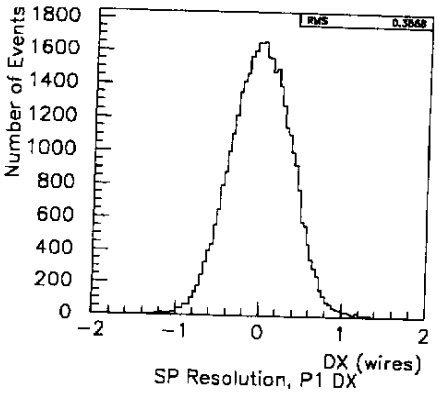

Fig. 16. Difference between x wire position and calculated x coordinate from u and v wires, in units of the wire spacing (2 mm). The peak has a width of 0.8 mm.

Table 2
Chamber and reconstruction efficiencies determined for a typical run near the end of the experiment

Chamber	P1	P2	P3	P4
Average efficiency per plane	0.987	0.990	0.889	0.854
Space point efficiency	0.999	0.999	0.937	0.896
Track efficiency (four space points)				0.838
Track efficiency (three space points)				0.993

intensity. More than one track could be assigned to each calorimeter clump and a space point could also be in more than one track. After all tracks with space points in all four chambers were found, the algorithm continued to search for tracks with one missing chamber. The track hypothesis for three-chamber tracks was tested by calculating a χ^2 based on the difference of the y-position of the space point in the middle chamber to the y-position obtained by interpolating the space points in the first and in the last chamber. Within the windows projected from the calorimeter clump on average about five space points were found, which also led to several possible track combinations. Eventually only one track for each calorimeter clump was selected, based on momentum and vertex fitting discussed below.

4.3.2. Track momentum determination

The algorithm used to find the particle momentum was based on a fit of the individual wire clusters which were combined to form a track. Five parameters x, Θ_x, y, Θ_y and R are needed to describe a track fully. The positions x and y and the slopes Θ_x and Θ_y are taken at MWPC P1 and R is the radius of curvature of the track which carries a sign to indicate the bend direction. If $\bar{W}_i$ denotes the measured clusters, g_{ij} the covariance matrix (taking into account the wire resolution and multiple scattering), α_k the five track parameters and $W_i(\alpha_k)$ the wire coordinates as a function of the parameters, the function to be minimized is

$$\chi^2 = \sum_{i=1}^{N} \sum_{j=1}^{N} (W_i(\alpha_k) - \bar{W}_i) g_{ij} (W_j(\alpha_k) - \bar{W}_j) \quad (8)$$

where the sum runs over all the wires associated with the track. Since the initial estimates for the parameters are quite accurate, the standard linearized, recursive minimization procedure using a first-order Taylor expansion of $W_i(\alpha_k)$ around the first value α_{k0} suffices. Finding the wire positions for the first estimate and the first derivatives with respect to all parameters requires calculating six trial tracks with slightly different initial values for each prospective track. Because there are large number of candidate tracks at this stage, this algorithm is the most computer time consuming part of the whole analysis chain, even though the minimization procedure converges rapidly. To reduce the computer time, a few simplifications are available. The step size of the transportation of the track through the magnetic field can be lengthened from the nominal 5 to 20 cm, or the magnetic field can be simplified by a hard edge approximation. In addition, the covariance matrix can be reduced to a diagonal matrix if multiple scattering is ignored. Large-angle scattering at a given point introduces correlated deviations at all points downstream [33].

Even after including multiple scattering the measured χ^2 distribution is broader than expected from the Monte Carlo simulation. We ascribe this effect to shortcomings of the alignment, the imperfect knowledge of the field map and to smearing of the spatial resolution per plane due to spurious hits. Scaling the wire resolution by a factor 1.4 and adding accidential tracks brings the two distributions into agreement (see Fig. 17).

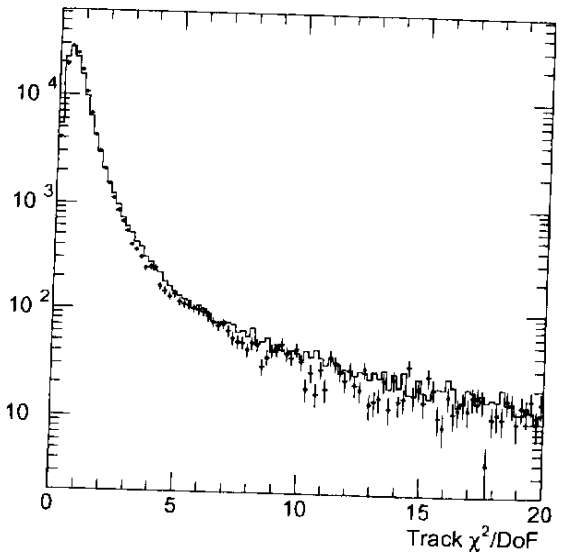

Fig. 17. Left: Measured track χ^2 per degree of freedom (histogram) for K_τ events compared to the Monte Carlo simulation (points with error bars) using the measured field and space point resolution (scaled by 1.4) and adding accidential tracks which account for the high χ^2 tail.

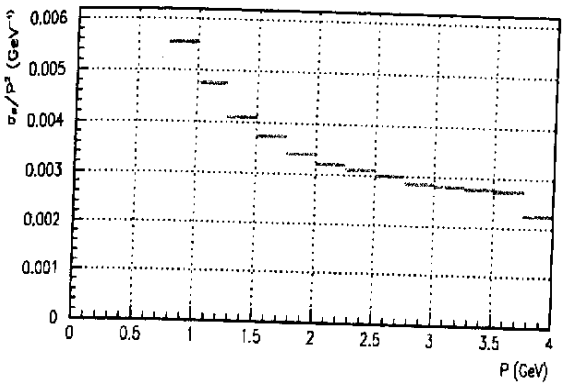

Fig. 18. Charged particle spectrometer momentum resolution.

The momentum resolution as function of momentum is displayed in Fig. 18. The field used provides a transverse momentum kick of 255 MeV/c. For high momenta, where multiple scattering is unimportant one expects σ_p/p^2 to approach a constant value C in units $(\mathrm{GeV}/c)^{-1}$. For four point tracks we find $C = 0.3\%$. For three-point tracks the resolution degrades to $C = 0.7\%$ if P4 information is missing, and to $C = 0.6\%$ if P3 information is missing, while missing P1 and P2 information has little influence on the resolution.

4.3.3. *Vertex fits*

An important distinguishing feature of the K^+ decays of interest in this experiment is a common vertex of the tracks of the three decay products. The ability to find this vertex is crucial for separating true decays from accidental backgrounds. For most of the analyses in this experiment, only events with three charged tracks from K^+ decays are of interest. Therefore, three or more in-time calorimeter clumps are required. Each clump can have a list of candidate tracks. The vertex-fitting procedure searches for the combination of three tracks, each associated with a different calorimeter clump, that gives the best vertex quality. If a clump is not in the vertex, and has multiple tracks associated with it, only the track with the best χ^2 is kept. All other tracks are discarded.

Two vertex-finding algorithms have been used. The first one minimizes S, which is the square root of the quadratic sum of the closest approach of the tracks $(x(z), y(z))$ to a common vertex point, using the individual fitted track parameters, but not including information on the quality of the fit. The combination of three tracks having the lowest value of S is assumed to have the highest probability to originate from a K^+-decay. For K_τ events Fig. 19 shows the distribution of this quantity. Also shown is the typical S distribution of accidental events, selected according to the time spread between the tracks. The second method, which improves the resolution slightly, involves a constrained fit to the vertex including the error matrix of the track. The quality of the vertex fit depends however upon how far upstream the decay took place. The uncertainty in the position of the vertex increases linearly with the distance from the first chamber. For the quality estimator a renormalized value of S is therefore used, which is corrected for the z dependence.

If all decay products are charged the reconstructed K^+ can be propagated back through the beam line to the production target (see Section 2). As an example Fig. 20 shows the x position at the production target versus the K^+ momentum again for identified K_τ events. This is a very useful tool to reject accidential three-track combinations or those decays with missing particles in analyses of very rare decay, in particular the search for $K^+ \to \pi^+\mu^+e^-$.

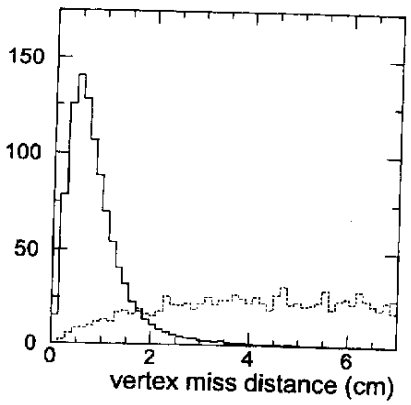

Fig. 19. Distance of closest approach S of three-pion tracks for a sample of K_τ events (solid histogram) and that of accidental three-track events.

4.4. Performance

Figs. 21 and 22 show invariant mass distributions for three different decay channels. Our most important reference sample is the K_τ, exhibiting a three-pion mass resolution of $\sigma_M = 2.2$ MeV/c^2 ($\sigma_M/m_K = 4.4 \times 10^{-3}$). For the rare decay $K^+ \to \pi^+e^+e^-$ the three-particle mass resolution is $\sigma_M = 4.8$ MeV/c^2. The mass resolution is worse here, because the available phase space is larger. The event selection is described in Refs. [34,11].

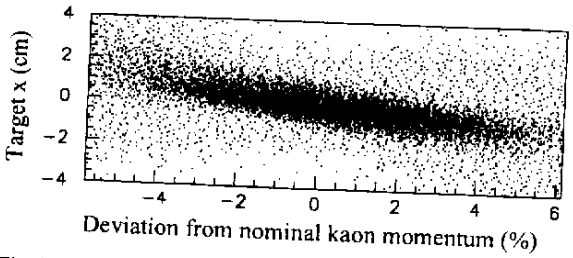

Fig. 20. The horizontal position of the reconstructed K^+ at the production target, after trace back through the beam line, for a sample of identified K_τ events as a function of the deviation from the nominal momentum.

The four-particle invariant mass spectrum from the decay $\pi^0 \to e^+e^-e^+e^-$ (branching ratio 3.14×10^{-5}) exhibits a resolution of $\sigma = 5.8$ MeV/c^2.

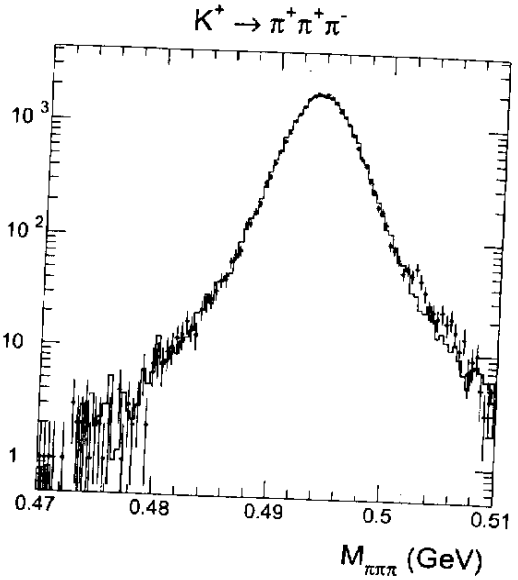

Fig. 21. Three-pion mass spectrum for K_τ decay. The histogram corresponds to the Monte Carlo simulation of the spectrometer, the points with error bars to the data.

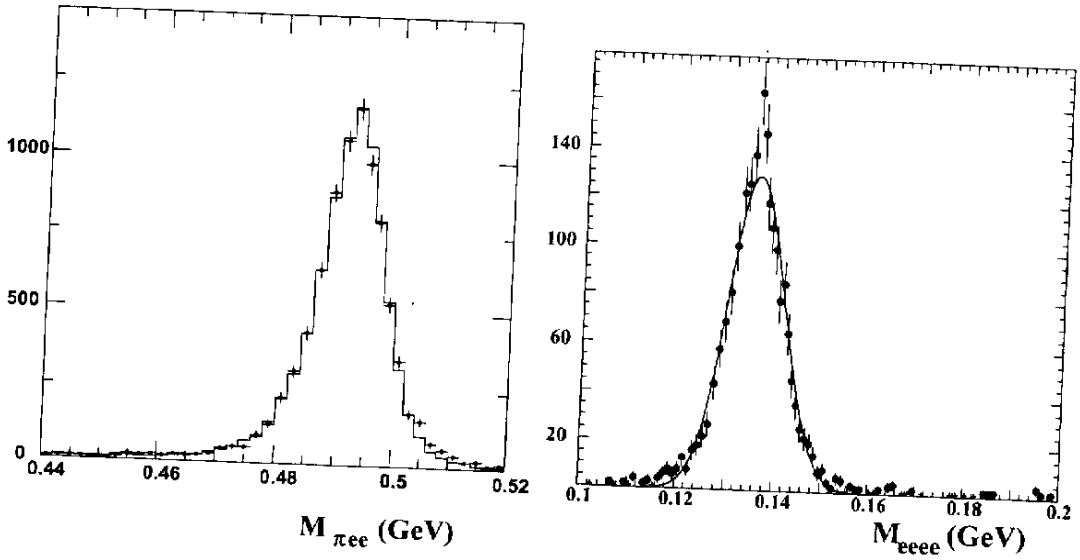

Fig. 22. Left: three-particle invariant mass spectrum for $K^- \to \pi^+e^+e^-$ decay; right: four-particle invariant mass spectrum for the decay $\pi^0 \to e^+e^-e^+e^-$. The histograms correspond to the Monte Carlo simulation of the spectrometer, the points with error bars to the data.

5. Electromagnetic calorimeter

5.1. Construction details

The electromagnetic calorimeter is a modular array of the Shashlyk type [17]. Each module consists of alternating lead and scintillator plates, with the light collected by wavelength-shifting fibers. The calorimeter contains 30 modules in the horizontal and 20 modules in the vertical direction, covering the acceptance of the proportional wire chambers. 6×3 modules were omitted in the center of the calorimeter to allow the beam to pass through. This is shown in Fig. 23.

As the design of a module is described elsewhere [17] in great detail, only the most important points are discussed here. Fig. 24 shows a single module consisting of perforated lead plates alternating with plastic scintillator plates 1.4 ± 0.005 and 4.0 ± 0.05 mm thick, respectively. Altogether, there were 60 layers with a total thickness of 15 radiation lengths. The transverse dimensions are 11.4×11.4 cm^2, corresponding to 2.5 Molière radii. The light is collected by 144 wavelength-shifting fibers (WLS), with a diameter of 1.2 mm, inserted through the holes in the scintillator and lead plates. The selected number of fibers resulted in capture of the scintillation light at any emission angle. To reduce the contribution of the longitudinal fluctuation of shower development to the energy resolution, each fiber was viewed by photomultiplier tubes at both ends. This was

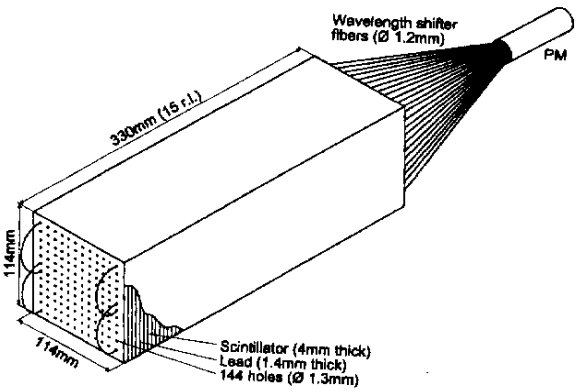

Fig. 24. Calorimeter module.

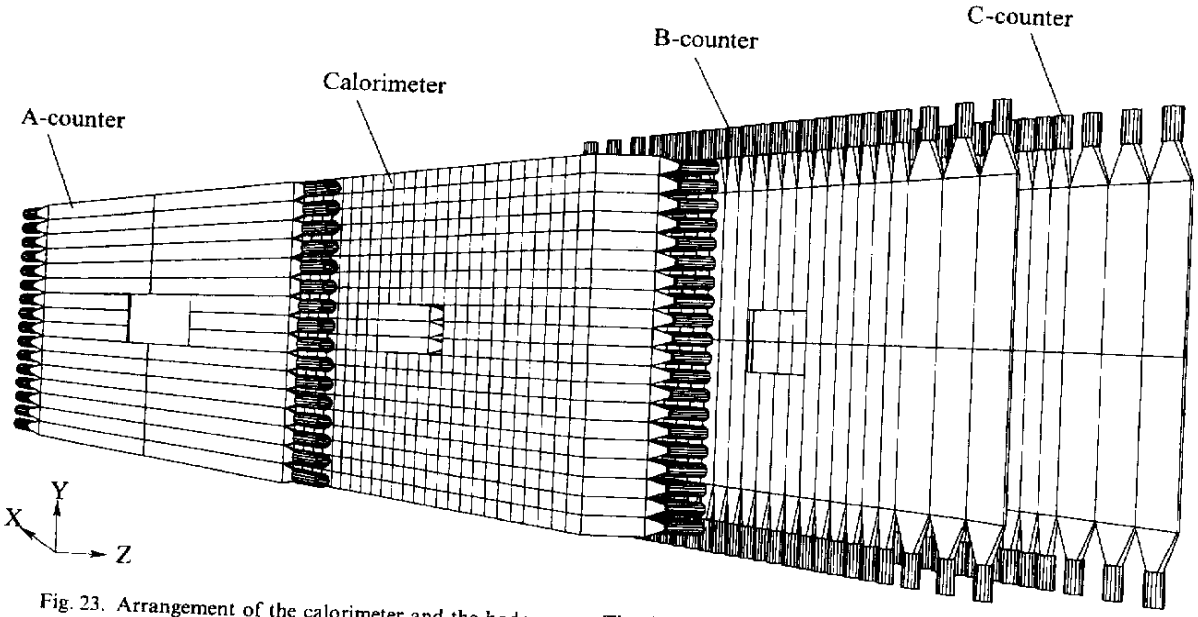

Fig. 23. Arrangement of the calorimeter and the hodoscopes. The A counter was moved 1.5 m upstream in this drawing.

Table 3
Calorimeter parameters

Number of modules	582
Lateral size	11.4×11.4 cm^2
Number of planes	60
Scintillator/lead	4.0 ± 0.05 mm/1.4 ± 0.005 mm
Thickness	$15X_0$
Radiation length	21.6 mm
Molière radius	45 mm
Attenuation length in scintillator	30 cm
Scintillator	Polystyrene & P-terphenyl & POPOP
WLS-fibers	Polystyrene (core), PMMA (cladding) 1.2 mm diameter
Number of fibers per module	144
Interfiber distance	9.6 mm
Attenuation length in fibers	1.2 m
PM-tube	FEU-85 & FEU-115
Contact between fiber and PMT	Direct contact, no optical grease used

accomplished by making a loop with a radius of 3 cm at the front of the module (Fig. 24). White paper used as reflecting surface was placed between the lead and scintillator plates. The whole module was wrapped with aluminized mylar and tied together with four 50 μm thick steel strips on each side to provide rigidity. Table 3 lists the most important parameters.

To improve the behavior of the selected photomultiplier tubes under high intensity conditions, a preamplifier with a gain of ~ 50 was attached to the PMT anode chain. At the output of the preamplifier the signal was split for the ADC and TDC channels. The TDC signal passed a low threshold discriminator (LTD) where it was shaped into a 20 ns wide ECL signal. Each LTD module contains 16 channels. The threshold in each channel may be individually adjusted in the range 1–30 mV via a CAMAC controller. The logical OR of all 16 channels has been used to generate the cosmic-ray trigger.

5.2. Calibration

The calorimeter response was originally measured in an electron beam [17]. Since a Shashlyk calorimeter as opposed to a lead–glass calorimeter is sensitive to traversing muons, we monitored the response during the experiment and maintained the calibration using cosmic-ray muons as well as electrons and positrons from the decay $\pi^0 \to e^+e^-\gamma$. This method has advantages over the standard method used to calibrate a highly granular electromagnetic calorimeter with an electron beam. It needs no beam, requires no vertical and horizontal movement of the calorimeter nor special monitoring systems like LEDs or lasers, and takes less time. Furthermore the calorimeter is exposed approximately uniformly and the mean values of the signals from each module are expected to be the same which makes this method a very effective tool, especially for low energies (≈ 1 GeV). For the cosmic-ray calibration, a calorimeter self-trigger was used. The trigger required hits in at least at six rows on the left or right side of the calorimeter (Fig. 25). For the actual calibration of each module, cosmic-ray muons entering through the upper surface of the module and exiting through the lower one were selected by requiring signals in the adjacent modules above and below and no signals in the left and right neighbors. The spectrum of these

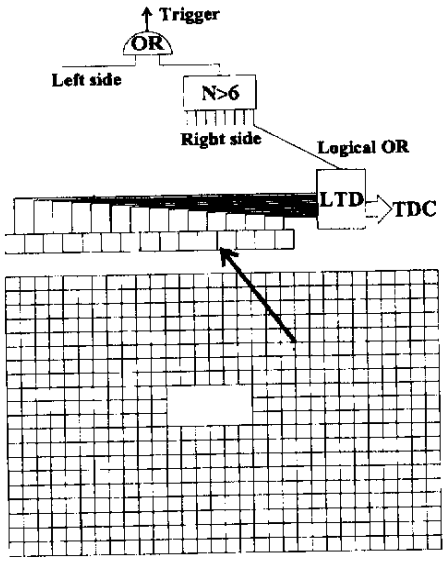

Fig. 25. Cosmic-ray muon trigger.

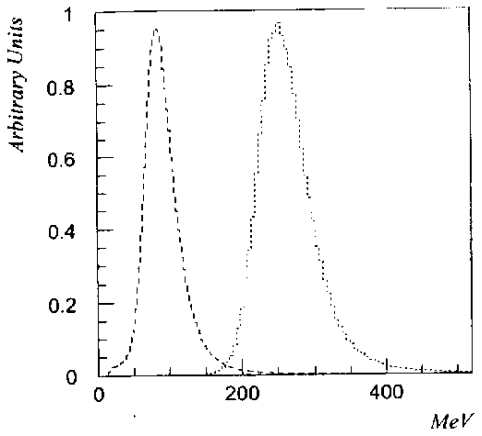

Fig. 26. Comparison of the calorimeter response to cosmic-ray (dashed) and beam muons (dotted) after high voltage corrections and averaged over the whole detector. The ratio of the mean amplitude for each counter is constant with a standard deviation of 1.9%.

signals, after high voltage adjustment, averaged over the whole calorimeter is displayed in Fig. 26 and compared there to signals due to beam muons which penetrate the module longitudinally. For the relative calibration the mean signal amplitude for each module was calculated. The ratio of the mean amplitudes for beam and cosmic-ray muons was the same for all modules to an accuracy of $\sigma = 1.9\%$.

Fig. 27 shows the measured momentum spectrum of the electrons and positrons which were used for the calibration. They were identified using Cherenkov counters and taken from data accepted in a regular run. The E/p ratio (ratio of the energy deposited in the calorimeter to the momentum measured in the spectrometer) averaged over all momenta after calibration is shown in Fig. 27. The distribution of the ratio of the calibration coefficients, from the cosmic-ray and electron calibrations is constant to an accuracy of $\sigma \sim 4\%$. The stability of the calibration coefficients can be monitored with the cosmic-ray precalibration with an accuracy of $\sim 1\%$.

During data taking, the zero suppression, i.e. the elimination of signals from calorimeter modules with no hits, is turned off by the data acquisition system for one in every 200 spills in order to determine the ADC pedestals. Cosmic-ray events, taken between AGS spills, provided an additional method of determining the pedestals of the calorimeter. This was done on a run by run basis.

The timing calibration uses two simultaneous hits in the calorimeter, taking raw data events from regular runs. No event reconstruction or selection was necessary. The calibrated time was calculated as

$$t_i = \tilde{t}_i - \tau_i - \alpha_i f(a_i) \tag{9}$$

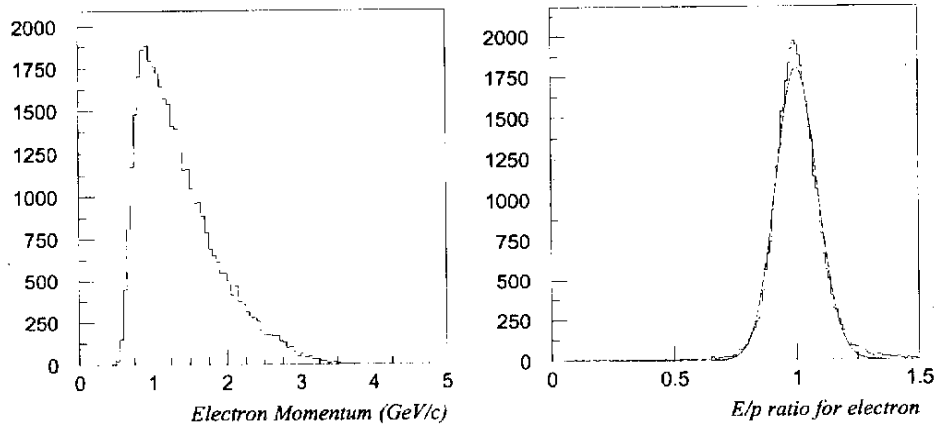

Fig. 27. Electron calibration. Left: electron spectrum from K_{Dal} decays; right: ratio of the measured energy after high voltage correction and averaged over the whole detector to the momentum measured in the spectrometer. The smooth curve is a Gaussian fit to the data with $\sigma = 0.085$.

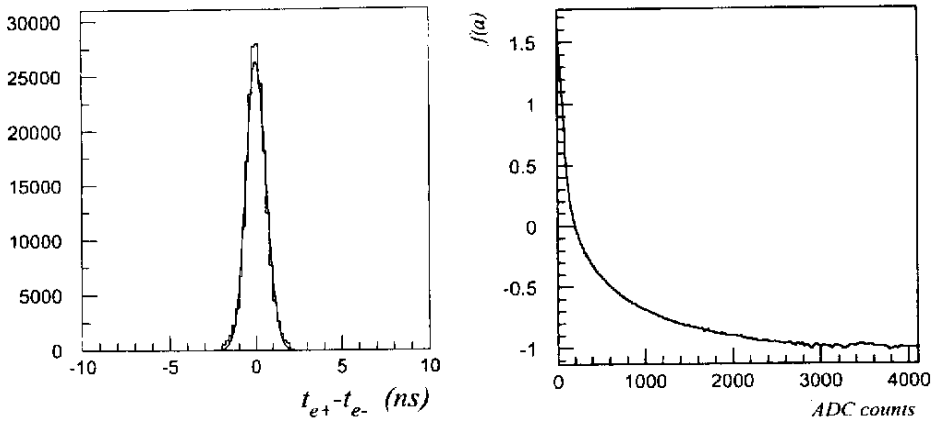

Fig. 28. Timing calibration. Left: time difference spectrum for electrons and positrons from K_{Dal} decays; the smooth curve is a Gaussian fit to the data with $\sigma = 0.56$ ns. Right: slewing correction function (see text for details).

where i the module number, $\tilde{t}_i$ is the raw TDC time, τ_i the TDC offset, and $\alpha_i f(a_i)$ the slewing correction. $f(a_i)$ is a function of the amplitude a_i (in ADC counts) only and was taken to be the same for all modules (Fig. 28).

5.3. Reconstruction of electromagnetic clusters

The reconstruction of electron, positron and photon clusters was based on the Monte Carlo simulation of the electromagnetic shower (1 GeV region): (i) 99% of the deposited energy is located in a 3×3 array of modules; (ii) 95% of the deposited energy is located in a 2×2 array of modules; (iii) the longitudinal leakage of energy is small. The characteristic signature of minimum ionizing particles (muons) is usually a single module hit with a deposited energy corresponding to a 260 MeV electromagnetic shower (Fig. 26).

In approximately 50% of all cases a pion behaves in the calorimeter like a minimum ionizing particle. Hadronic shower development is characterized by significant longitudinal leakage and a wider transverse distribution. Such a cluster may be recognized as a single or several overlapping and/or isolated electromagnetic clusters. The total deposited energy is usually less than the pion momentum (see Fig. 29).

To determine the transverse coordinate of a particle, the center of gravity of the clump was calculated and then corrected using a specially designed function. The time assigned to the clump was defined as a weighted average of times in modules with weights dependent on energy deposited in each module. For charged particles the momentum is known from the magnetic spectrometer. This allowed us to investigate the spatial response of the calorimeter and its linearity. Fig. 29 indicates a small non-uniformity of light collection and that the calorimeter showed a small non-linearity which could be fit with the expression

$$\frac{E}{p} = 1 + a + bp + cp^2 \tag{10}$$

with $a = (0.51 \pm 0.04)\%$, $b = (0.59 \pm 0.04)\%$ $(\mathrm{GeV}/c)^{-1}$, $c = (-0.41 \pm 0.01)\%$ $(\mathrm{GeV}/c)^{-2}$.

5.4. Performance

Fig. 30 shows the energy resolution of the calorimeter as a function of the energy. The resolution deduced from K_{Dal} data can be described by the formula

$$\sigma_E/E = \left(a^2 + \frac{b^2}{E}\right)^{1/2} \tag{11}$$

with $a = (3.57 \pm 0.20)\%$, $b = (7.58 \pm 0.15)\%$ $\mathrm{GeV}^{1/2}$.

The large constant term, a, is most likely due to the non-uniformity of light collection

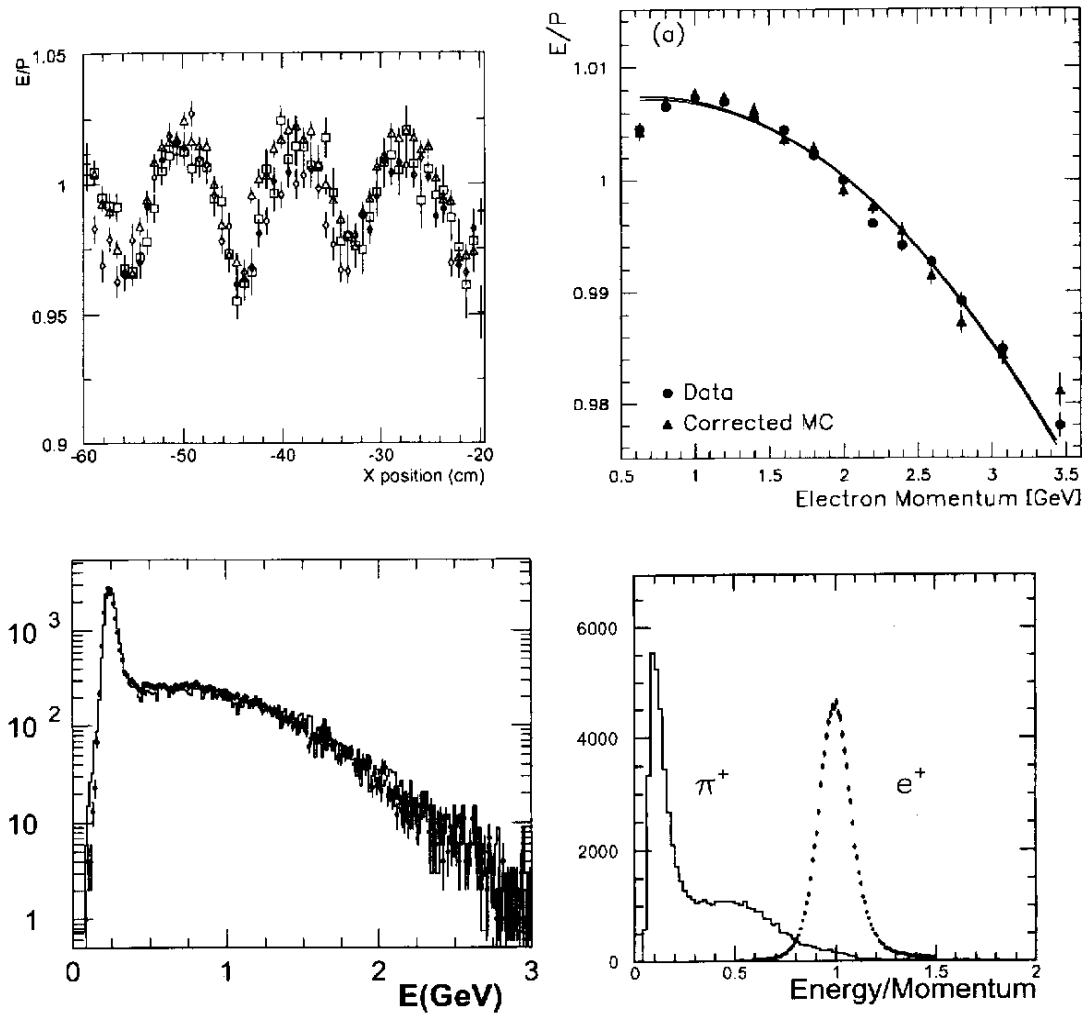

Fig. 29. Various distributions illustrating the response of the calorimeter. Top left: measured energy to momentum ratio for electrons as a function of the horizontal position indicating the influence of the non-uniform light collection in the calorimeter modules (the different symbols refer to different vertical rows). Top right: non-linearity correction. Bottom left: measured calorimeter response (data points) for pions from K_τ decays compared to the Monte Carlo simulation (histogram). Bottom right: energy to momentum ratio for positrons and positive pions from K_{Dal} decays averaged over all momenta.

and gain variation from channel to channel. Fig. 29 shows the deposited energy in the calorimeter divided by the momentum of the track (E/P) for pions and positrons. For the chosen rejection algorithm which satisfies the requirement of the experiment, typically 6.4% (1.9%) of the pions with an energy of 1.5 GeV (3 GeV) survive a cut $E/p > 0.9$ as compared to 86% (80%) of the electrons of the same energy.

The time resolution of the calorimeter was measured to be $\sigma_t = 0.35$ ns for electrons (~ 1 GeV) and about $\sigma_t = 0.79$ ns for muons. This resolution was measured for real events in full

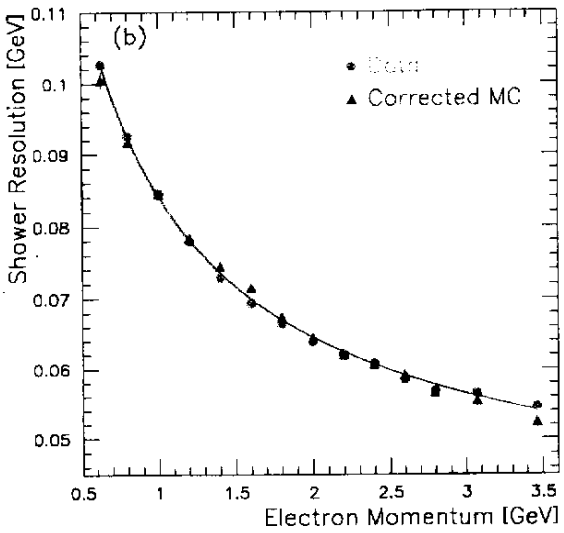

Fig. 30. Electron energy resolution σ_E/E of the calorimeter as a function of the energy.

intensity running after correcting for particle time of flight in the apparatus.

6. Particle identification

6.1. Gas Cherenkov counters

6.1.1. Introduction

The (sometimes conflicting) design goals for the Cherenkov counters (C1 and C2) were

- high electron efficiency; but, in each counter, less than 0.2% probability to misidentify a π^- as an electron (further rejection in the calorimeter then yields an overall false π^- signal probability of less than 3×10^{-6});
- high e^+ efficiency (at least 98%), to avoid misidentification of an e^+ from one of the many sources of e^+e^- pairs as π^+ or μ^+; but insensitivity to pions and muons from kaon decays to three charged particles, which range up to ≈ 3.4 GeV/c;
- minimization of correlated false signals or loss of signal, e.g. from interactions or δ-ray production, or particles in regions of poor acceptance;
- relatively short length along beam line to achieve high acceptance for three charged-particle final states; and
- stable operation in an intense beam with instantaneous rates up to 5 MHz in individual photomultipliers.

Figs. 31 and 32 show elevation sections of the two Cherenkov counters (C1 and C2) which were developed in response to these criteria. The thickness of each counter is about 0.12 g/cm^2, excluding the Cherenkov radiating gas (0.01 g/cm^2 H_2, 0.08 g/cm^2 CH_4). The mirrors contribute about 35 mg/cm^2, or about 0.2% X_0 per mirror. The primary beam and its energetic

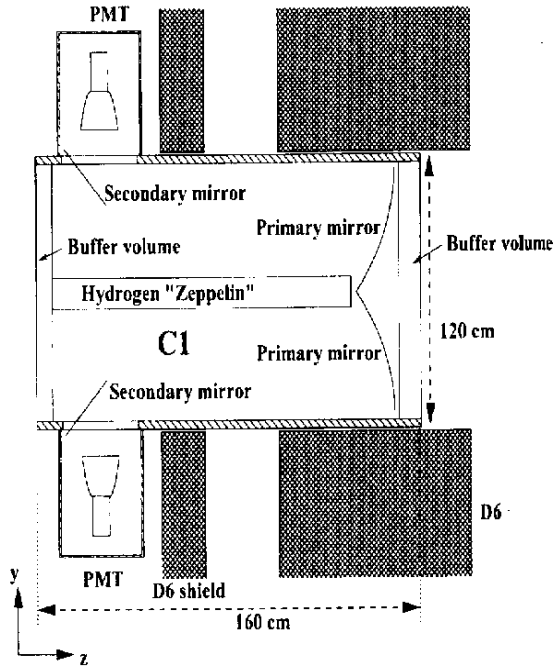

Fig. 31. Elevation section of the right side of Cherenkov counter C1 showing the shell, optical elements and the enclosure of the beam path (Zeppelin). The left side mirrors the right side except for the beam tube. In this view each PMT shadows an unseen PMT, so that only 2 of the 4 PMTs on each side are visible. D6 and D6 shield refer to the pole and magnetic shield of the spectrometer magnet.

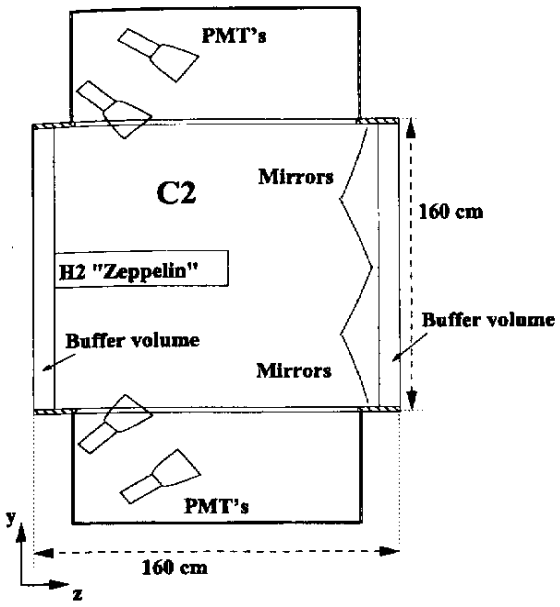

Fig. 32. Elevation drawing of the Cherenkov counter C2 showing the shell, optical elements and the beam tube (Zeppelin). In this view, the PMTs furthest vertically from the beam each shadow one PMT behind it in the figure, and the PMTs closest vertically to the beam each shadow three PMTs behind them for a total of six PMTs in each quadrant, or 24 in C2.

decay products pass through the right cell of each counter. Beam interactions and light from Cherenkov radiation and δ-rays are reduced by a closed beam tube in each cell, filled with hydrogen and suspended in the region traversed by the beam (labelled "Zeppelin" in Figs. 31 and 32). Mirrors are absent from the area through which the beam particles pass. The left sides are mirror images of the right sides except for the missing mirrors and the beam tubes. Some photomultipliers are shadowed behind those visible in the figures. There are 8 photomultipliers in C1 and 24 in C2.

The most relevant points of the conceptual design, with an indication of the problems addressed, and those which remained, are summarized below.

The first bending magnet in the apparatus (D5) separates positively and negatively charged particles. Separation of the right and left sides of C1 and C2 by a septum allows the use of gases with different Cherenkov thresholds on different sides:

- Hydrogen at STP on the left side has a threshold γ_{th} of 53–55 (varying over our temperature range of 5–35°C), at wavelength of 200 nm, near the lower end of our wavelength sensitivity. The threshold momenta are thus about 7.6 GeV/c for pions, and 5.7 GeV/c for muons, well above the charged particle momenta from three-body K^+ decay products; however the light yield, even for the highly relativistic e^-, is rather low, leading to e^- efficiencies of only ≈90%.
- Use of a gas with higher index of refraction such as CH_4 on the right gives more light and higher efficiency for positrons, but the lower thresholds (about 3.4 GeV/c for muons) allowed substantial intensity-dependent background light from beam decay muons.

δ-ray production in C1 was reduced by the very thin mirrors, but with some degradation in optical quality. The placement of C1 in the D6 magnet suppressed backgrounds from δ-rays produced upstream, but this position also made δ-ray production in the C1 mirrors especially troublesome in pattern recognition and led to a spread in photon direction due to the bend of the radiating particle in the magnet. A special challenge in C2 was accepting the large phase space occupied by the low momentum positrons from $K^+ \to \pi^+\pi^0$ followed by $\pi^0 \to e^+e^-\gamma$, K_{Dal} decays. Suppression of scintillation (from either beam particles or particles of interest) required tight gas systems to reduce O_2 contamination, in both counters.

6.1.2. Operating history

The counters were operational from February, 1995 through December, 1998. CO_2 was used on the right in 1995, but CH_4 was used in later years, because of its lower scintillation (about 2/3 that of CO_2) and density. Before the 1997 run, some mirrors (in C1L) and other optical elements in C1 were replaced, and all photomultipliers were coated with wavelength shifters [35]; the wavelength shifter coating increased light yields by about 40%.

Initially, light from beam decay muons or other uncorrelated tracks led to intensity-dependent electronics losses on the right of 1–5%. Electronics upgrades in 1997 and 1998 reduced these losses. The overall efficiency on the right (in CH_4) in 1998 was approximately 98–99% in both counters. Efficiency on the left (in H_2) in 1998 was $\approx$89% in C1L and $\approx$92% in C2L.

6.1.3. Optics design

6.1.3.1. General remarks on the optical design. - Liouville's theorem for photons in optical systems [36] shows that the quantity $(\Delta x\,\Delta y) \times (\Delta \sin\theta_x\,\Delta \sin\theta_y)$ is conserved, indicating that the area $\Delta x\,\Delta y$ on which the rays fall can be reduced, but with an increase in angular spread. Cherenkov photons from $K^+ \to \pi^+\pi^0$ with subsequent $\pi^0 \to \gamma ee$ decays are the most common and have the largest initial phase space of processes of interest to us. Therefore photons from the simulation of this process were used in the design of C1 and C2 and later to test their efficiencies. Their phase space is shown in Fig. 33.

The phase space occupied by the rays striking the surface of the mirror in C1 is $\approx$100 cm^2 sr, with the x and y phase space substantially independent. Since the usable area of a 12.7 cm diameter photomultiplier is about 110 cm^2, and 2π sr can be subtended at the exit aperture of a standard Winston cone, only a modest number of photomultipliers is required, if appropriate collectors can transform the phase space to small spatial extent and a slope distribution azimuthally symmetric about the photomultiplier axis [37,38]. Losses due to small gaps in the optics [39] must of course be addressed in a real design.

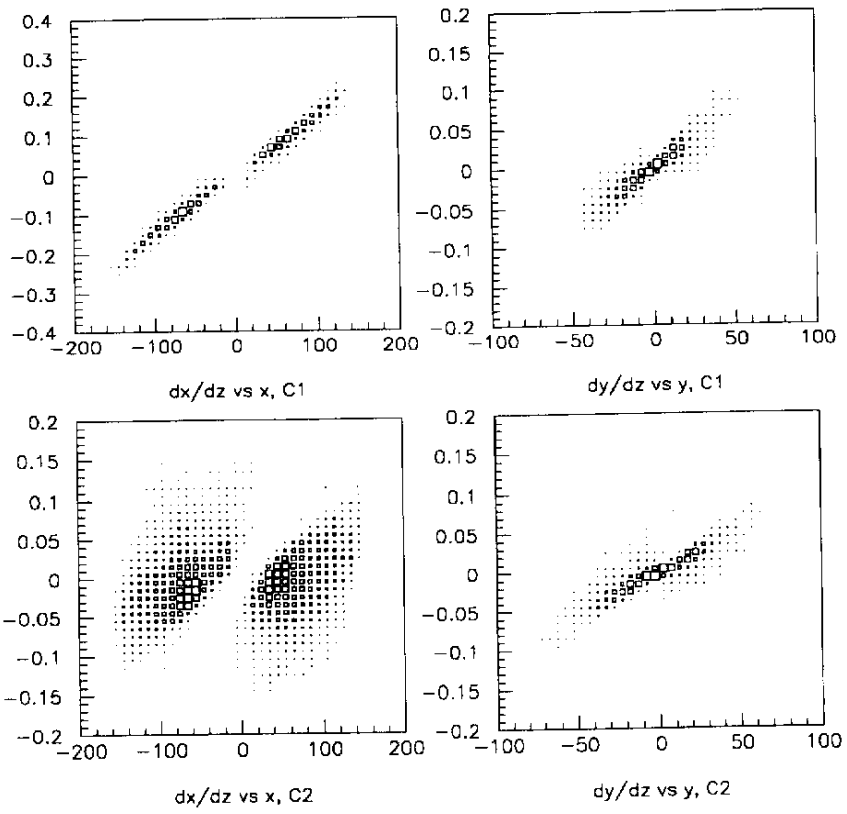

Fig. 33. Optical phase space for photons from simulated low-mass pairs in $K^+ \to \pi^+\pi^0$ with subsequent $\pi^0 \to \gamma ee$ decays, at the C1 and C2 primary mirror planes.

6.1.3.2. Innovative aspects and associated problems. The goal of accommodating the large photon phase space with good efficiency and minimum material posed two challenges:

- fabrication and support of thin mirrors and;
- design of customized optics to deliver the large photon phase space to a few photomultipliers (to minimize both cracks in acceptance, and cost of the detector).

In this section we summarize new or unusual elements in our design decisions and implementation.

Primary mirrors (after study of several alternatives [40–43]) were assembled from individual mirror elements (slats) which could be independently shaped and oriented. The method potentially allows fabrication of an overall complicated optical shape. In addition, the composite nature of the optics (similar to a Fresnel lens) allowed reorientation of mirror elements rather than overall curvature of the mirror arrays, thus giving longer path length for the radiation of Cherenkov photons.

Each slat was made of a lightweight aluminized surface attached after aluminization to a stiff lightweight frame of curved polyimide foam.[30] The mirror substrate chosen was 0.51 mm acrylic (original construction) or 0.51 mm polycarbonate (replacement construction) in C1 and 0.81 mm acrylic in C2. Attachment by (only one) spot of glue and several flexible polyurethane bands held the mirror surfaces to the shape of the slats, and avoided problems due to differential expansion of the two materials. The slats were oriented roughly vertically, with the primary curvature along the vertical direction, and the horizontal curvature of the array obtained by orientation of the individual slats. The slats were overlapped in a "venetian blind" style to provide continuous coverage for photons travelling away from the beam axis. This method allowed the construction and customized configuration of large reflecting surfaces in non-spherical forms, and removed the limits on mirror dimensions set by pressure vessels, ovens, and evaporators.

[30] Rohacell 51: Roehm GmbH, Darmstadt, Germany.

To minimize mass, the slat frames were made of three ribs, connected by a few cross-pieces. Light collection was improved by introducing a small secondary curvature in the short dimension of the mirror, to approximate more closely a continuous mirror array. Distortions are generally well controlled by additional cross pieces between the ribs, although distortions at the very ends, beyond the final point of mirror attachment, remained problematic for the very thin mirrors in C1, which were also less well supported than the mirrors in C2, because of concerns about delta ray production in the mirror framing material. In C1, distortions with humidity [44] were controlled by stiffening the mirror ends, at the cost of increasing the material at the edges to $\approx 0.3\%\ X_0$.

Construction of the mirrors from differential elements facilitated light weight construction, and further allowed:

- flexibility in choice of PMT and concentrator positions, to satisfy mechanical constraints or optimize magnetic shielding;
- quick modification of the optics or replacement of individual degraded elements; and
- tailoring of the shape (e.g. radius of curvature in the design, or the modifications described above, carried out in response to tip distortions) as a function of position to minimize bounces and maximize collection.

Because of the bending in the magnetic field, the horizontal and vertical phase space occupancies differ (see Fig. 33). To match these differences, the collectors are not simple Winston cones [37,45], but rather modified compound elliptical concentrators [36] with elliptical sides in the bending direction but simple flat planes in the non-bending direction. The sides come to a square at the PMT photocathode, of the same total area as the (circular) photocathode. Photons which fall in the collector corners are rescued by small mirror patches (ears) which match the collector exit aperture to the photomultiplier. Further details of the construction are given in Ref. [46].

6.1.3.3. C1 and C2 optics designs. The elements of each primary mirror array are oriented roughly vertically and point to a photomultiplier–collector

FERMILAB

combination (or two photomultipliers in some cases in C2) at the array center. In C1, an intermediate mirror array reflects the photons to allow the photomultipliers to be oriented vertically in a region of low magnetic field. In C2, more space is available for the PMTs and no intermediate mirrors are required. In both C1 and C2 the optics is symmetric (except for beam hole cutouts) under a left–right reflection. Photon collection is somewhat worse near the edges of the arrays, and substantially worse near the fiducial volume edge, particularly near the magnet surfaces, in part because of the loss of photons which go out of the fiducial volume. Fortunately there are also few particles near these kinematic boundaries, and the particles which populate these phase space regions are easily separated kinematically between K_{Dal} decay candidates and candidates for the rare decays of interest to us.

The phase space distributions for photons from simulated K_{Dal} events were used to test the C1 and C2 design and efficiencies are shown in Fig. 33. The larger phase space in C2 is due to large bending angles for low momentum electrons and positrons, and required doubling the collectors and photomultipliers for the high occupancy regions vertically close to the beam. This collector/photomultiplier doubling also has the advantage that low momentum electrons from K_{Dal} decays are relatively concentrated in the doubled partner. Another consequence of the large C2 phase space is that 0a few percent of photons travel toward the beam and those lying close to the edge of a mirror element may be subject to losses because the reflected ray is blocked by an adjacent mirror. These losses are again primarily in the phase space populated only by K_{Dal} events, and the additional kinematic separation available for these events makes these losses acceptable.

Although the intermediate reflectors in C1 introduce an extra bounce for all photons, they also simplify the design, simplify the magnetic shielding required, and give only about 0.75 bounces more than solutions without the intermediate reflector. From the computer results, the average number of bounces seen by photons from the K_{Dal} decay mode in C1 is approximately three (one each in primary and intermediate mirrors, and on average approximately one in the collector), and in C2 approximately two.

C1 has 14 slats 20 cm wide (horizontally) by 60 cm tall in each quadrant of primary mirrors. C2 has 24 slats 14 cm wide by 40 cm tall in each quadrant, arranged in 4 subarrays of 6 slats each. The C2 arrays near the beam vertically are oriented toward the beam line, with photons passing to collectors on the opposite side of the beam line, in order to give slightly more radiative path for those particles in that highly populated region. To avoid blocking optical paths, the mirror arrays away from the beam vertically are oriented away from the beam and direct photons to photomultipliers on the same side of the beam.

6.1.4. Optics tests and construction

6.1.4.1. Metallization and reflectivity. The surfaces were metallized by electron beam evaporation of aluminum of (80 nm thick) followed by an overcoat to protect against aluminum oxide formation.[31]

Reflectivity measurements were made at wavelengths from 628 nm down to about 185 nm, using two different He–Ne lasers and a D_2 arc excitation source with a system of wavelength filters. Measurements were made both on materials under consideration for use and on many of the final installed mirrors. Initially a 30 nm MgF_2 coating, with high reflectivity but vulnerable to degradation with humidity [47] was used. A more durable SiO_2 overcoating which was optimized in cooperation with industry[31] yielded reflectivities $\approx$75–80% in the range 225–270 nm, and was used on the optics installed in 1997.

A commercial aluminized mylar foil[32] was used for the flat sides of the collectors, at lower cost than the aluminized surfaces used for the other mirror elements. This foil showed a surprisingly high reflectivity throughout the visible and near UV. The measured reflectivity remained above 65% for wavelengths down to 190 nm.

6.1.4.2. Assembly into arrays, alignment and testing. The construction time of the individual slats

[31] P.A. Clausing Inc., Skokie, IL 60076-3438.

[32] Madico Inc., 45 Industrial Pkwy, Woburn, MA 01801-1919.

was small compared to assembly and alignment. The mirrors were constructed and assembled into subarrays. During this assembly the radii and orientation of the differential mirror elements were tested for relative alignment by scanning them with a laser beam [46]. To support and test the design, we developed optical ray-tracing code which could follow test rays through several standard optical elements: spheres, cylinders, arrays of cylindrical slats, planes, parabolas, ellipses, as well as the combination elliptical wall collectors, and any surface whose normal and spatial limits are specified. The code uses successive approximations for complex surfaces to find the point of intersection of the ray with any mirror surface. All elements of the optical design, except for the hand-crafted ears, were modelled by the ray-tracing code. Simulation results for the dependence of photon losses on deviations of the C1 mirror normal are shown in Fig. 34. In the simulation the mirror alignments were disturbed by displacing the mirror element axes. The percentage of photon losses is plotted versus the displacement of the axis at the center of curvature of the mirror. The deviation of the final collected ray at the photomultipliers is approximately twice the displacement of the mirror axis shown in the figure. During the alignments, the deviation of the return ray from expectations served as an indicator of the quality of the mirror alignments. The radii of the individual mirrors elements was about 250 cm, so that a 5 cm shift of the axis approximately corresponded to a 20 mrad misalignment of the mirrors. A 10–20 mrad misalignment (2–5 cm displacement of the mirror center, or 4–10 cm deviation of the collected ray) would cause significant inefficiency in y, but less in x. The rough criterion for optics acceptability was 2–4 cm deviation in y, and 4–6 cm in x.

For C1, bench tests (of about 1500 rays per assembled quadrant) at BNL before placement in the counter support the conclusion that distortions of the mirror normal up to 5 mrad in y and 10 mrad in x did not affect the efficiency substantially. For individual mirrors, oriented freely, only a few percent of 75 tested input rays per mirror element were beyond 5 mrad from nominal.

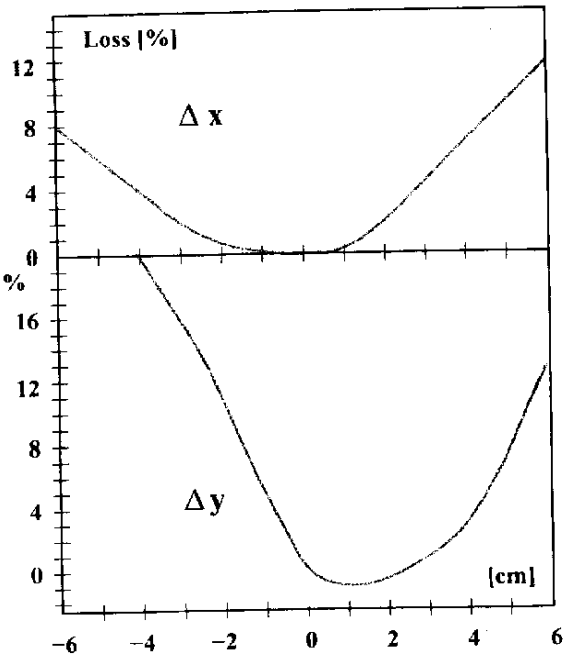

Fig. 34. The dependence of the photon collection (in percent loss) on displacement of the mirror axis (in cm), at the mirror center of curvature. The return ray deviation is twice the mirror center displacement shown here, and the radii of the mirrors are typically 240 cm.

Mirror alignment was checked both by detailed comparison of test rays, (about 80 rays per side of both C1 and C2) and by sweeping the beam within accepted limits and checking that the acceptance appeared to be continuous. Compared to simulation, the final mirrors as aligned in the counters lose 5–10% more than expected of the Cherenkov photons and introduce approximately an extra bounce, with ≈20% light losses at each bounce.

6.1.5. *Mechanical design and construction*

Each Cherenkov volume is an aluminum box of half-inch plate. For each counter the windows are a Kevlar–Mylar combination. They receive their strength from Kevlar fabric sewn at critical regions where the fabric is strengthened by a thin polyurethane coating. The gas containment is provided by Mylar sheets bonded with polyurethane to the polyurethane gasket. This arrangement permits

the use of thin Mylar (75 μm). The gaskets (Shore 65A polyurethane) were cast inside the counter with the window assembly in place and fastened by clamping bars bolted to closely spaced tapped holes at the edges of the aluminum frame. Tests showed no gasket or window leaks under helium at 150% of the design pressure (12"H_2O).

The hydrogen-containing beam tubes were made of thin-walled polyurethane (40 μm) bags stiffened by thin rohacell ribs and supported by Kevlar thread. The design keeps the leakage of hydrogen into the surrounding CO_2 well below 300 cm^3/h. This design worked satisfactorily as long as gas pressures were constant. Inadvertent overpressure of the tube in C2 near the end of the 1998 run ruptured the Rohacell ribs (but not the polyurethane bag). The sagging bag introduced local inefficiencies, but in a region only sparsely populated by events of interest.

Auxiliary containment windows and gas control systems for both C1 and C2 were continuously purged by inert gas passing through a volume surrounding the primary explosive gas containment. A 0.0025 cm Mylar sheet defined a buffer volume between the windows and atmosphere. Window failure might rupture the proportional chamber windows, creating an isobutane explosive hazard far more serious than a small hydrogen leak. Primary protection against the explosive window failure was the prompt detection and low impedance relief of excessive differential pressure. The buffer volumes were operated at low flow rates, with good sensitivity for potential explosive gas leakage, and did not show any levels beyond those expected from hydrogen permeation through Mylar.

Plumbing using 3 cm diameter pipes secured high flow rates at pressures below 3 cm H_2O. Large hand-blown bubblers permitted reliable operation at relief pressures of 4 cm H_2O at relief flow rates of 6 m^3/h of CO_2. The system permitted three exchanges of the C2 volume in 8 h, even with a high viscosity gas such as CO_2. Residual CO_2 and O_2 and H_2 were measured down to the 0.5% level. Gas samples from each counter were tested for contamination, down to 200 nm, by absorption spectroscopy. Comparison of results in N_2, in which significant absorption occurs, to results in CH_4, with little absorption, indicate that either residual oxygen was present or that photons with wavelength <200 nm were attenuated in the optics.

6.1.6. Photomultipliers

6.1.6.1. General remarks on photomultipliers. A question coupled to the mirror material and construction is the choice of photomultiplier (PMT). We discuss this here only briefly; more details can be found in Ref. [46].

Because the light yield from the H_2 side of the Cherenkov counter is low, the short wavelength response must be optimized. An optimum PMT design would therefore combine:

- photomultipliers with good sensitivity (probably coated with wavelength shifter) and windows with good transmission at least down to 180 nm; and
- high first dynode electron multiplication permitting good separation of one- and two-photoelectron yields as well as good separation of single photoelectron signals from pulses arising from processes further down the multiplication chain.

For H_2 only 2–3 photoelectrons are expected, which must be distinguished from noise pulses below the one photoelectron level.

Despite the lack of a quartz window, and transit time spread of about 0.8 ns, we chose to use 12.7 cm diameter Burle Industries 8854 photomultiplier tubes with a GaP first dynode yielding a gain of ≈ 20. Use of a large PMT minimizes "cracks" in our large volume optics. Taking advantage of the quartz windows available in various smaller PMTs would also have required an additional level of effort in gas purification and more expensive mirror surfaces to guarantee good short wavelength reflection. A wavelength shifter was added to enhance short wavelength light collection before the 1998 run, with no apparent degradation of timing.

We used a combination of new (≈ 6) and used Burle PMTs. The used tubes [48,5,8] had been stored in N_2 to guard against degradation due to diffusion of He or H_2 into the glass envelope. Tests of each tube indicated very little performance

difference between new and used tubes. First dynode gains were ≈20, and quantum efficiency inhomogenieties were not more than ≈30%, considerably smaller than reported previously [49].

These tests employed monochromators and a deuterium lamp [46]. The quantum efficiency was measured both in the multiplier and the photodiode mode. The results were consistent with BURLE specifications for the photodiode mode, but the quantum efficiency in the photomultiplier mode was found to be somewhat smaller, as also noted in Ref. [50]. We also tested gain variations as a function of single photoelectron rate, with the PMT exposed to a variable intensity blue LED background while measuring the gain associated with a 3 ns pulsed light source used to trigger an ADC gate. In all our tests we observed a low amplitude tail in the observed one photoelectron (p.e.) response, which indicated potential losses of order 10% for single photoelectron detection with a 0.25 photoelectron discriminator setting. These losses are apparent for example in Fig. 37, and are consistent with results seen by other experimenters [51].

6.1.6.2. Magnetic shielding. The optical configurations for C1 and C2 were chosen to allow simple mechanical construction. For C1 the PMTs were positioned in a region of low magnetic field (≈0.009 T) with the principal component perpendicular to the PMT axis. After installation of the magnetic shielding (≈40 kg per PMT), the field was reduced sufficiently to permit their operation.

For C2, the photomultipliers vertically near the beam line were in magnetic fields of up to 0.008 T before shielding, with the principal component at about 45° to the PM axis. Fields at the positions of photomultipliers away from the beam vertically are 0.004 T before shielding. The shield for C2, the design for which was derived in part from two-dimensional model studies, included a heavy plate to shunt field lines away from the PMT region, heavy shielding plates closer to the PMT position, soft iron boxes, and inner mu-metal cylinders around the multiplier chain. The fields after shielding were less than about 5×10^{-5} T at the photocathode position, as shown in Fig. 35, and about 0.0002 T at the PMT base positions.

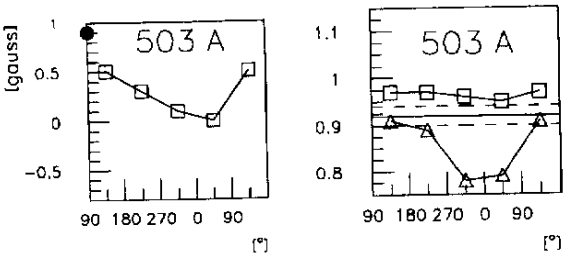

Fig. 35. Fields at the photocathode and performance in the magnetic field for a PMT near the C2R shell above the beam as a function of azimuthal angle around the perimeter of the tube, in the plane of the tube face. Zero degrees refers to the horizontal direction. Left: magnetic field parallel to the axis. Both points on the axis (circle) and 5 cm from the axis (squares) are shown. Right: ratio of light response with field on to field off, for an LED setup (squares), for light leaks during the run (band) and for a magnetized PMT (triangles).

Response tests as a function of rotational orientation of the PMT demonstrated the effects of residual magnetizations of a few gauss on the Kovar shields of the PMTs, probably from prior use in insufficiently shielded regions. The performance degradation shown in Fig. 35 resulted when a demagnetized PMT was exposed to fields of order 0.001–0.006 T, leading to subsequent magnetization. Without shielding, losses of 50–90% were seen in field on and off comparisons. With shielding and after demagnetization these losses dropped to ≈10%, measured both in tests and in running conditions. All PMTs were degaussed with a coil producing up to approximately 50 G at its center, in order to forestall losses due to tube magnetization.

6.1.6.3. Wavelength shifter. Before the 1997 run, we replaced the tubes previously used with ones (in many cases the same physical PMTs) onto which fast wavelength shifter (p-terphenyl) had been evaporated [35], to obtain sensitivity at wavelengths below 250 nm. Before making this change, we made tests using a D_2 lamp as light source. The setup included cutoff filters to study the response as a function of wavelength, and exploited the excellent stability of Hamamatsu deuterium lamps, as well as the rough correspondence of their emission spectra between 200 and 350 nm to that

of Cherenkov radiators. The PMT diameter could be scanned under computer control with a collimated flux about 1 mm in diameter, giving single photoelectron counting rates up to 0.5 MHz (see Ref. [46] for details). This result could be reproduced after long intervals, and reliable measurements of relative quantum efficiency could be made among photomultipliers.

The effect of wavelength shifter (WLS) on quantum efficiency, shown in Fig. 36, was determined by removing WLS for some patches several mm across, and observing the change in PMT response as the beam scanned the coated and uncoated areas.

At the wavelengths at which our tests were made (above 195 nm) no improvement in performance was seen when using dimethyl p-terphenyl [52] as compared to p-terphenyl. These results were used to predict the response of the PMT to Cherenkov light modulated by our mirror reflectance and gas transmission. The predicted improvement varied from 30% to 65% for different photomultipliers.

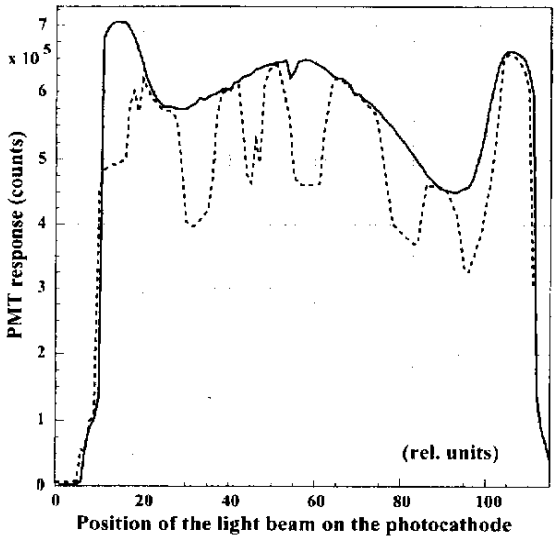

Fig. 36. Performance of a PMT before (solid line) and after (dotted line) five patches of wavelength shifter were scrubbed off. The third dip from the right is a place where halocarbon wax was applied.

6.1.6.4. Bases and tube performance. Photomultiplier placement inside the gas volume has the advantages of:

- decoupling the optics design from the mechanical design of the containment box, giving more flexibility in the optics design;
- simplifying the mechanical design by removing the need for VUV transmitting windows; and
- improving short wavelength photon collection, since they are then not required to pass through a window in going out of the gas volume.

Putting the tubes inside the gas volume, however, has risks: possible breakdown of tubes in the gas volume, or other component failure, with consequent experimental downtime for repair or loss of fiducial volume. We put the tubes inside the gas volume, and improved reliability by redesign of the PMT bases. The tubes were not powered until residual oxygen fell below 0.5%, an order of magnitude below explosive range.

Zener diodes were added to the dynode voltage distribution chain, to allow the bases to be run with less current through the resistors. The components were potted in a cylindrical shell fitted around the neck of the inner magnetic shield to improve heat transfer and compactness and facilitate fabrication. Both bench tests and reliability calculations[33] were done, indicating an expected failure rate of not more than one in the lifetime of the experiment. All bases survived a 200 h burn-in, and aside from one cold solder joint and one failed resistor in the high-voltage delivery, discovered and fixed when the counters were opened for other reasons, no component failures occurred during the experiment.

The performance of the tubes was satisfactory, judged both from direct observation of the pulse shapes and from off-line distributions of the size of the single photoelectron signal as seen in the ADCs. The Zener chain was required in only six of the 32 PMTs. One tube at high rates showed an increase in gain with time in spill, which we attribute to thermal heating of the dynodes.

[33] Reliablity calculations according to MIL-HDBK-217 standard.

The base performance was stable up to 10 MHz, well above the largest average rate in the experiment of about 4 MHz.

We did not experience any increase in afterpulsing attributable to H_2 or He permeation during our run, which stretched from 1995 through 1998 and included periods of 3–6 months of continuous H_2 fill. We did, however, observe some gradual degradation ($\approx 30\%$) in gain for high-rate tubes, for which we compensated by increasing the high voltage. The limiting factor is the average current, which was increased due to the extended AGS spill.

6.1.6.5. Readout electronics. The basic readout electronics was an ADC and a TDC channel. However, the high average rates led to occasional pre-empting of the signal of interest to us by unrelated overlap events. Losses at high-intensity running in high-rate tubes could reach $\approx 5\%$. A second TDC with threshold set above the one photoelectron level was installed for tubes on the right in 1997. Auxiliary electronics (an extra, more tightly timed, ADC and TDC channel and an "early" ADC sampling the period before trigger time) for overlapping events was installed during the early part of the 1998 run.

6.1.6.6. Individual PMT rates and photoelectron spectra. A clear one-photoelectron peak is seen in C1L and C2L as displayed in Fig. 37, which shows Cherenkov responses for low mass e^+e^- pairs identified using spectrometer momentum and matching calorimeter energy. These events, collectively, illuminate all PMTs on a given side, sometimes even sharing light between more than

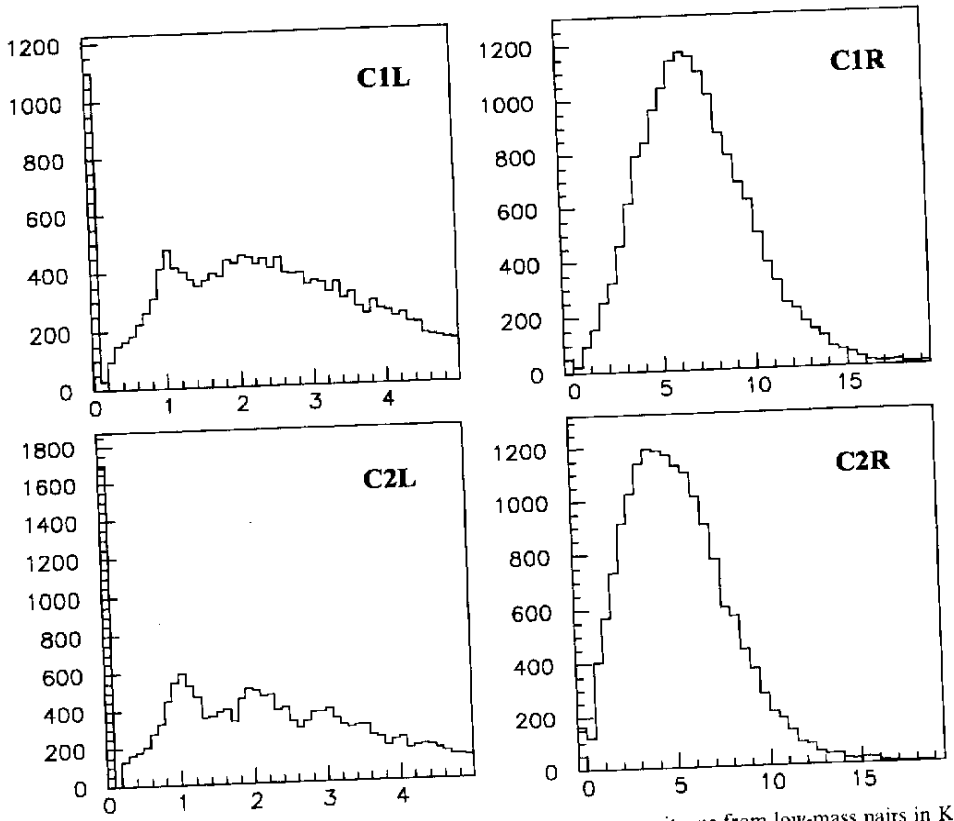

Fig. 37. Response of the four Cherenkov counters, in units of photoelectrons, to positrons from low-mass pairs in K_{De1} decay. Top left: C1L (H_2), top right: C1R (CH_4), bottom left: C2L (H_2) and bottom right: C2R (H_2).

one PMT for a single trajectory. The responses shown in Fig. 37 therefore are smeared by differences in PMT response among individual tubes. The visibility of a clear one photoelectron peak in the summed response indicates satisfactory intercalibration.

The results in Fig. 37 are expressed in single photoelectron units, i.e. are divided by the value corresponding to the apparent peak of the single photoelectron yield after pedestal subtraction. For particles which may contribute to more than one PMT, the responses were summed. The trigger threshold was set at a quarter of a single photoelectron response. The short plateau just above the threshold, seen particularly well in the C2L plot, lies at 15–20% of the peak value, but for some PMTs reached 30%. The two-, and perhaps three-photoelectron peaks are also visible. The plateau complicates the interpretation of the observed number of photoelectrons, with the one photoelectron peak defined as above. Convolution of the real one photoelectron response with the Poisson statistics expected for Cherenkov radiation reduces the average uncorrected estimate of the number of photoelectrons (N_{peob}) by about 10% with respect to the true yields.

Counting rates in tubes on the left (H_2) were of order 100–200 kHz. On the right (CH_4) at full beam intensity, the average counting rates were approximately 4 MHz in the highest-counting tubes. After slewing and pathlength corrections, the width of the relative timing between two PMTs, each giving a signal on a member of an e^+e^- pair, was about $\sigma_t = 0.85$ ns, the same to within errors before and after addition of the wavelength shifter, giving $\sigma_t = 0.65$ ns for a single tube.

Transit times in the optics for K_{Da} decays, as calculated using GEANT and the optics simulation code, were 11.5 ns in C1, and 10 ns for the inner tubes and 8.5 ns for the outer tubes in C2, with a spread of 0.1–0.3 ns. Some of the variation in timing is due to differences in the number of reflections in the collar plus collector. Each bounce changes the path of the photon and adds about 0.5 ns to arrival time at the PMT. However late photons with several bounces are less likely to be detected, since intensity losses are on average about 15% per reflection.

6.1.7. Performance

The efficiencies were monitored regularly using low mass e^+e^- pairs extracted from a Cherenkov efficiency trigger which required signals from at least three of the four cells (C1R, C2R, C1L, C2L).

Table 4 gives the efficiencies, $N_{peff} = -\ln$ (inefficiency) and the average number of photoelectrons, N_{peob}, for each of the four cells, for CH_4, and where available (CL1, CL2), for H_2. N_{est} is the estimated number of photoelectrons for hydrogen obtained by scaling N_{peob} for CH_4 by the ratio $n(H_2) - 1/n(CH_4) - 1$. The values in Table 4 are for the 1997 and early 1998 runs following the introduction of the wavelength shifter. Efficiencies on the right were about 0.5–1.0% less toward the end of the 1998 running, after the beam tubes were accidentally overpresssured. Statistical errors are of the order of 0.01 photoelectron units.

Table 4
Photoelectron yields during the 1997–1998 running period. $N_{peff} = \ln$(inefficiency), N_{peob} is the average number of photoelectrons, calibrated to the peak of the one photoelectron response and $N_{est} = N_{peob}(CH_4) \times n(H_2) - 1/n(CH_4) - 1$

Cell	CH_4 efficiency %	CH_4 N_{peff}	CH_4 N_{peob}	(H_2) N_{est}	H_2 efficiency %	H_2 N_{peff}	H_2 N_{peob}
C1L	99.7	5.84	7.17	2.28	89.6	2.26	2.24
C1R	98.7–99.2	4.74	5.80–6.7	1.5–1.8			
C2L	99.87	6.6	8.66	2.78	92.46	2.59	2.58
C2R	99.2–99.7	4.8–5.8	6.7–6.9	2.16			

Using H_2, N_2, CO_2 and CH_4. the mean photoelectron yields were found to increase linearly with $(n-1)$ as expected [46]. For a true Poisson distribution the inefficiency (no light seen) would be $\eta = \exp(-N_{peff})$. Discrepancies between N_{peob} and N_{peff} calculated from the observed inefficiencies arise from low-level residual backgrounds such as non-electrons in the normalization sample, false light due to scintillation or from beam muons just above threshold, non-Gaussian PMT one-photoelectron response, and variation of collection efficiencies.

The low pulse height tail on the PMT pulse shape and the loss of events below the PMT discriminator thresholds of 0.25 p.e. reduced N_{peob} and N_{peff}, respectively, by $\approx 10\%$. N_{est} compares well to the observed N_{peob}. For this comparison, the ratio of the two $n-1$ values was taken as 0.141/0.444.

The internal comparison of N_{peob} and N_{peff} for CH_4, especially the values on the right in Table 4, is more complex than the comparisons for H_2. C1R has persistently shown more problems than C2R with background contamination in the sample used to test efficiency. We ascribe this difference to the larger phase space acceptance of C2 for background processes such as scintillation and interactions in mirrors and gas windows creating δ-rays which are more likely to produce signals in C2R than in C1R. Thus a C2R signal may falsely validate a track and add it to the sample in which C1R is tested for efficiency. In addition, when the efficiencies are over 99%, N_{peff} is sensitive to the small errors in the efficiencies mentioned above. N_{peob} is less vulnerable to such small corrections. The efficiencies and yields shown are for all events, including those near the beam tube on the right, and such events were subject to loss in 1998 after overpressure of the beam tubes ruptured some of the supports and caused a repositioning of the tubes. For the foregoing reasons, we take the results from the left side as a figure of merit of the counters: $N_0 = 57$ photoelectrons/cm/$\sin^2\theta$ for C1 (three design reflections) and 66 in C2 (two design reflections). Taking into account the insensitivity of our optics below 200 nm, 5–10% PMT losses in residual magnetic fields, alignment losses of 5–10% rays not collected and about 20% due to the measured average of one extra bounce, these results compare satisfactorily to those scaled from other Cherenkov counters [53–55] and to simulation predictions. Fig. 38 compares the combined C1–C2 response for electrons and pions.

6.1.8. Summary

Conclusions from the Cherenkov counter tests and performance are:

- The observed efficiencies of approximately 89% in C1L, 90–93% in C2L, 98–99% in C1R and 99–99.5% in C2R compare satisfactorily to design goals of 97–98% on the right (in CO_2 or CH_4) and 85–87% in hydrogen. The counter performance also compares satisfactorily to simulation expectations and to performance of other large volume Cherenkov counters in which wavelengths below ≈ 200 nm are not utilized.
- Timing differences between counter elements indicates PMT timing ≈ 0.65 ns, even with the use of wavelength shifter.
- The Kovar shells of BURLE 8854 tubes may be magnetized, with subsequent performance degradation. Degaussing restores the tubes for effective use.
- The astigmatic venetian blind design from modest size mirror elements easily constructed in our shops, and low mass (0.2% X_0) mirror construction, may be of interest for other arrays where large areas or low masses are required.
- The Kevlar/aluminized Mylar enclosures provided a low-mass reliable gas containment and the method of sewing the middle partition in place rather than anchoring it solely with polyurethane allowed a median gas divider of relatively low mass.
- Custom-built large aperture plumbing and glass bubbler relief valves were superior to those commercially available. At pressures of about 1 cm of H_2O, these valves allowed flow rates of ≈ 2.8 m^3/h (CO_2) and purging of the counters within $\approx$ one 8-h shift.

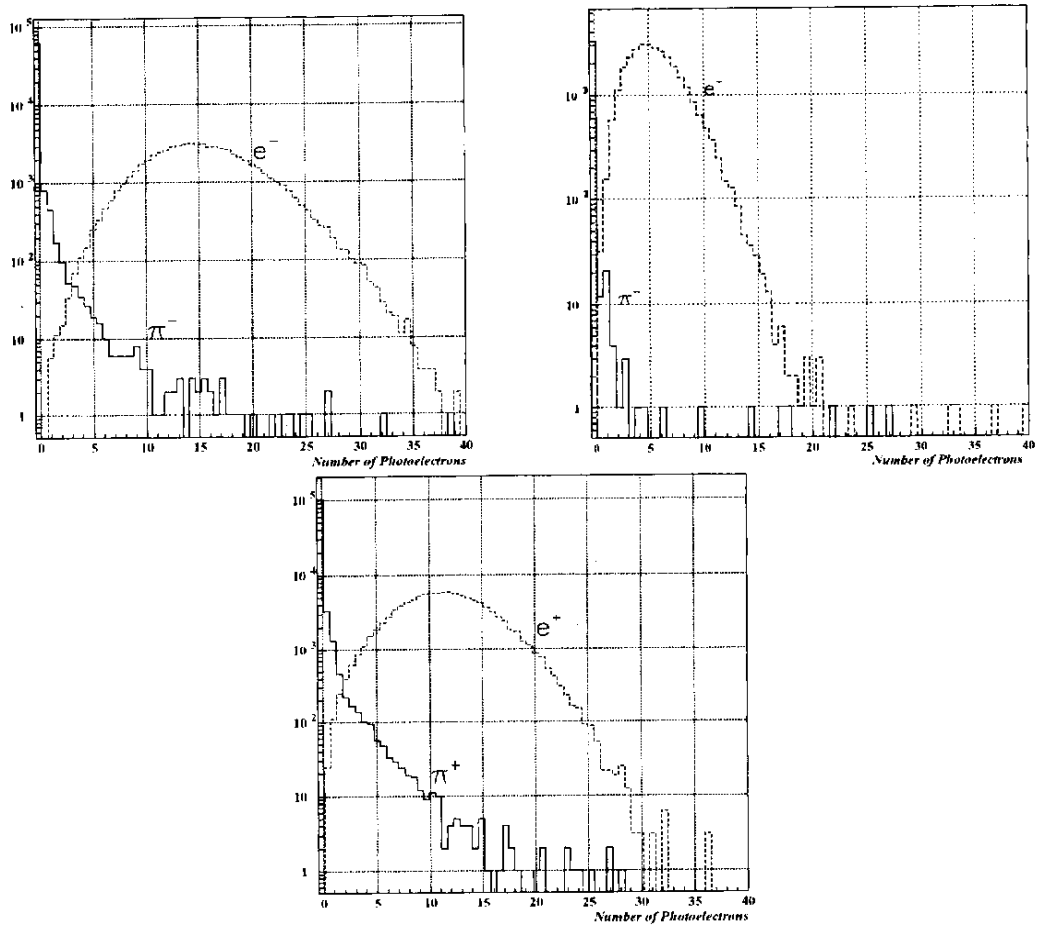

Fig. 38. Cherenkov counter performance: Number of photoelectrons seen by the Cherenkov counter phototubes for positrons from K_{Dal} decays and pions from K_τ decays: C1L and C2L with CH_4 (top left), C1L and C2L with H_2 (top right), C1R and C2R with CH_4 (bottom).

6.2. Muon identifier

The muon identifier was located at the downstream end of the experiment and covered the full acceptance of the apparatus which was approximately 4×2 m^2 at this location. It was composed of 12 fixed iron plates in the arrangement shown in Fig. 39. Each of the first eight of these plates was 5 cm thick; the following three plates were 10 cm thick and the series ended with a plate 5 cm thick. The proportional chamber walls were interspersed between the iron plates, with the first wall (M1) in front of the first plate. The B scintillator hodoscope was located after the first eight plates and the C scintillator hodoscope was mounted after M12, at the end of the muon chamber iron stack. With this setup it was possible to distinguish muons from pions by observing their range. This configuration allowed us to require that a muon traverses 75 cm of iron in order to reach the C hodoscope, i.e. 43 radiation lengths of material in addition to the 15 radiation lengths in the calorimeter. The minimum energy required for a muon to reach the B scintillator hodoscope was

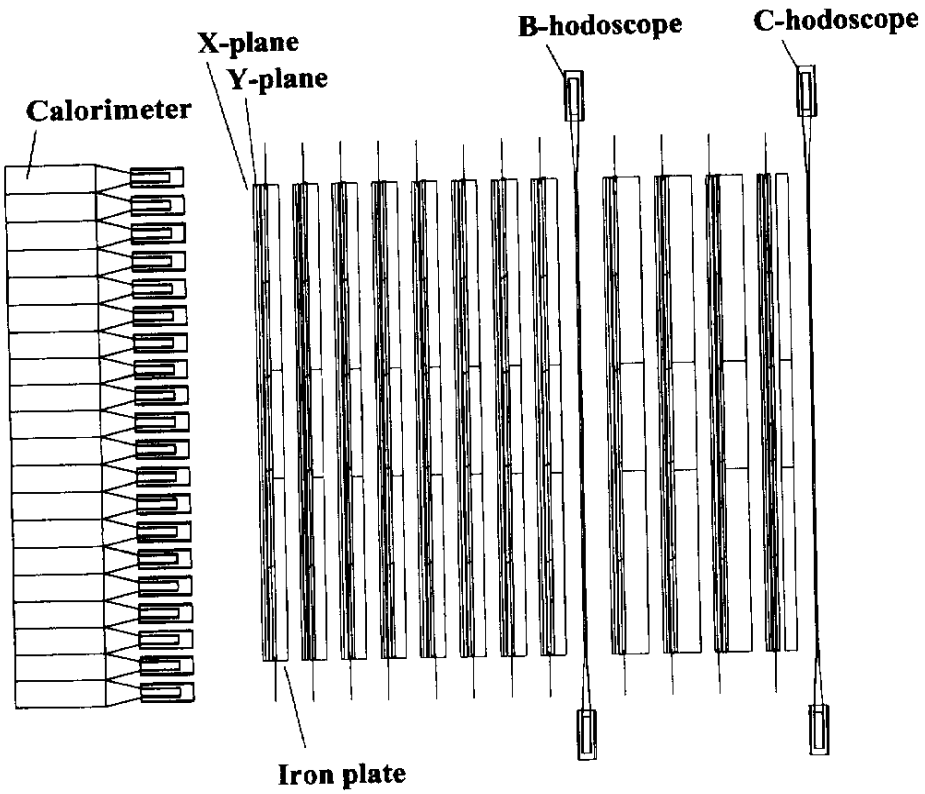

Fig. 39. Elevation view (y) of the muon detector. Also shown are the positions of the calorimeter, the B and the C counter hodoscopes.

0.8 GeV. To penetrate the calorimeter and the muon identifier a minimum of 1.3 GeV was required. The entire apparatus was traversed by the 6 GeV/c beam for which an opening of 42 × 42 cm^2 in the muon identifier was filled with a thin-walled mylar cylinder filled with helium gas at atmospheric pressure to allow beam passage with minimum interaction.

A x-plane consisted of eight modules 2.10 m long, four on the beam left side and four on the beam right side. A y-plane was assembled of five modules on the beam left side which are 1.68 m long, and two modules each on top and bottom, which are 2.10 m long. There were also five modules on the right side. Fouaccr are 2.10 m long. The central module measures 1.68 m in order to not extend into beam region (Fig. 41).

6.2.1. Mechanical construction

The modules were constructed of aluminum extrusions, that were joined back to back to form the profile indicated in Fig. 40. The extrusions were fabricated [34] in lengths of 7 m by a cold pressing process (*Strangpressen*). The material used was an aluminum alloy Ac-053/61 (AlMgSi 0.5).[33] In this process, the still warm extrusion was stretched tightly in such a way that the end product was absolutely straight and planar. This method of fabrication and our demands on the tolerances determined the geometry and the amount of material needed. After cutting each manufactured module into sections of 2179 mm length, two of these sections were glued together to achieve the required width for the backbone of

[34] Alusuisse, Sierre VS, Switzerland.

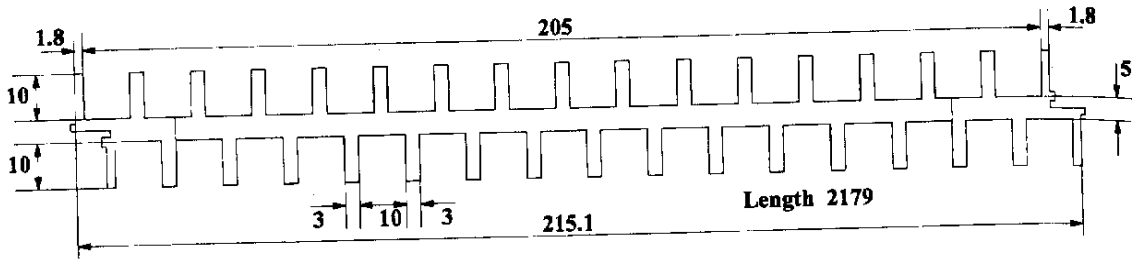

Fig. 40. Aluminium extrusion for the muon chambers. Marked dimensions are in mm.

430.2 mm. Covering the top and bottom of each of these sections were 2 mm thick aluminum plates, creating 32 tubes of square cross-section and with 1 cm^2 area, staggered top to bottom by one half a cell width. All of these aluminum components, plate coverings as well as extrusions were degreased and cleaned in different baths using chromatized acid and deionized water.[35] In all stages of the fabrication, assembly, cleaning, and construction the modules had to be handled with extreme care. As a result, no retooling or other mechanical correction was necessary, and the modules maintained a uniform precision (± 50 μm) in all dimensions.

To mount the different components necessary (gas distribution, anode wires, HV and signal readout) on each end of the profile, 40 mm of the ribs at both ends were removed. A glass fiber epoxy plate[24] was glued on to the remaining aluminum plate on either end, carrying the printed circuit boards for the anode wire attachment. One side was used for the gas distribution for the module; the other end for the high-voltage connection, the signal readout and the preamplifier. As glue we used Casinin with a primer.[36] To guarantee a reproducible and uniform layer of glue we mixed with it glass spheres of 80 μm diameter. Pressing this glue joint produced a very precise, constant and gas-tight seal.

The 30 μm diameter gold-plated tungsten anode wires, stretched to 1.5 N, were strung in the channels and soldered with a standard low-melting point tin. Some of the wires were welded by a technique we developed [56]. In a last step, the 2 mm thick aluminum cover was glued on the top and bottom. At the ends a thin aluminum angle was glued to provide the gas seal. With this construction we obtained a module of high stability that was self supporting and gas-tight, with a sensitive area of 2.10×0.43 m^2 equipped with 64 independent anode wire channels.

Because of the staggered front and back channels, a particle traversing a module always had to go through at least one active channel (Fig. 40). Using these modules we assembled the muon chamber walls. The modules, mounted vertically and horizontally (as shown in Fig. 41) allowed us to read the x- and y-coordinates of a charged particle traversing the wall. The walls were then hung into the fixed iron plate array.

A view of the muon identifier is shown in Fig. 39. For each wall the modules for x- and y-view had their own independent gas, and low- and high-voltage supplies.

The gas used was a 50%/50% CF_4/isobutane mixture flowing at a rate of 25 cm^3/min flushing a counter volume of 75 l. The chambers normally ran with a high voltage between 2150 and 2200 V. With a time gate of 50 ns width and a high voltage of 2200 V the individual chamber efficiency was 96% on average, as shown in Fig. 42 (see also Ref. [57]).

6.2.2. Electronics

The electronic chain following each pair of connected anode wires consisted of a preamplifier, a long special flat cable, a main amplifier, a discriminator and a coincidence circuit. This

[35] Buerox Anonization, Bueren a.d. Aare BE, Switzerland.

[36] Casinin 790.060, LMS AG für Leichtmetallsysteme, CH 4617 Gunzgen, Switzerland.

Fig. 41. Ar
chamber pl

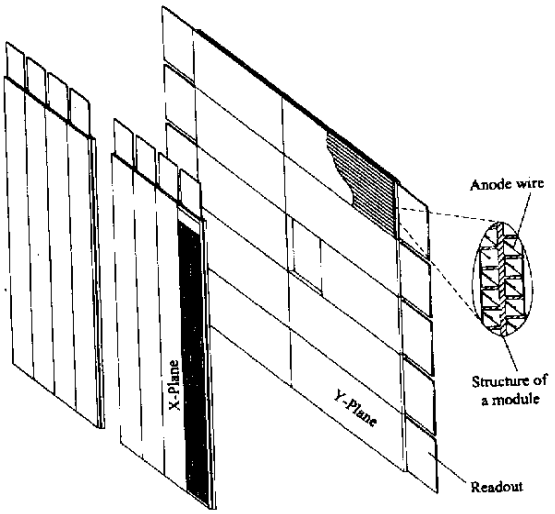

Fig. 41. Arrangement of the modules in a X- and a Y-muon chamber plane. The cell structure of a module is enlarged.

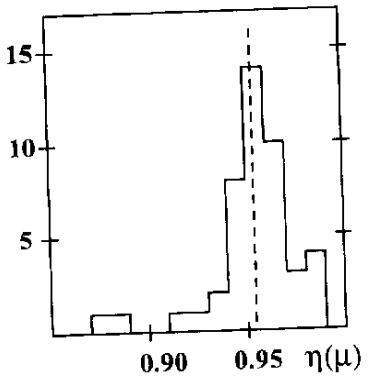

Fig. 42. Muon chamber plane efficiencies.

electronics was designed and produced in mid 80s and used for the proportional wire chambers of experiment E777 [48]. The whole signal processing chain is a more robust and more economical version of the ideal chain described in Ref. [28].

The preamplifiers were located at one end of the anode wires to minimize the total input capacitance and inductance of the connections. The preamplifier was based on a simple configuration with a common-base input transistor, an emitter follower and a long-tailed pair of transistors with the total current supplied from a current source (Fig. 43). There were two components, one diode and one resistor between the anode wire and the emitter of the first transistor. Their only function was the protection of the preamplifier in a case of wire chamber instabilities. The diode is robust enough to conduct any current due to positive excursion of the potential of the anode wire. The presence of the carbon 75 Ω resistor in series slowed the flow of negative wire discharge current which was then safely absorbed by the transistor. It was found experimentally that carbon resistors withstood the discharges better than metal-based resistors. The presence of the physical resistor between the anode and the input transistor increased the total equivalent series noise resistance by a factor of two. Thus the series component of the total noise increased by a square root of this factor, a small price to pay for practically indestructible preamplifiers. Moreover, the protection resistor, together with the input capacitance of the base to emitter junction of the first transistor provided an additional pole in the overall transfer function which simplified design of the main amplifier.

The long-tailed pair was the driver stage for a long cable carrying signals to the counting house where the rest of the chain as well as other experimental electronics was located. The cable was long enough to provide the signal delay to create and to distribute the trigger. The electrical characteristics of the cable were carefully measured and the cable was terminated for both the differential and for the common mode of excitations of the cable. The signal output current was steered between the two output transistors and there was no demand for an additional current during the presence of the signal pulse. Thus the power buses of the preamplifier remained clean which contributed to the observed stability and lack of oscillations in the system. These circuits required more power, but the preamplifiers were spread over an area sufficiently large for efficient air cooling. The preamplifier used an array of five fast *npn* transistors (CA3127E). There were eight channels in one preamplifier printed circuit board.

The degradation of the pulse in the cable was an important component in the overall shaping. The

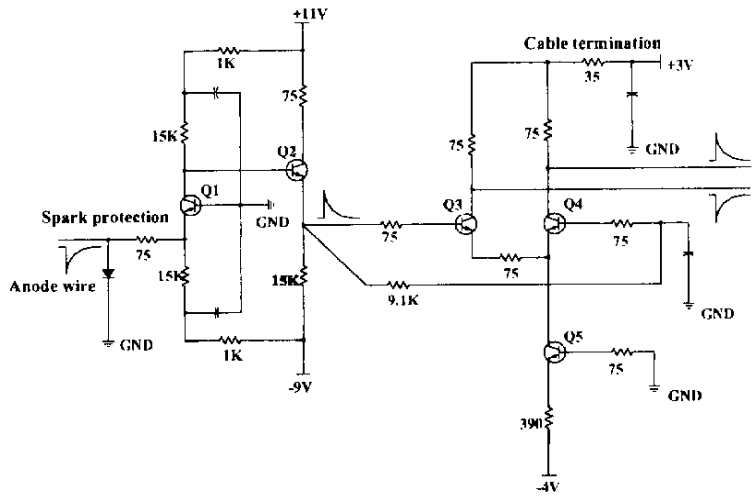

Fig. 43. Circuit diagram of the amplifier used for the muon chambers.

signal was amplified by an LM733 differential video amplifier with the gain set externally to 10. The differential input stage of the amplifier provided common mode rejection of about 40 decibels at the frequency of interest. The two differential outputs of the amplifier were fed in a balanced way into a series of three ECL line receivers connected as a Schmitt trigger acting as a discriminator. Due to the complete balancing of the linear part of the electronics there was only negligible cross-talk among the channels. Transitions between the discriminator output levels were not seen in the linear part of the electronics. The pulse shape presented to the discriminator had a 30 ns rise time and a 150 ns fall time. The equivalent noise charge was about 3000 electrons for the input capacitance of 20 pF. We ran with the effective threshold between 20 000 and 30 000 electrons. Such a low threshold allowed the operation of the chamber at a modest gas gain in the 10^4 region while being sensitive to practically the first electron cluster arriving at the anode.

When the trigger arrived and the signal was above the threshold level the address of the hit wire was read by a controller which passed this information to a CAMAC crate to be read by the Data Acquisition System. One receiver card with all linear and digital electronics contained 32 channels. One crate could hold up to 25 cards and was served by a single controller.

6.2.3. *Reconstruction and performance*

To optimize the separation of muons from pions, five variables associated with the muon stack were constructed and used in a likelihood analysis. In a first step, muon hits were collected in a cone where the axis of the cone was defined by the projection of the track from P3 to P4. The diameter of the cone increases as the track penetrates deeper into the stack. As the cone increases there is a concurrent increase in the number of spurious hits from other muon tracks or from hadrons produced from pions interacting with steel plates. To improve the reconstruction of the muon tracks, in a second step, only those hits which best fit to a muon track were used. Each track was divided into three segments, each combining four chambers. Because a muon track is relatively straight through the first segment, the hits were required to lie on a line. As a muon traverses the stack, it loses energy and completely stops or slowly curves due to the increase in multiple scattering. In the middle segment it was therefore only required that a hit is reasonably close to the previous hit. Hits from the first two track segments were used to make a second-order

polynomial fit and hits in the third segment were required to be close to the predicted crossing point from this fit.

With a cleaner sample of muon hits we defined a new variable, the hit ratio, which is the ratio of the sum of the observed hits in x and y to the sum of the expected number of hits (see Fig. 44a). Muons were required to have a hit ratio exceeding 0.5, and the region between 0.5 and 1 was used to construct the likelihood function for this distribution.

Because pions can hadronize as they interact with the steel slabs, secondary and tertiary tracks tend to occur near the end of the track and create multiple hits in the chamber. Using this characteristic, we were able to construct a variable which measures this noise by counting the number of extra hits within ± 5 cm of the x or y hit for each view of each chamber, and adding up the hits for all chambers. Ideally we expect no extra hits for muons, however due to the high rate environment, a muon track may be accompanied by multiple hits in a chamber (see Fig. 44b). With a loose cut of 15 hits, this distribution can also be used as a likelihood function.

From the momentum and direction of a muon track, the expected range could be calculated and

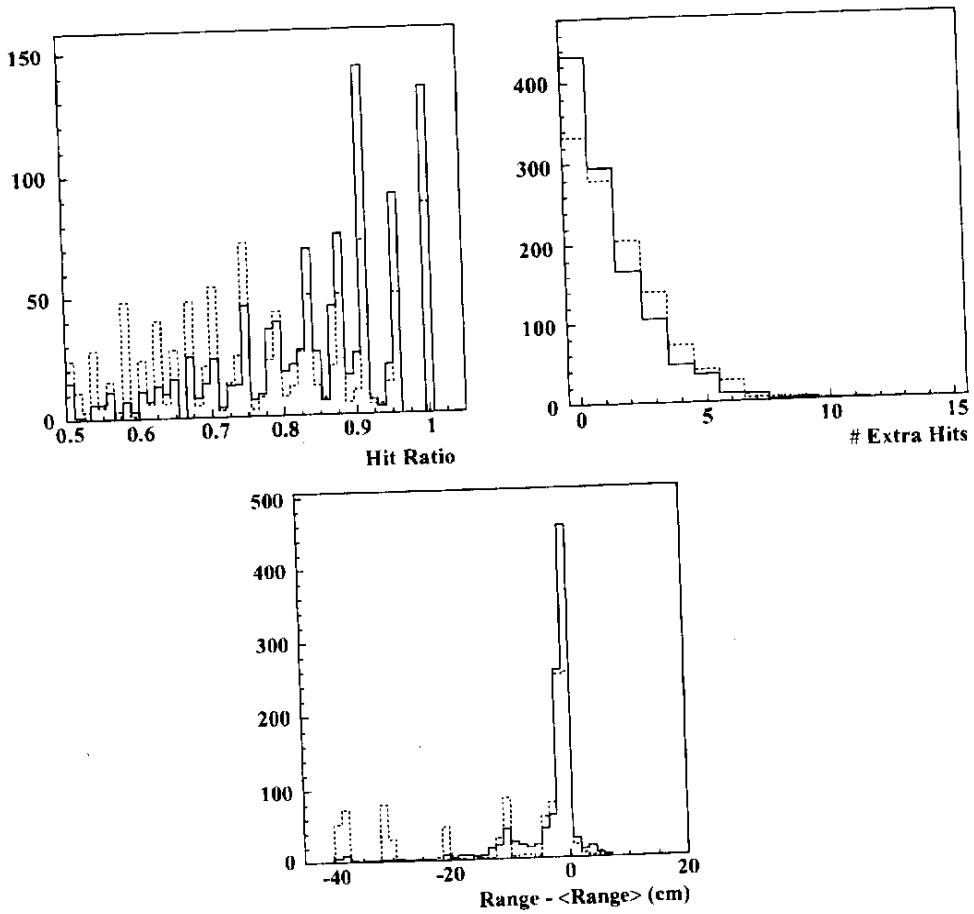

Fig. 44. Various distributions associated with the muon stack for muons (solid histograms) and pions (dashed histograms). Top left (a): ratio of observed to expected muon chamber hits; top right (b): number of extra hits found within ± 5 cm of a hit associated with a track in a given chamber; bottom (c): difference between the measured and the expected range of a particle in muon stack.

compared to the observed range. Since most pions are absorbed before the end of their range, the difference between the observed and the expected track depth (Fig. 44c) could be used to separate the two types of particles. If M_i was the last chamber that registered a hit for a track, the center of the steel plate between chambers M_i and M_{i+1} was taken to be the observed range. If an in-time C counter signal associated with the track was seen, the track was assumed to have traversed the whole stack. Since the range was then unknown, the observed and expected range were assumed to be identical. The influence of chamber inefficiencies was minor, since a hit was assumed to be the last hit along a track only if the next two chambers showed no hits associated with the track. The probability for missing two consecutive chambers was less than 4%.

A pion track can fake a muon track if the pion decays into a muon via the decay $\pi^+ \to \mu^+ \nu$ during its passage through the stack. The majority of the decay muons will appear at a finite angle in the (x,z) and (y,z) plane with respect to the original pion trajectory, displaying a characteristic kink. The quality of the fit to a second-order polynomial was measured by track χ^2. A cut on this quantity eliminated the majority of the decay muons (Fig. 45a).

Traversing the calorimeter, the muon loses a well defined and measured amount of energy (see Fig. 26). Multiple scattering in the calorimeter produces an angular displacement and a difference between the measured slopes before and after the calorimeter as well as a corresponding lateral displacement. The probability that the observed displacements could actually be caused by a muon of the measured momentum is also used in the muon identification. Taking the logarithm of the likelihood, a scattering χ^2 is defined as

$$\chi^2_{x\mathrm{scat}} \propto \frac{4}{\Theta_s^2}\left(\theta_x^2 - \frac{3x\theta_x}{z} + \frac{3x^2}{z^2}\right),$$

$$\text{where } \Theta_s = \frac{13.6\ \mathrm{MeV}}{\beta c p}\sqrt{\frac{x}{X_0}}. \tag{12}$$

Here, θ_x is the angular displacement in the x-plane determined by the angular difference between the track at P3–P4 and the first segment of the track at M1. The spatial displacement x is obtained from the difference in the x coordinate in front of the shower counter and z is the longitudinal distance between the front of the shower counter and M1. Θ_s is the multiple Coulomb scattering angle determined from p, βc, and x/X_0 which are the momentum, velocity of the particle and the amount of material responsible for the scattering

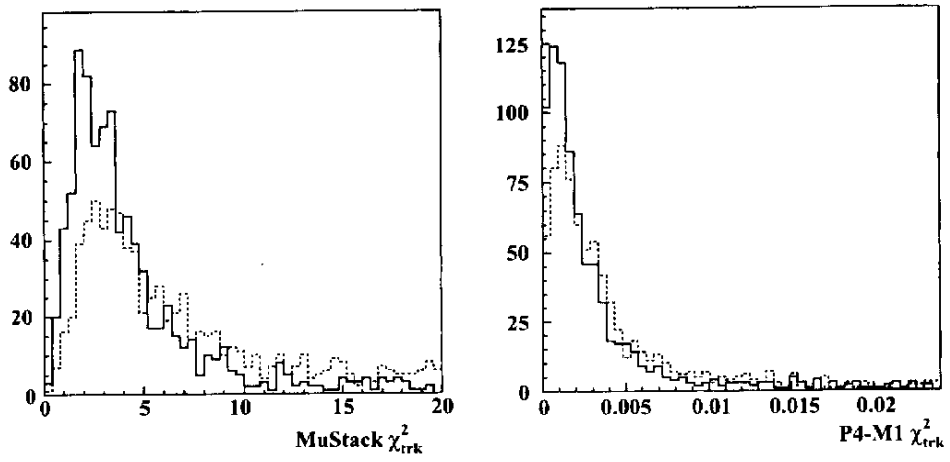

Fig. 45. Quality criteria for a track in the muon stack for muons (solid histograms) and pions (dashed histograms). Left (a): track χ^2 for a second-order polynomial fit to the track; right (b): scattering χ^2 in the calorimeter between P4 and M1.

ter, the muon loses a amount of energy (see ng in the calorimeter cement and a difference es before and after the corresponding lateral ility that the observed ly be caused by a muon um is also used in the ig the logarithm of the is defined as

$$\left(\frac{\chi^2}{2}\right),$$

(12)

lacement in the x-plane difference between the segment of the track at ent x is obtained from rdinate in front of the e longitudinal distance ower counter and M1. omb scattering angle d x/X_0 which are the the particle and the sible for the scattering

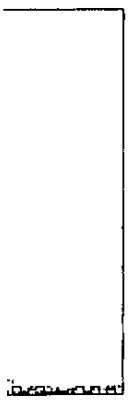

stograms). Left (a): track χ^2 M1.

measured in units of the radiation length. When the corresponding contribution in the y-plane is added one obtains the distribution shown in Fig. 45(b).

The combination of all these identification criteria using likelihood functions and χ^2 cuts yielded a μ^- identification efficiency of 75.9% with 94.3% of the pions suppressed.

7. Trigger

7.1. Trigger concept

The total charged-particle rate through the detector outside the beam region was about 50 MHz. The size of a typical event was 1.5–2 kb. A conventional 8 mm tape drive records up to roughly 500 kb/s. Hence, not more than a few hundred events per second can be written to a single tape. A fast trigger with a very high rejection for background and a high efficiency for physics events becomes crucial.

The general design philosophy of the trigger, as outlined in Fig. 46, was to use a multilevel structure which eliminated the largest fraction of events as early as possible with simple and fast hardware logic. More sophisticated, and hence slower requirements were implemented in successive levels. The sensitivity of the experiment was limited by this ability to suppress background since a higher beam intensity implies a much larger background rate associated mainly with random coincidences of tracks in the detector and a relatively smaller increase in K^+ decays.

The primary trigger (T0 trigger level), common to all trigger types, was based on charged particle hits in the calorimeter and the A and D hodoscopes. It was recognized in the early stages of the experiment that the beam interaction with the matter after the evacuated decay volume contributed significantly to the trigger rate if only the A hodoscope and shower counters were used. To ensure that the trigger is caused by the particles coming from the decay volume, the D hodoscope was also required in the primary trigger.

At T1 trigger level, fast particle identification information was available. Various triggers are

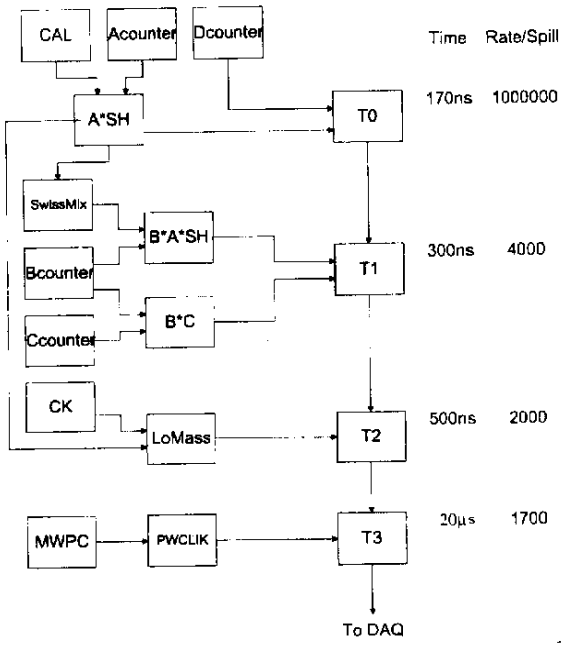

Fig. 46. Trigger scheme, response time and rate capability: T0–T3 indicate subsequent trigger levels; CAL the electromagnetic calorimeter, A(B,C,D) the different trigger hodoscopes; SwissMix and LoMass are described in the text.

configured according to the final states of interest. For example the trigger for $K^+ \to \pi^+\mu^+e^-$ required Cherenkov response on the left, and a muon signal in the B hodoscope. The T1 triggers were manually selected. The composition varied throughout the running periods.

K_{Dal} decay can also fake a $K^+ \to \pi^+\mu^+e^-$ final state and is also a large background to $K^+ \to \pi^+e^+e^-$. π^0's are also produced to a lesser extent in $K_{\mu 3}$ and $K^+ \to \pi^+\pi^0\pi^0$ decays. The characteristics of the K_{Dal} decay is such that the e^+e^- invariant mass is low. Taking advantage of the small separation of the e^+e^- pair in the non-bending (vertical) plane, these events can be greatly reduced. This was achieved in the T2 trigger.

The proportional chamber readout provides the number of non-empty cards (Ncard) in each half of each wire plane (logical plane) after the hits are buffered. Typical good events with three charged tracks have certain distributions of Ncard in each

chamber at the nominal running intensity. Spurious triggers with insufficient number of tracks, or pile-up triggers with noisy hits, can be rejected based on this information. This was achieved in the T3 trigger with special memory lookup modules.

The T0 trigger was free of dead-time. A master dead-time was set after a successful T1 trigger which inhibited further triggers and was only cleared if the T2 or T3 trigger failed, or after the event had been completely buffered in the Fastbus memory modules.

7.2. Hardware realization

7.2.1. T0 trigger level

This lowest trigger level was common for all trigger types. It was designed to indicate the presence of three charged particle tracks and it was formed from three coincidences between the A counter and the corresponding modules in the shower calorimeter directly behind it, as well as the D hodoscope.

In a high rate experiment, it is essential to reduce the pulse width of the signals that go into the coincidence. However, timing jitter resulting from such effects as slewing and light propagation time, limit such reductions. The A hodoscope elements, being 1.6 m long, had a 10 ns variation in timing, depending on the position of a hit. In addition, it operated at a threshold of 1.0 MeV, making it sensitive to neutron and photon rates. A custom-designed coincidence module (time adjusted circuit: TAC), was used to require a shower counter hit directly behind the A hodoscope slab, and to adjust the timing according to the position of the shower counter module. The A counter signal going into a TAC was split into 15 signals, each delayed by $i \times 0.7$ ns, $i = 1, \ldots, 15$. The discriminator threshold for the shower counter modules was set at approximately 80 MeV and the width was 20 ns. The ith shower counter module, counting from the end of the A counter away from the PMT, was connected to a coincidence circuit with the ith delayed A counter signal. Therefore, more delay was added to the A counter signal if the hit was closer to the PMT, thus compensating for the light propagation time difference. The output of the TAC was a logically ORed signal of all the coincidences in the module, with a full time width of about 7 ns. A total of 30 such A hodoscope and shower counter coincidences (A*SH), 15 on each side of the detector, formed the basis of the charged particle trigger.

Another feature of the TAC was a set of outputs that corresponds to the adjusted A counter timing and horizontal position of the hit using the shower counter segmentation. All such outputs for each side of the detector were sent to a logic unit (SwissMix), where the signals were logically ORed according to vertical columns. This provided the horizontal position of the A*SH hit which was later used for finding the correlated B hodoscope hits (see Section 7.2.2).

The three particles from K^+ decays, such as $K^+ \to \pi^+\mu^+e^-$ occupy the A hodoscope in a balanced way. The accidentals, on the other hand, are randomly distributed. A custom-designed matrix lookup unit (MLU) with fast memory chips made the selection of hit patterns more flexible.

The first 16 inputs (input-A) of such a MLU were used as addressing signals for a fast 16-bit memory chip. The bit-wise coincidences between the output of the memory and the next 16 inputs (input-B) were used as addressing signals for a 4-bit memory. The first 16 inputs were also used to address another 4-bit memory. The final output of the module was based on the coincidence of the outputs of the two 4-bit memory chips. The module was mounted in a CAMAC crate. All the memory locations are fully programmable through the CAMAC back-plane. The 16-bit memory was used to select the desired pattern of input-B for a given input-A. The 4-bit memory can be used to select pattern within each input group, or simply its multiplicity. The minimum input pulse width was 5 ns, and resolving time was about 3 ns. The time jitter between different patterns of signals was less than 1 ns. This proved to be a very general purpose trigger module, which was used in other places in the trigger system. A total of 13 such modules were used.

For the nominal T0 trigger, the A*SH on the right side was sent to Input-A of an MLU, where at least two hits were required. For each pair of

possible hits, only a limited region of the left side was allowed, within which at least one hit was required. The pattern of the allowed region was selected according to a Monte Carlo study of the $K^+ \to \pi^+\mu^+e^-$ decay. Similarly, to allow two hits on the left, a second MLU was used, where the inputs were interchanged by sides. To ensure that the trigger was caused by particles coming from the decay volume, D hodoscope hits were required, at least one on each side. The correlation between the D counter hits and A*SH was imposed, using one MLU for each side. The T0 trigger thus defined had a time jitter of about $\sigma = 1$ ns. It should be noted that because the MLU is programmable, the configuration of T0 trigger can be modified easily. Typical T0 trigger rate was about 10^6/spill. The trigger acceptances at this level for various decay modes are given in Table 5.

7.2.2. T1 trigger

Particle identification information was made available at T1 Trigger. The typical signals were from discriminators with a width of about 7–10 ns. The threshold for Cherenkov counter PMTs was set to about 0.25 photo-electrons. The hodoscope threshold was set to about one-quarter of the minimum ionizing peak. The main ingredients were

(1) CLAND(CRAND): Cherenkov counter C1 and C2 coincidence on the left(right), for identifying e^- (e^+).

Table 5
T0 trigger acceptance for various decay modes with three charged particles. The first column lists the acceptance for three different A counters showing a particle hit

Decay mode	Three A counters (%)	T0 (%)
$K^+ \to \pi^+\pi^+\pi^-$	31.5	21.9
$K^+ \to \pi^+\pi^0; \pi^+e^+e^-(\gamma)$	9.0	2.9
$K^+ \to e^+\nu_e\pi^0; e^+e^+e^-(\nu_e\gamma)$	5.6	1.7
$K^+ \to \mu^+\nu_\mu\pi^0; \mu^+e^-e^-(\nu_\mu\gamma)$	7.8	2.7
$K^+ \to \pi^+e^+e^-$	17.0	6.1
$K^- \to \pi^-\mu^-\mu$	33.0	16.3
$K^+ \to \pi^-\mu^+e^-$	20.0	8.3

(2) CLOR(CROR): Cherenkov counter C1 or C2 signal on the left(right), for Cherenkov efficiency measurements.
(3) BASH: At least one B hodoscope hit in the coincidence with A*SH, which is transposed into vertical columns by SwissMix. An MLU was used for each quadrant to allow only the hits in correlated regions.
(4) BCL(BCR): B and C hodoscope coincidence on the left(right). An MLU was used for each quadrant to allow only the hits in correlated regions.

Various T1 triggers were formed according to the particles in the final states:

(1) TAU = T0: Minimum bias trigger, with no particle identification. Its name reflects the fact that the most common three charged particle final state comes from K_τ decay. It was prescaled by a large factor.
(2) MUE = T0•CLAND•BASH: $\pi\mu e$ trigger required the presence of a e^- on the left side, and a μ^+ that reaches at least the B hodoscope.
(3) ELER = T0•CLAND•CRAND: $\pi^+e^+e^-$ trigger required a e^- on the left side and a e^+ on the right.
(4) MUMU = T0•BCL•BCR: $\pi^+\mu^+\mu^-$ trigger required both μ^+ and μ^- to reach the end of the muon stack.
(5) KE4 = T0•CRAND•$\overline{\text{CLOR}}$: $\pi^+\pi^-e^+\nu$ trigger required only e^+ on the right. In the runs for this trigger, the threshold for the Cherenkov counters on the right was raised to 2.5 photo-electrons, to reduce the trigger rate. Furthermore all events with a Cherenkov signal on the left were vetoed to suppress K_{Dal} events.
(6) CK = T0•CROR•CLOR: This trigger, which accepts events with K_{Dal} decays, was used to measure the Cherenkov efficiency. This trigger was prescaled.
(7) COSMIC: A special trigger based solely on the calorimeter hit multiplicity, for monitoring the calorimeter threshold, gain and timing. This trigger was taken between beam spills.

The typical T1 trigger rate for πμe runs was about 4000/spill at a primary beam intensity of 10^{13} protons/pulse. The T1 signal was fanned out to all the readout devices such as PCOS4, ADC and TDC modules.

7.2.3. T2 trigger

The purpose of the second level trigger was to suppress K_{Dal} decay background to MUE and ELER trigger. The e^+e^- pair in the K_{Dal} decay has a low invariant mass. In the vertical view, the trajectories of the e^+e^- pair tend to stay together, because there is little bending due to the magnetic field. The e^- and e^- at this trigger level were identified by the coincidence of the A*SH hit and the corresponding Cherenkov counters in front of it. The four vertical segments of the Cherenkov counter C2, in coincidence with C1, were mapped to the A*SH segments. The hit pattern on the left and right sides were then compared, using an MLU. If there was a match within ±1 A counter width in height, the LoMass logic was satisfied.

The T2 requirement depends on the T1 trigger type. For the ELER trigger to pass T2, it either had to survive a prescaler (ELERPS), or the LoMass logic was off (HiMass). Fig. 47 shows the invariant mass distributions for ELER triggered events passing this HiMass requirement. For the MUE trigger, the LoMass logic was required to be off. Other triggers automatically pass through this level. The T2 decision is made about 200 ns after T1. It reduced the trigger rate by about a factor of two in normal πμe data taking.

7.2.4. T3 trigger

This stage, identical for all trigger types, made use of the non-empty card count from the LeCroy 2748 MWPC readout controller available from each logical plane. While the latched data were being transfered from each PCOS4 card to the controller, a pulse was generated whenever a card contained at least one hit. A custom-designed memory module (PWCLIK) accumulated these pulses. Each module handled eight logical planes. At the end of the transfer, the pulse count was used to address an 8-bit memory. The contents of the memory were summed internally in a module,

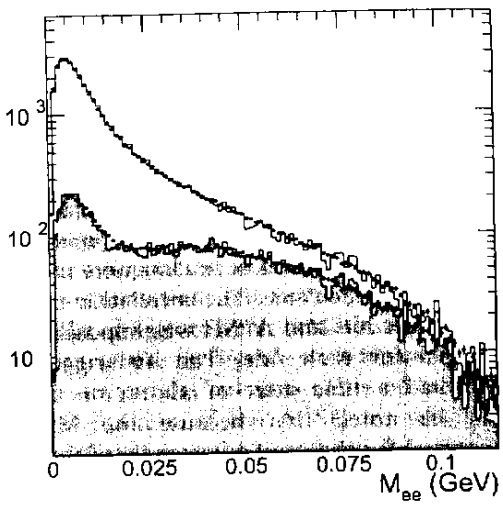

Fig. 47. M_{ee} distribution for accepted K_{Dal} events with (lower curve) and without (upper curve) the high-mass trigger requirement. The Monte Carlo simulation (histogram) includes events from other K^+ decays with a π^0 in the final state.

then presented to a bus, which connects all four PWCLIK modules. The output of all the modules were summed together according to a sequence of control signals, and the value was compared to a preset threshold. The content of the memory was pre-loaded, through the CAMAC back-plane, with a log-likelihood for each logical plane, determined off-line for a certain running condition. The sum then corresponds to the log of the joint likelihood. T3 trigger required that the total likelihood be greater than the threshold.

T3 trigger decision was made 20 μs after T2. Although it normally only rejected about 15% of the T2 trigger, most of the rejected events tend to be noisy with a large event size.

Trigger efficiencies are always very important in physics analyses. The triggers described here provided sufficient overlaps between them, so that the efficiencies could be determined. The prescaled triggers, TAU, ELERPS and CK were not only very useful for monitoring the detector performance, but also crucial for determining the efficiencies of the other triggers.

8. Online data acquisition and filtering

8.1. Data acquisition

The data acquisition system (DAQ) was based on the system of the MEGA experiment at the Los Alamos National Laboratory [58]. It consists of Camac-, Fastbus(FB)- and VME-modules, two Digital 3000/600 Alpha Workstations and a VAXstation as shown in Fig. 48.

CAMAC data were transfered to buffer memory in FB for each accepted T3 trigger. FB ADC and TDC modules can buffer up to 7 events before the data are transfered to the buffer memory. The data flow takes advantage of the 3.6–5.1 s accelerator cycle with 1.6–2.8 s beam-on spills. Working in parallel, fast crate controllers read out data into temporary memory buffers during the spill. The data transfer from memory buffers to host computer was carried out when the beam is off. Online event building and filtering was performed in a farm of workstations, and data were then sent to the host computer for taping.

The analog signals from the calorimeter and the Cherenkov counters were connected to FB ADCs (LRS1881), after being delayed through long coaxial cables. The discriminator output signals from the calorimeter, the Cherenkov counters and the hodoscopes were sent to FB TDCs (LRS1872). The ADCs were gated with the T1 signal, while the TDCs were configured in common start mode, started by the T1 signal. The failure of subsequent trigger levels resulted in a fast clear to the ADC and TDC modules, which were then ready for new

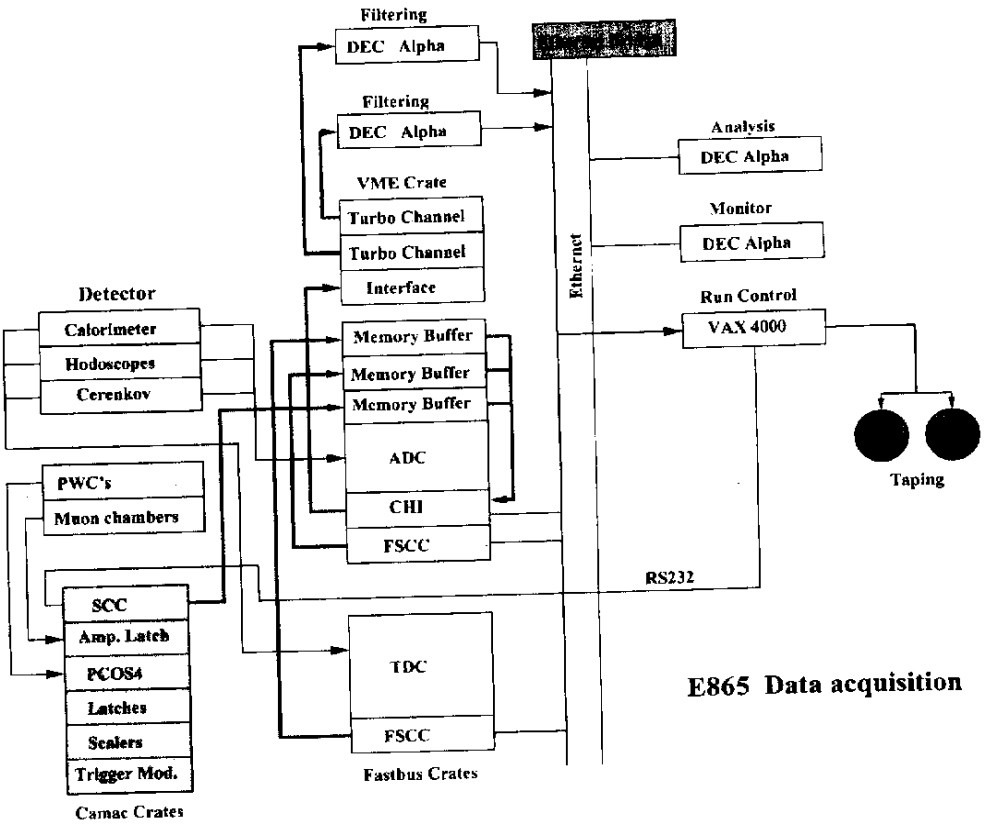

Fig. 48. A schematic diagram of the E865 data acquisition system.

triggers in 1 μs. The TDC modules are able to buffer seven events, while ADC modules could buffer 64 events.

The CAMAC readout handled data from trigger latches, scalars, PCOS4, and muon latches. All signals were latched at T1 trigger. If T2 was successful, PCOS4 data were transferred from the cards to the controller (LRS2748) at a 20 MHz rate. Similarly, the muon data, latched in amp/latch cards, were transfered to data buffers in a CAMAC crate.

There were four CAMAC crates. There is no multi-event buffering in the CAMAC system. Therefore, after a successful T3 trigger, each CAMAC crate was read out by a CAMAC smart crate controller (SCC) [59]. The SCC routed the data through a high-speed parallel port to a Fastbus memory module (LRS1892) with 4 Mb of memory. Depending on the chamber occupancy, it took about 200 μs to complete the data transfer.

The ADC modules were installed in one FB crate together with the memory modules, while the TDC modules were installed in another. Initially, two Fastbus crates were connected by a cluster interconnect (STR410), and controlled by one FB master, CERN host interface (CHI, STR330). All modules were read out by the CHI. This turned out to be the bottleneck for the throughput. In the upgraded system, the two FB crates were separated, each being read by one Fastbus smart crate controller (FSCC). The data were transfered to two Fastbus memory modules (LRS1892). The FSCC read FB modules at 5 MWords/s, with an overhead of 6 μs per module. This provided sufficient throughput when two crates operated in parallel. The readout of the FB ADC and TDC modules did not incur deadtime for up to six buffered events. A special counter kept track of the number of buffered events. After the CAMAC data were transfered to the FB memory modules, the counter was incremented, the inhibit was cleared, and the system was ready to accept another trigger. After the FSCCs finished reading one event from the ADC and TDC modules, the counter was decremented. If there were seven buffered events, the trigger remained inhibited until one event was read out.

At the end of a beam spill, the CHI was activated to start transferring the data from the memory modules to its internal memory through the FB backplane. Through an interface in a VME crate, the CHI could directly write the data into the memory of the workstations, transferring data of an entire spill. A maximal transfer rate was 3.27 Mb/s for the connection between the CHI and a workstation [57].

As discussed in the next subsection, the software running in the workstations built events from the buffered data, reconstructed the events for rejecting background, and transfered the events to the VAXstation. The maximum transfer rate between the farm and the VAXStation was limited by Ethernet, at about 450 kb/s.

The run control resided in the VAXStation and initialized the crate controllers, the CHI and the workstation farm, maintained the run status, received events from the farm, wrote the data to tape, and selected data for online monitoring. One high-density 8 mm tape drive was used, recording data at about 400 kb/s. To monitor the performance of the detector, a small fraction of the events were sent to a second Vaxstation via DECNET where they were analyzed, and histograms accumulated. The monitoring system provided alarms for various possible errors in the data taking system, as well as measurements of efficiencies of detector components.

The deadtime of the system was kept below 20%, most of which came from the CAMAC readout because it was not buffered. The event buffers in the ADC/TDC modules, together with fast FSCC readout eliminated the other readout deadtime. With the long AGS spill length (~3 s), the memory size in CHI (4 Mb) became a limiting factor.

8.2. Online event filtering

Even with the hardware trigger selection described in Section 7, the event rate from the CHI was still too high to be written to tape directly. Therefore, to provide a further selection of good events, data from the CHI were passed to a processor farm consisting of two DEC 3000/600 "Alpha" computers. Events were first assembled

from the raw data, which were still arranged as blocks from FB memory buffers. Each event was then analyzed by a FORTRAN77 "filter code", written in 18 modules, any combination of which could be selected during running.

Various combinations of the software modules performed the following tasks:

(i) A basic check on the buffer format and contents.
(ii) Inspection of the distribution of hits in wire chambers. Events could be rejected if the chambers contained either too few hits to reconstruct a track, or so many hits that the event was unlikely to be analyzable as an event of interest. This check was carried out by the construction of a likelihood function based on the number and distribution of hits in all chambers.
(iii) A search for "clumps" in the A hodoscope and shower counter, i.e. patterns of signals in these detectors that correspond to the detection of a charged particle or photon. At this stage, events could be rejected if less than three charged particles were found. Also, for triggers such as $K^+ \to \pi^+ \mu^+ e^-$ or $K^+ \to \pi^+ \pi^+ \pi^-$, for which no photon should be present, the event could be rejected if a photon was found.
(iv) A check on the timing and distribution of hits in the hodoscopes. This check was carried out by the use of a likelihood function, using TDC hits for the hodoscope elements and shower counter.
(v) The pulse height and timing of signals in the Cherenkov detectors were checked. Both the presence of a signal for an electron track and the absence for a muon or pion track were required.
(vi) A check was made, using the y-position of hits in the wire chambers, that 3 tracks existed that could reconstruct to a vertex in the y-coordinate. Since this coordinate is perpendicular to the bending plane of the spectrometer magnet, the check could be made quickly using straight-line geometry, without tracking through the magnetic field.
(vii) For triggers which required a muon to be present, a check was made for a possible track in the muon stack that had hits in at least 6 of the 12 chambers.
(viii) Chamber hits could be decoded, space points located and particle tracks could be reconstructed in the spectrometer.
(ix) The kinematics of the event could be checked.
(x) The track corresponding to the reconstructed K^+ momentum vector could be traced back through the beam-line elements to the production target.

Any combination of these modules could have been selected when running. In fact, the last three have not been required, and of the first seven, no more were used than were necessary to reduce the event rate out of the farm, to a level that could be written to tape under the running conditions. Typically, each module removed only a few percent of unwanted triggers. The combined effect of the entire filter code was to reduce the event rate to tape by about a factor of two.

9. Typical results

The E865 detector was primarily built to reach a high sensitivity to $K^+ \to \pi^+ \mu^+ e^-$, with its high resolution, excellent particle identification and high rate capability. Many other processes have also been studied with this device. Here we briefly summarize the overall performance of the detector, and various decays this detector has been used to study.

The most abundant three charged particle final states from K^+ decay are $K^+ \to \pi^- \pi^+ \pi^-$, and $K^+ \to \pi^+ \pi^0$ followed by π^0 Dalitz decays. These decays were used extensively to study the detector performance, in particular, vertex reconstruction (Fig. 19), invariant mass reconstruction (Figs. 21 and 47) and particle identification (Figs. 29 and 37), as well as for normalization. A GEANT Monte Carlo program was used to simulate the decay and interaction of particles with the detector. Most of the detector resolution effects could be accounted for by the simulation.

To reject πμe background events from other K^+ decays, excellent particle identification is essential. The level of particle identification achieved in analyzing the data collected in 1996, combining the information from the Cherenkov counters, calorimeter and muon detector, is summarized in Table 6.

For events that satisfied the kinematic and particle identification cuts, an event likelihood was developed to further separate the signal from background. This proved to be effective in rejecting the accidental background which was the dominant background in the final πμe sample. In this analysis, the single event sensitivity was 1.1×10^{-11}, with the background expected at the level of 0.4×10^{-11}. We have collected a factor of three more data in 1998. The analysis of this data is in progress.

The rare decays that have been studied include the highly suppressed flavor changing neutral current processes, 10,000 $K^+ \to \pi^+ e^+ e^-$ and 400 $K^+ \to \pi^+ \mu^+ \mu^-$ events, radiative leptonic decays, 450 $K^+ \to e^+ \nu e^+ e^-$ and 1500 $K^+ \to \mu^+ \nu e^+ e^-$ events [11,12,62]. The πee invariant mass distribution in Fig. 22 demonstrates the capability of selecting a large clean sample of events for a decay channel of a branching ratio of 3×10^{-7}. The spectrometer resolution was critical in selecting the $\pi^+ \mu^+ \mu^-$ events because the particle identification rejection of $\pi^- \pi^+ \pi$ events is limited by pion decay in flight (Fig. 49).

The relatively narrow beam phase space allowed reconstruction of decays with neutrinos. The kaon mass of decays such as K_{e4} could be reconstructed to about 33 MeV, dominated by transverse momentum spread of the kaon beam. The beam pixel detector, together with the reconstructed vertex, provided a measurement of the beam direction. This reduced the error on the transverse beam momentum, resulting in a kaon mass resolution of 12 MeV for K_{e4}. 400,000 K_{e4} events have been collected to study low-energy ππ scattering. Over 100,000 fully reconstructed K_{e3} events have been collected. The data set is being analyzed for extracting the branching ratio relative to that of $K_{\pi 2}$ as well as the form factor.

Table 6
Particle identification efficiencies and probabilities of misidentification [60,61][a]

	→π	→μ	→e
π^+	0.780 ± 0.004	0.049 ± 0.017	—
π^-	0.969 ± 0.002	—	$(2.6 \pm 0.1) \times 10^{-6}$
μ^+	—	0.743 ± 0.014	—
e^+	$(1.7 \pm 0.7) \times 10^{-5}$	$< 1.7 \times 10^{-5}$	0.873 ± 0.002
e^-	—	—	0.546 ± 0.003

[a] The symbol "→" denotes "identified as".

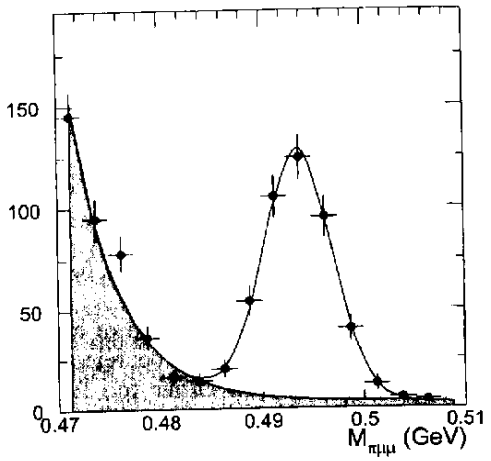

Fig. 49. Invariant three-particle mass spectrum in $K^+ \to \pi^+ \mu^+ \mu^-$ decay [12].

Acknowledgements

We gratefully acknowledge the contributions to the success of this experiment by Dave Philips, and the staff and management of the AGS at the Brookhaven National Laboratory, as well as the technical staffs of the participating institutions.

We are grateful to the staff of the Yale Physics Department shop, particularly Vincent Bernardo and Tom Hurteau for their work in constructing P3 and P4.

We are further indebted to Howard Clausing of Clausing Inc.[31] for his efforts in developing the reflective coatings used for the mirrors. The large

bubblers used in the Cherenkov counter gas system were designed and manufactured by Barry Lafler of the BNL Chemistry Department. The implementation of the Cherenkov counters benefitted strongly from the help of a highly motivated group of summer students, in particular V. Atoyan, R. Chapman, A. Freedman, S. McFadden, D. Parks, R. Rose, A. Tharrington, A. Trivelli and D. Willow.

This work was supported in part by the US Department of Energy, the National Science Foundations of the USA, Russia and Switzerland, the Research Corporation and the REU-program of the NSF.

References

[1] U. Bellgardt, et al., Nucl. Phys. B 299 (1988) 1.
[2] C. Dohmen, et al., Phys. Lett. B 317 (1993) 631.
[3] M.L. Brooks, et al., Phys. Rev. Lett. 83 (1999) 1521.
[4] D. Ambrose, et al., Phys. Rev. Lett. 81 (1998) 5734.
[5] A.M. Lee, et al., Phys. Rev. Lett. 64 (1990) 165.
[6] G. D'Ambrosio, G. Ecker, G. Isidori, J. Portoles, JHEP 08 (1998) 004.
[7] G. Ecker, A. Pich, E. de Rafael, Nucl. Phys. B 291 (1987) 692.
[8] C. Alliegro, et al., Phys. Rev. Lett. 68 (1992) 278.
[9] A.L. Deshpande, et al., Phys. Rev. Lett. 71 (1993) 27.
[10] S. Adler, et al., Phys. Rev. Lett. 79 (1997) 4756.
[11] R. Appel, et al., Phys. Rev. Lett. 83 (1999) 4482.
[12] H. Ma, et al., Phys. Rev. Lett. 84 (2000) 2580.
[13] J. Bijnens, G. Ecker, J. Gasser, in: L. Maiani (Ed.), DAPHNE Physics Handbook, Vol. 1, p. 115 (Frascati INFN—LNF-92-047, 1992).
[14] J. Bijnens, et al., Nucl. Phys. B 508 (1997) 263 erratum Nucl. Phys. B 517 (1998) 639.
[15] L. Rosselet, et al., Phys. Rev. D 15 (1977) 574.
[16] A.M. Diamant-Berger, et al., Phys. Lett. B 62 (1976) 485.
[17] G.S. Atoyan, et al., Nucl. Instr. and Meth. A 320 (1992) 144.
[18] J.R. Sanford, C.L. Wang, Brookhaven Nat. Lab., Acc. Dep. AGS Internal Report JRS/CLW-1 (11299) & JRS/CLW-2 (11479), 1967.
[19] C.L. Wang, Phys. Rev. D 16 (1977) 2197.
[20] C.F. Campagnari, Thesis, Yale University, New Haven, 1988.
[21] F. Sauli, CERN Yellow Report 77-09, 1977.
[22] M. di Palma, et al., Nucl. Instr. and Meth. 216 (1983) 393.
[23] L. Meier, Paul Scherrer Institute, private communication, 1993.
[24] S. Majewski, F. Sauli, CERN NP Internal Report 75-14, 1975.
[25] PCOS4: Proportional chamber operating system, LeCroy Corp., Chestnut Ridge, NY 10977, USA; see http://www.lecroy.com/lrs/dsheets/pcos4.htm.
[26] S.K. Dhawan et al., LeCroy Corp. Technical Note, 1994, unpublished.
[27] L.G. Christophorou, et al., Nucl. Instr. and Meth. 163 (1979) 141.
[28] J. Fischer, et al., Nucl. Instr. and Meth. A 238 (1985) 249.
[29] R. Henderson, et al., IEEE Trans. Nucl. Sci. NS-35 (1988) 477.
[30] J. Wise, et al., J. App. Phys. 74 (1993) 5327.
[31] T. Yamashita, et al., Nucl. Instr. and Meth. A 283 (1989) 709.
[32] L. Malter, Phys. Rev. 50 (1930) 48.
[33] D. Bergman, Thesis, Yale University, New Haven, 1997.
[34] S.W. Eilerts, Thesis, University of New Mexico, Albuquerque, 1998.
[35] E. Hahn, Fermi National Laboratory, Batavia, Illinois, private communication.
[36] I.M. Bassett, et al., Prog. Opt. 27 (1989) 161.
[37] J. O'Gallagher, et al., J. Opt. Soc. Am. A 4 (1988) 66.
[38] R. Winston, J. Opt. Soc. Am. 60 (1970) 245.
[39] D.A. Bartlett, et al., Nucl. Instr. and Meth. A 260 (1987) 55.
[40] W. Egle, et al., Opt. Eng. 29 (1990) 1260, 1269.
[41] Y.A. Budagov, et al., Instrum. Exp. Tech. 30 (1987) 737.
[42] D.P. Cadogan, SPIE 1113 (1989) 84.
[43] V.B. Huegele, SPIE 1113 (1989) 79.
[44] E. Scholle, Rochester Institute of Technology, private communication, 1997.
[45] R. Winston, Proceedings of the Sixth Meeting in Israel on Optical Engineering, SPIE, Vol. 1038, 1988, p. 590.
[46] R. Appel et al., E865-collaboration Internal Report 2000/01, available at http://www.phy.bnl.gov/e865/fullcerenkov.ps.
[47] K. Abe, et al., Nucl. Instr. and Meth. A 300 (1991) 501.
[48] N.J. Baker, et al., Phys. Rev. Lett. 59 (1987) 2832.
[49] M.L. Herbert, Thesis, University of Pittsburgh, 1978.
[50] P.J. Carlson, Nucl. Instr. and Meth. 158 (1979) 403.
[51] J. Napolitano, Rensselaer Polytechnical Institute, Troy, NY, private communication.
[52] T.A. DeVol, D.K. Wehe, G.F. Knoll, Nucl. Instr. and Meth. A 348 (1994) 156.
[53] M. Albee, et al., Nucl. Instr. and Meth. A 325 (1993) 429.
[54] D. Kawall, et al., Proceedings of the IEEE 1993 Nuclear Science Symposium and Medical Imaging Conference, San Francisco, CA, Vol. 1, p. 116 (IEEE Trans. Nucl. Sci. NS-41 (1994)).
[55] D. Kawall, et al., Proceedings IEEE 1991 Nuclear Science Symposium and Medical Imaging Conference, Santa Fe, NM, Vol. 1, p. 422 (IEEE Trans. Nucl. Sci. NS-39 (1992)).
[56] O. Ayranov, et al., Nucl. Instr. and Meth. A 408 (1998) 594.
[57] W. Menzel, Thesis, University of Basel, 1996.
[58] D.D. Koetke, in: W.T.H. van Oers (Ed.), Proceedings of the Fourth International Conference on the Intersections

between Part. and Nucl. Phys., Tucson, 1991, AIP Conference Proceedings, Vol. 243, 1992, p. 397.
[59] S. Hansen, et al., IEEE Trans. Nucl. Sci. NS-34 (1987) 1002.
[60] H. Do. Thesis, Yale University, New Haven, 2000.
[61] R. Appel, et al., Phys. Rev. Lett. 85 (2000) 2450.
[62] M. Zeller, Proceedings of the Chicago Conference on Kaon Phys., Kaon 99, in press.
[63] R. Appel, et al., Phys. Rev. Lett. 85 (2000) 2877.